基于二维离子晶体的量子信息处理

Quantum Information Processing with Two-Dimensional Ion Crystal

（申请清华大学理学博士学位论文）

培养单位：物理系
学　　科：物理学
研 究 生：乔　木
指导教师：金奇奂　教　授

二〇二三年五月

Quantum Information Processing with Two-Dimensional Ion Crystal

Dissertation Submitted to
Tsinghua University
in partial fulfillment of the requirement
for the degree of
Doctor of Philosophy
in
Physics

by

Mu Qiao

Dissertation Supervisor: Professor Kihwan Kim

May, 2023

学位论文指导小组、公开评阅人和答辩委员会名单

公开评阅人名单

(无，全隐名评阅)

答辩委员会名单

主席	尤力	教授	清华大学
委员	Kihwan Kim	教授	清华大学
	李颖	研究员	中国工程物理研究院
	王剑威	研究员	北京大学
	Stefano Chesi	副教授	北京计算科学研究中心
	丁世谦	助理教授	清华大学
秘书	Um Mark	科研助理	清华大学

关于学位论文使用授权的说明

本人完全了解清华大学有关保留、使用学位论文的规定，即：

清华大学拥有在著作权法规定范围内学位论文的使用权，其中包括：（1）已获学位的研究生必须按学校规定提交学位论文，学校可以采用影印、缩印或其他复制手段保存研究生上交的学位论文；（2）为教学和科研目的，学校可以将公开的学位论文作为资料在图书馆、资料室等场所供校内师生阅读，或在校园网上供校内师生浏览部分内容；（3）根据《中华人民共和国学位条例暂行实施办法》及上级教育主管部门具体要求，向国家图书馆报送相应的学位论文。

本人保证遵守上述规定。

作者签名：＿＿＿＿＿＿＿＿　　导师签名：＿＿＿＿＿＿＿＿

日　　期：＿＿＿＿＿＿＿＿　　日　　期：＿＿＿＿＿＿＿＿

摘　要

量子技术在近年来在学术与商业上均取得了一系列可喜进展，超导、光子体系在过去五年内上陆续实现了“量子霸权”，完成了随机量子线路采样与玻色采样，这些成果的展现出了量子计算机远超经典芯片的计算能力，尽管陆续有相关用经典计算器件仿真量子霸权的模拟算法被提出，并展现出不输于量子计算器件的能力，这种类似于十九世纪初期“马追火车”的尝试也将为未来量子器件全面超越经典器件设定一系列标准。

离子阱是当代最先进的量子信息处理平台之一，拥有全平台最高的量子体积与量子算法演示质量，并且演示了超过一小时的相干时间。但是离子阱平台中量子比特数量往往在5～20之间，相较于超导、中性原子动辄数十、数百的量子比特数量相对较少；且离子阱在过去数十年间一直致力于研究一维离子晶体上的量子信息处理，尽管在Penning阱中有些许基于二维离子晶体的工作，但如何使用这些二维离子晶体实现更加通用的量子模拟依然是一个开放问题。

在本文中，我们将会介绍首次在Paul阱实现的基于二维离子晶体的量子模拟。在我们的工作之前，学术界普遍认为Paul阱中无法使用二维离子晶体进行量子信息处理，尽管有理论方案被提出，但是并不清楚如何在实验上避免微振动对量子操作质量带来的致命影响。我们首先基于一款一体化离子阱芯片提出了通过旋转电场来调整微振动方向，并使其垂直于激光传播方向，进而将微振动“隐藏”起来，消除其对激光的影响；随后我们基于一体化芯片完成了二维离子晶体的制备，并开发了针对$^{171}\mathrm{Yb}^{+}$离子的EIT冷却技术，来快速制备二维离子晶体的运动基态；最后，我们在完成初态制备的二维离子晶体上演示了基于Ising模型的量子模拟。

我们的这项工作开拓了在Paul阱中基于二维离子晶体进行量子模拟与量子计算的新方向，尽管我们所尝试的离子数量相对较少，但是随着芯片加工工艺提升所导致的加热率下降以及将系统放入冷阱中所带来的真空提升与加热率下降，在该系统中装载上千个量子比特将不再是问题，也允许更大规模的量子信息处理实验，我们相信这一工作将会在NISQ时代大幅提升离子阱系统的拓展能力，并允许实验物理学家基于该系统探究更为丰富的物理现象。

关键词：量子信息；量子模拟；离子阱；二维自旋模型

ABSTRACT

Quantum technology has made promising progress in recent years, both academically and commercially. Researchers in superconducting and photonic systems have achieved ”quantum supremacy” and completed random circuit and boson sampling in the past three years. This shows that the quantum system far exceeds the computing capability of classical chips. However, successive attempts are to simulate quantum hegemony with classical computing devices. The attempts are similar to the early nineteenth-century ”horse beats iron horse”, which will set a series of standards for future quantum devices to surpass classical devices.

The ion trap is one of the most advanced quantum information processing platforms of our time, with the highest quantum volume and best quantum algorithms demonstration, and has shown a coherence time of over an hour. However, the number of quantum bits in ion trap platforms tends to be between 5 and 20, which is relatively small compared to the tens or hundreds of quantum bits in superconducting and neutral atoms. Moreover, ion traps have been devoted to studying quantum information processing on one-dimensional ion crystals for the past few decades. Although there is some work in Penning traps based on 2D ionic crystals, it is still an open problem to use these 2D ion crystals for more general quantum simulations. This paper presents the first quantum simulation based on two-dimensional ion crystals in Paul traps. Before our work, people doubt whether quantum information processing in Paul traps can be performed using two-dimensional ion crystals. Although theoretical solutions were proposed, it was not clear how to experimentally avoid the lethal effects of micromotions on the quality of quantum operations. We propose to ”hide” micromotions by rotating the electric field to adjust the direction of micromotions perpendicular to the laser propagation direction based on a monolithic ion trap chip to eliminate their detrimental influence on the laser. We prepare two-dimensional ion crystals based on the monolithic chip and develop a EIT cooling method for $^{171}\mathrm{Yb}^{+}$ ions to prepare the motional ground state of 2D ionic crystals. Finally, we demonstrate quantum simulations based on the Ising model.

Our work pioneers quantum simulations and quantum computations based on two-dimensional ion crystals in Paul traps. Although we only studied relatively small systems, the size of the system could be scaled up to thousands of ions by improving trap quality and putting the trap into a cryogenic system. We believe this work will significantly increase the scalability of ion trap systems in the NISQ era and allow experimental physicists to explore richer physics based on the system.

Keywords: Quantum information; quantum simulation; trapped ions; two-dimensional spin model

CONTENTS

LIST OF FIGURES

LIST OF TABLES

LIST OF SYMBOLS AND ACRONYMS

AF	Anti-Ferromagnetic
AM	Amplitude Modulation
AOM	Acoustic optical modulator
AWG	Arbitrary Waveform Generator
CCD	Charge-Coupled Device
EMCCD	Electron-multiplying Charge-Coupled Device
EIT	Electromagnetically-Induced-Transparency
FM	Ferromagnetic
MS gate	Mølmer–Sørensen gate
RF	Radio Frequency
PD	Photon Diode
PMT	Photomultiplier Tubes
QCCD	Quantum Charge-Coupled Device
UPD	Ultra-fast Photon Diode
UHV	Ultrahigh vacuum
Yb	Ytterbium

CHAPTER 1 INTRODUCTION

1.1 The Emergence of the Classical Computation Industry

In 1812, English mathematician and inventor Charles Babbage conceived the idea of using gears and rods to calculate mathematical tables. He later designed the Difference Engine to tabulate polynomial functions, which served as the prototype for the first general-purpose computer – the Analytical Engine[1].

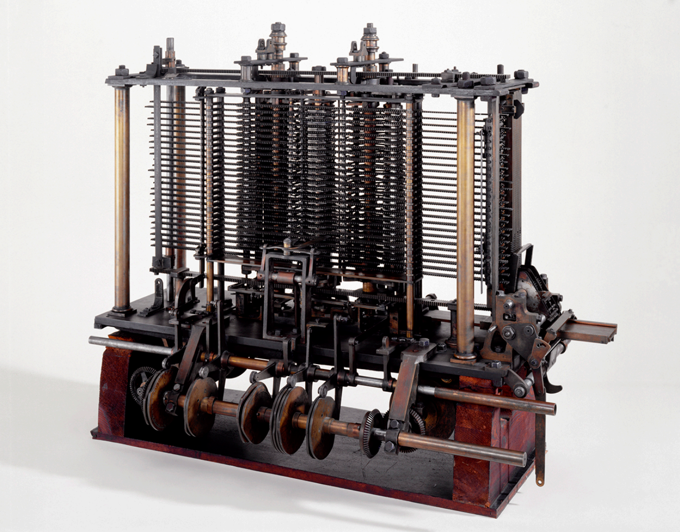

Figure 1.1 The Analytical Engine displayed at the Science Museum (London).

The Analytical Engine comprised several units, such as arithmetic logic units, flow control with conditional statements and loops, punch cards, and integrated memory. Users needed to utilize punched cards to input instructions into the engine. However, the Analytical Engine was never constructed due to insufficient funding during Charles Babbage's lifetime. The disparity between the capabilities of the Analytical Engine and the world's needs at the time made it challenging for Babbage to secure financial support.

In 1890, recent Ph.D. graduate Herman Hollerith constructed an electromechanical engine to aid the American census in enumerating and tabulating the collected data[2]. Hollerith meticulously calculated the cost of the enumeration for the ninth American census to be $2,095,563.32$ and projected that the expense would rise to $3,000,000$ for the tenth census. Although the government would cover the enumeration cost for each subsequent census, a machine would only require a one-time fabrication cost. Successfully bridging the gap between computing technology and societal demand, Hollerith built his apparatus and later founded The Tabulating Machine Co. This company merged with

Figure 1.2 The electric tabulating system displayed at the Smithsonian National Museum of American History (DC).

several others to form the Computing-Tabulating-Recording Company, which eventually became the industry giant IBM[3].

In 1936, Alan Turing explored the types of numbers computable by a machine composed of tape, squares, and scanned symbols. This machine is now known as the Turing machine, which Turing used to demonstrate that there is no solution for Hilbert's Entscheidungsproblem[4]. This problem asks, "Is there a general process for determining whether a given formula A of the functional calculus is provable?". Three years later, Germany invaded Poland, and World War II began. Turing was tasked with breaking the German Enigma machine, which was used to encrypt secret messages. He also designed an electro-mechanical machine called the British Bombe, based on his Turing machine concept, to decrypt Enigma's messages.

Concurrently, another cryptanalysis project led by Tommy Flowers, called Colossus, was under development in Britain. Colossus was the world's first programmable, electronic, digital computer and was built using 18,000 vacuum tubes. The ENIAC (Electronic Numerical Integrator and Computer) is perhaps the most famous vacuum tube computer, designed by John Mauchly, a professor at the Moore School of Electrical Engineering at the University of Pennsylvania, and John Presper Eckert, a graduate student at the same institution. ENIAC was sponsored by the United States Army Ordnance Department to expedite the recomputation of artillery firing tables[5]. It occupied a room measuring 30 by 50 feet and weighed 30 tons.

In 1949, the success of ENIAC motivated John Mauchly and John Presper Eckert to

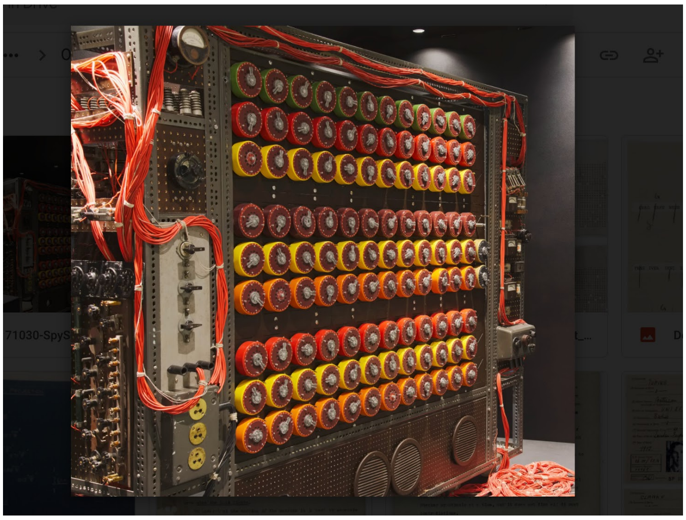

Figure 1.3 The British Bombe displayed at The National Museum of Computing (Bletchley Park).

establish the world's first computer company, Electronic Controls Company. The name was soon changed to Eckert–Mauchly Computer Corporation (EMCC) in 1950. Similar to Herman Hollerith's company, EMCC also aimed to sell their computers to the United States Census Bureau to help researchers reduce the number of punch cards. EMCC is now a part of Unisys.

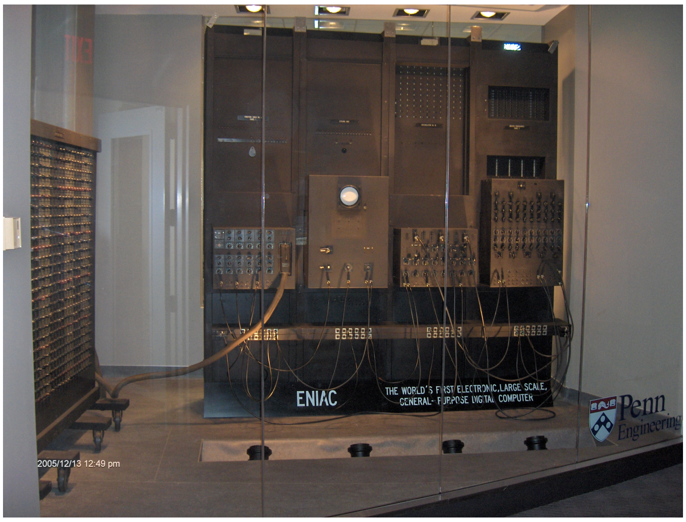

Figure 1.4 The ENIAC displayed at the University of Pennsylvania.

In addition to ENIAC, John Mauchly and John Presper Eckert also constructed EDVAC (Electronic Discrete Variable Automatic Computer) at the Moore School of Electrical Engineering. EDVAC was designed to process binary data and store programs inside the computer. At the time, von Neumann was consulting for EDVAC as a member of the Scientific Advisory Committee and used ink to write a 23-page sorting algorithm for EDVAC[6]. During this consulting period, von Neumann described a computer architecture in which the computer can store data and programs in its memory using the same address space[7], now known as the von Neumann architecture. After World War II, von Neumann returned to the Institute for Advanced Study at Princeton University and designed another binary computer called the IAS machine. The IAS machine was built with 1,700 vacuum tubes, had a 40-bit word, and could store 20-bit instructions. In 1952, two IBM researchers, Jerrier Haddad and Nathaniel Rochester, created IBM's first commercial computer, the 701, based on the IAS machine, which launched the computer industry for IBM.

Figure 1.5 The TRADIC at Bell Labs.

While IBM was marketing its first commercial computer for translation and blackjack, the era of vacuum tubes was drawing to a close. In 1947, three physicists at Bell Labs, John Bardeen, Walter Brattain, and William Shockley, invented a point-contact transistor made of germanium and published their work in Physical Review[8]. Research on semiconductor transistors was motivated by the need to replace unreliable vacuum tubes, which were too fragile due to their glass cover. Following the invention of the transistor, Jean Howard Felker, another researcher at Bell Labs, began constructing a fully transistorized digital computer, the TRADIC (TRAnsistor DIgital Computer or TRansistorized

Airborne DIgital Computer), which was completed in 1954. One year after the development of the TRADIC, William Shockley left Bell Labs and brought silicon to Silicon Valley. When Shockley founded his own company, reporters asked him why he left Bell Labs, to which he replied, ”You only live once. I would like to do something else for a change.”[9]. Shockley believed that the future of the semiconductor industry lay in silicon, not germanium, as germanium had insufficient thermal stability and insulating properties. Shockley Semiconductor laid the foundation for the silicon-based classical information age and set the stage for the legends of Silicon Valley.

1.2 The birth of quantum computation

The idea of using quantum mechanics to process information can be traced back to the 1960s when Stephen Wiesner came up with the concept of a quantum banknote[10]. However, the original paper was rejected by the editors and referees of *IEEE Transactions on Information Theory*. In 1973, Soviet mathematician Alexander Holevo calculated a bound for the amount of information transmitted by a quantum channel, and this was the earliest published paper on quantum information. In 1980, Soviet mathematician Yuri Manin proposed the idea of using superposition and entanglement to create a quantum automaton[11]. In the same year, Charles Bennett published a paper in the *Journal of Statistical Physics*, demonstrating that any Turing machine could be represented as a time evolution of a quantum state under a particular Hamiltonian[12].

One year later, in 1981, IBM and MIT organized the ”Physics of Computation” conference, which brought together some of the most renowned physicists. The talks given at the conference were published in the *International Journal of Theoretical Physics*. At the conference, Richard Feynman delivered a talk titled ”Simulating physics with computers,” where he asked, ”Can physics be simulated by a locally interacted universal computer?”, and proposed the idea of simulating quantum physics with quantum computer elements. At the same conference, Tommaso Toffoli[13] and Edward Fredkin[14] also discussed the possibility of using quantum systems to perform computation. However, credit for founding quantum computation is mostly given to Feynman, possibly due to his more concrete ideas and others’ citations. The ideas that emerged from the ”Physics of Computation” conference indeed inspired the birth of quantum computation. In 1984, David Deutsch proposed his idea of the quantum Church-Turing principle, stating that ”Every finitely realizable physical system can be perfectly simulated by a universal model computing machine operating by finite means”[15]. In this proposal, Deutsch also explained that the advantage of quantum computers originated from ”quantum parallelism.” Five years later, David Deutsch envisioned quantum computational networks to discuss how to physically realize a quantum Turing machine[16]. At that time, nobody knew what a quantum computer could do.

Entering the 1990s, the field of quantum computation developed rapidly. In 1991, David Deutsch and Richard Jozsa discovered the first quantum algorithm with exponential speed-up over classical algorithms[17]. In 1993, Seth Lloyd suggested that applying a sequence of electromagnetic pulses to arrays of weakly coupled quantum systems could coherently perform computation[18]; Ethan Bernstein and Umesh Vazirani first used the term ”bounded-error quantum polynomial time (BQP)” and asked whether $\mathrm{BQP}\neq\mathrm{BPP}$[19]; Andrew Chi-Chih Yao proved that any function computable in polynomial time by a quantum Turing machine has a polynomial-size quantum circuit[20]. In 1994, Peter Shor at Bell Labs developed the first practical, useful quantum algorithm for factoring numbers with exponential speed-up, which marked a historical turning point for large-scale investments in quantum computation. When Shor’s paper was published, nobody knew how to build a quantum computer, so it was time for experimental physicists to consider how to turn the idea of a quantum computer into reality.

The earliest idea of building a qubit came from Klaus Obermayer and his colleagues, who suggested using the position of an electron in different energy levels of a quantum dot to store information[21]. Then, in 1994, Serge Haroche’s group proposed an idea of encoding information based on cavity quantum electrodynamics and creating entanglement through spontaneous emission[22]. In the same year, physicists were excited by Shor’s algorithm and seriously tried to find a way to build an actual device. One year later, the field of quantum computation witnessed an explosion of experimental works: Harry Kimble’s group realized a conditional phase gate based on nonlinear optical response for qubits stored in polarization[23]; David Wineland’s group realized a controlled-NOT gate between qubits stored separately in the internal and external degrees of freedom of a single trapped $^9\mathrm{Be}^+$ ion[24]; Ignacio Cirac and Peter Zoller proposed an idea of entangling internal states of trapped ions through a phononic bus[25]. Around 1994, photons were the first candidate qubits, but their lack of interaction made it challenging to perform two-qubit gates. However, after 1995, ions became the most promising candidates. The Cirac-Zoller paper was the first to show a practical way to build a quantum computer from a theoretical imagination, opening up the experimental race to create a real device in the lab.

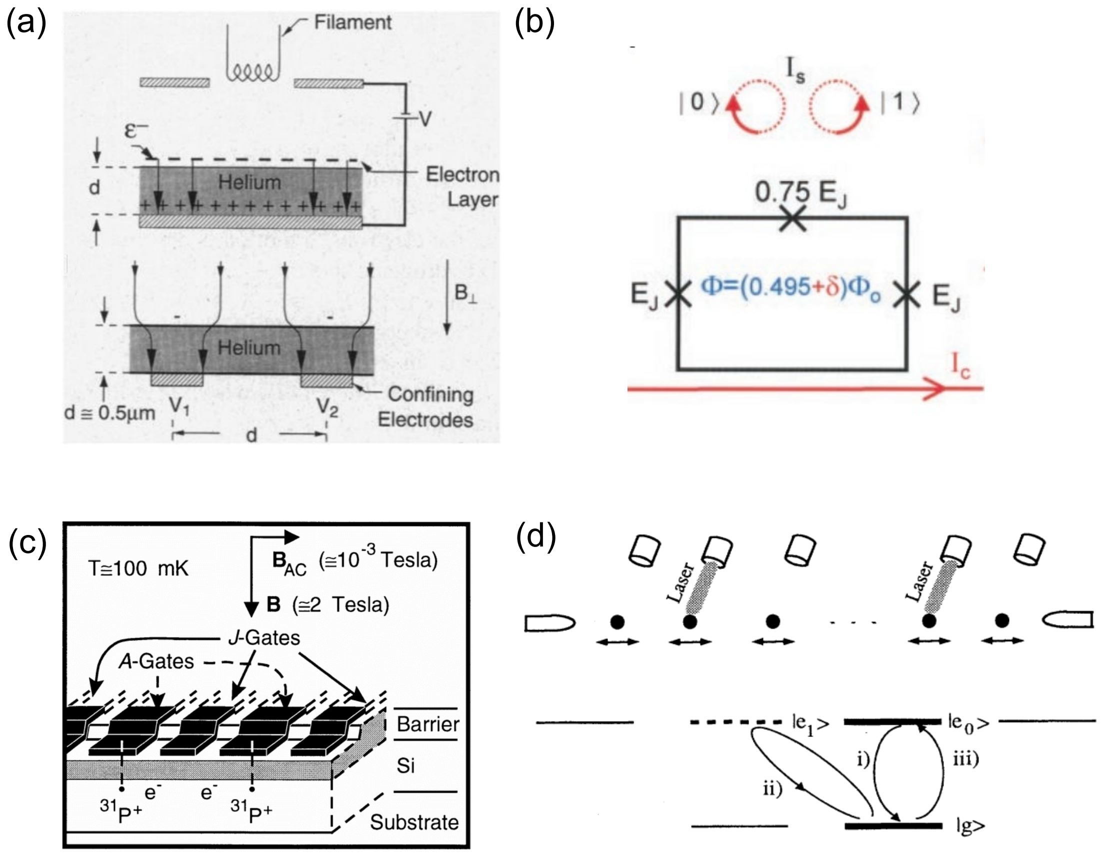

Figure 1.6 Systems suitable for quantum computation.
(a) Electrons trapped on the surface of helium. (b) Persisten qubit in Josephson junctions. (c) Qubits confined in a Si host. (d) Linear ion crystal confined in vacuum.

After the Cirac-Zoller paper, many other systems capable of quantum computation were proposed. In 1997, Isaac Chuang proposed an approach based on multi-pulse resonance techniques for quantum computation[26]; Alexander Shnirman and Dmitri Averin independently proposed an approach based on coherent tunneling of Cooper pairs in low-capacitance Josephson junctions for quantum computation[27]; Daniel Loss and David DiVincenzo proposed an approach based on coupling the electron spin states of single-electron quantum dots[28]. In 1998, Bruce Kane presented a scheme based on atoms in doped silicon devices to implement quantum computation[29]. In 1999, Atac Imamoglu proposed an idea of using quantum dot spin inside a high finesse microcavity to build a solid-state quantum computer[30]; Johan Mooij proposed an idea of using persistent current inside Josephson junctions to build a solid-state quantum computer[31]; Philip Platzman proposed an idea of using electrons trapped above a thin film of liquid helium for quantum computation[32]. In the early 21st century, a few new platforms were proposed. In 2001, Mikhail Lukin presented an idea of using dipole-dipole interaction between atoms excited into Rydberg states to realize two-qubit gates[33]. Motivated by these various proposals for building an actual quantum computer, in 2000, David DiVincenzo summarized a checklist to test whether a system is suitable for quantum computation, now known as the DiVincenzo criteria[34]:

1. a scalable physical system with well-characterized qubits
2. the ability to initialize the state of the qubits to a simple initial state
3. long decoherence times (that exceed the gate operation time)
4. a universal set of quantum gates
5. the ability to perform qubit-specific measurements

All of the above systems are under heavy research efforts, while none of them is recognized as the most suitable one for quantum computation with wide consensus. The race to build a large-scale quantum computer could still continue for several decades.

CHAPTER 2 INTRODUCTION OF ION TRAP

2.1 Quadrupole Trapping Fields

The idea of ion traps arose from the question[35] : What happens if one injects charged particles into a multipole field? Electric or magnetic multipole fields can generate binding forces that trap charged particles. Generally, the order of trapping potential depends on the number of ”poles”, and the trapping potential V is given by[35]

$$V \propto r^{m/2} \cos\left(\frac{m}{2}\theta\right) \tag{2.1}$$

where m is the number of ”poles”, r is the distance from the equilibrium position, and θ is the angle from a symmetric axis of the multipole.

In this work, we focus on quadrupole fields. An electric quadrupole field is given by

$$V(x, y, z) = \frac{V_0}{2R_0^2}(\alpha x^2 + \beta y^2 + \gamma z^2) \tag{2.2}$$

Maxwell’s equation $\nabla \cdot \mathbf{E} = -\Delta V = 0$ restricts the coefficients as

$$\alpha + \beta + \gamma = 0 \tag{2.3}$$

In the past, two-dimensional quadrupole fields were popular for mass filters and represented the simplest case of quadrupole fields. Two-dimensional quadrupole fields satisfy the condition $\alpha = -\beta = 1, \gamma = 0$. Under this condition, the electric field is given by

$$\mathbf{E} = -\nabla V = \frac{V_0}{R_0^2}(-x\hat{\imath} + y\hat{\jmath}) \tag{2.4}$$

In this electric field, charged particles are accelerated along the y-direction and will eventually hit the electrodes. To avoid this problem, scientists used periodic voltage instead of static voltage[35] . The electric force periodically changes the sign, simultaneously focusing and defocusing the particle in both the x- and y-directions. It is challenging to write down the motion of a particle directly, but it is simple to write the equation of motion using $F = ma$:

$$\ddot{x}+\frac{QV_0}{mR_0^2}\cos(\Omega t)x=0\ \ddot{y}-\frac{QV_0}{mR_0^2}\cos(\Omega t)y=0 \tag{2.5}$$

where m/Q is the mass/charge of the particle.

Mathematicians have studied this type of equation for many years and named it the Mathieu differential equation.

2.2 Mathieu Differential Equation

150 years ago, ‘Emile L’eonard Mathieu first wrote down the following equation to investigate the oscillation of an elliptic membrane[36]:

$$\frac{d^2u}{d\tau^2}+(a-2q\cos(2\tau))u=0 \tag{2.6}$$

The equation can be solved by calculating the coefficients of the Floquet expansion[37].

$$u(\tau)\approx u^{(0)}(\tau)+u^{(1)}(\tau)\quad =A_0\cos\left(\beta_u\tau\right)+A_1\cos\left(\left(\beta_u+2\right)\tau\right)+A_{-1}\cos\left(\left(\beta_u-2\right)\tau\right) \tag{2.7}$$

Substituting the expansion Eq.2.7 into the Mathieu equation Eq.2.6, we obtain the following linear equations

$$\begin{aligned}\left(A_1q+A_{-1}q+A_0\beta_u^2\right)\cos\left(\beta_u\tau\right)+\left(A_0q+A_1\left(\beta_u+2\right)^2\right)\cos\left(\left(\beta_u+2\right)\tau\right)\\+\left(A_0q+A_{-1}\left(\beta_u-2\right)^2\right)\cos\left(\left(\beta_u-2\right)\tau\right)=0\end{aligned} \tag{2.8}$$

By setting all the coefficients before the oscillating terms to zero, we obtain

$$q^2\frac{2\beta_u^2+8}{\left(\beta_u^2-4\right)^2}=\beta_u^2 \tag{2.9}$$

This equation provides a relationship between the parameters of the Mathieu differential equation, which can be useful for understanding the properties of the solutions and their applications in quadrupole trapping fields.

Substituting the coefficients into the expansion Eq. 2.7, we can obtain the approximate solution of the motion:

$$u(\tau) \approx A_0 \cos\left(\frac{q}{\sqrt{2}}\tau\right)\left(1 + \frac{q}{2}\cos(2\tau)\right) \tag{2.10}$$

Comparing Eq.2.5 and Eq.2.6, we find that Eq. 2.5 is a Mathieu equation with $a = 0, q = -\frac{2QV_0}{m\Omega^2 R_0^2}$, whose approximate solution is:

$$x(t) \approx A_0 \cos\left(\frac{QV_0}{\sqrt{2}m\Omega R_0^2}t\right)\left(1 - \frac{QV_0}{m\Omega^2 R_0^2}\cos(\Omega t)\right), \tag{2.11}$$

where $r_{\text{micromotion}} = \frac{QV_0}{m\Omega^2 R_0^2}$ represents the strength of unavoidable micromotion, and $\omega_{\text{trap}} = \frac{QV_0}{\sqrt{2}m\Omega R_0^2}$ represents the trap frequency. If we naively increase the trap frequency by increasing the power of the RF field, the amplitude of the unavoidable micromotion would also increase. Considering the ratio between these two parameters, we obtain $\omega_{\text{trap}} = \frac{\Omega}{\sqrt{2}} r_{\text{micromotion}}$, which means that if we want to increase the trap frequency without increasing the amplitude of micromotion, we should simultaneously increase the RF power and the RF frequency.

2.3 Pseudopotential

Eq. 2.11 shows that the secular motion of an ion follows the form of a harmonic oscillator. The emergence of harmonic motion can also be understood from the perspective of pseudopotential. The ion's motion under an oscillating electric field is determined by the following equation of motion:

$$m\ddot{\vec{r}}(t) = Q\vec{E}(\vec{r}(t))\cos\Omega t \tag{2.12}$$

There is no general way to analytically solve Eq. 2.12 due to the composite function $\vec{E}(\vec{r}(t))$. To obtain an approximate description of the ion's motion under an oscillating field, we need to separate the mutual dependency between the electric field and ion's motion. We can assume the ion's motion is much slower than the oscillating speed of the electric field, and then approximate $\vec{r}(t) \approx \vec{r}(t_0) + \delta\vec{r}$ and $\vec{E}(\vec{r}(t)) \approx \vec{E}(\vec{r}(t_0))$.

The pseudopotential $\Phi(\vec{r})$ is a time-averaged behavior of an oscillating electric field, which can be presented as:

$$\vec{F}\text{coarse} = \frac{1}{T}\int 0^T Q\vec{E}(\vec{r}(t))\cos\Omega t dt \approx -Q\nabla\Phi(\vec{r}). \tag{2.13}$$

Since in ion traps the oscillating fields are periodic and we assume the ion's motion is much slower than the oscillating speed, the first-order term in the averaged force is zero:

$$\int_0^T Q\vec{E}(\vec{r}(t))\cos\Omega t dt \approx \int_0^T Q(\vec{E}(\vec{r}(t_0)) + \delta\vec{E})\cos\Omega t dt = \int_0^T Q\delta\vec{E}\cos\Omega t dt, \tag{2.14}$$

where $\delta\vec{E} = (\delta\vec{r}\cdot\nabla)\vec{E}(\vec{r}(t_0))$ can be calculated by Taylor expansion. To calculate $\delta\vec{E}$, we first simplify Eq. 2.12 to:

$$m\delta\ddot{\vec{r}}(t) = Q\vec{E}(\vec{r}(t_0))\cos\Omega t \tag{2.15}$$

Then, we obtain:

$$\delta\vec{r}(t) = \frac{Q\vec{E}(\vec{r}(t_0))}{m\Omega^2}(1-\cos\Omega t) \tag{2.16}$$

And also:

$$\delta\vec{E} = \frac{Q}{m\Omega^2}(1-\cos\Omega t)(\vec{E}\cdot\nabla)\vec{E} = \frac{Q}{2m\Omega^2}(1-\cos\Omega t)\nabla|\vec{E}|^2 \tag{2.17}$$

Substituting Eq.2.17 into Eq.2.14, we can get (set $T = \frac{2\pi}{\Omega}$):

$$\vec{F}\text{coarse} \approx \frac{1}{T}\int 0^T Q\delta\vec{E}(\vec{r}(t))\cos\Omega t dt = -\frac{Q^2}{4m\Omega^2}\nabla|\vec{E}|^2 = -Q\nabla\Phi \tag{2.18}$$

Therefore, the pseudopotential can be approximated as:

$$\Phi \approx \frac{Q}{4m\Omega^2}|\vec{E}(\vec{r})|^2 \tag{2.19}$$

2.4 Geometric structure and motional modes

In this section, we primarily discuss simulating the classical mechanical properties of ion crystals, such as geometry, mode frequencies, and so on. The classical interaction potential energy of ions confined by a Paul trap can be expressed as follows:

$$V = \sum_i \frac{1}{2} m\omega_x^2 \left[x_i^2 + \left(\frac{\omega_y}{\omega_x}\right)^2 y_i^2 + \left(\frac{\omega_z}{\omega_x}\right) z_i^2 \right] + \sum_{i<j} \frac{e^2}{4\pi\epsilon_0 \sqrt{(x_i - x_j)^2 + (y_i - y_j)^2 + (z_i - z_j)^2}},$$

To remove dimensions, we can define $x_i = lu_i$, $y_i = lv_i$, and $z_i = lw_i$, resulting in

$$\frac{V}{m\omega_x^2} = l^2 \sum_i \frac{1}{2} \left(x_i^2 + r^2 v_i^2 + s^2 w_i^2 \right) + \frac{e^2}{4\pi\epsilon_0 m\omega_x^2 l} \sum_{i<j} \frac{1}{\sqrt{(u_i - u_j)^2 + (v_i - v_j)^2 + (w_i - w_j)^2}},$$

where $r = \omega_y/\omega_x$ and $s = \omega_z/\omega_x$. To make the potential energy dimensionless, we need

$$l^2 = \frac{e^2}{4\pi\epsilon_0 m\omega_x^2 l}$$

Then, $l^3 = e^2/(4\pi\epsilon_0 m\omega_x^2)$, and the potential energy can be transformed into a dimensionless form

$$\frac{V}{m\omega_x^2 l^2} = \sum_i \frac{1}{2} \left(u_i^2 + r^2 v_i^2 + s^2 w_i^2 \right) + \sum_{i<j} \frac{1}{\sqrt{(u_i - u_j)^2 + (v_i - v_j)^2 + (w_i - w_j)^2}} \tag{2.20}$$

When ions crystallize, their geometry automatically minimizes the value of the potential given by Eq.2.20. To theoretically simulate the equilibrium positions, we typically numerically minimize the potential energy from Eq.2.20 to obtain dimensionless parameters u_i, v_i, and w_i, and then add the dimension l to solutions to acquire the real space position by $x_i = lu_i$, $y_i = lv_i$, and $z_i = lw_i$.

As ions crystallize, we can calculate their collective motional normal modes based on classical mechanics. Considering ions moving in a three-dimensional space, the classical Hamiltonian in real space coordinates can be written as a summation of kinetic energy and potential energy:

$$\mathcal{H} = \frac{1}{2} m \sum_i (\dot{x}_i^2 + \dot{y}_i^2 + \dot{z}_i^2) + V(x_i, y_i, z_i)$$

When ions crystallize, we can assume ions move very slightly around their equilibrium positions, and use the deviation $\eta_{xi} = x_i - x_{i,0}$ from the equilibrium positions as generalized coordinates. Then we can perturb the potential energy using Taylor expansion:

$$V = \nabla V(\eta) \cdot \eta + \frac{1}{2}\eta^T H\eta,$$

where $\eta = (\cdots, \eta_{xi}, \cdots, \eta_{yi}, \cdots, \eta_{zi}, \cdots)$, and $H_{ij} = \partial V/\partial\eta_i\eta_j$ is the Hessian matrix. Since ions are in equilibrium positions, the first-order term vanishes, $\nabla V(\eta) \cdot \eta = 0$. The classical Hamiltonian can be rewritten as

$$\mathcal{H} = \frac{1}{2}\dot{\eta}^T\eta + \nabla V(\eta) \cdot \eta + \frac{1}{2}\eta^T H\eta, \tag{2.21}$$

Next, we can perform a linear transformation $\eta = U\rho$ to diagonalize the quadratic form in Eq. 2.21, yielding

$$\mathcal{H} = \frac{1}{2}m\dot{\rho}^T U^T U\dot{\rho} + \frac{1}{2}\rho^T U^T HU\rho = \frac{1}{2}m\dot{\rho}^T\dot{\rho} + \frac{1}{2}\rho^T U^T HU\rho.$$

We can solve for the matrix U to diagonalize H by $U^T HU = K$, where K is a diagonal matrix. Then we obtain a Hamiltonian of a set of independent classical harmonic oscillators:

$$\mathcal{H} = \frac{1}{2}m\dot{\rho}^T\dot{\rho} + \frac{1}{2}\rho^T K\rho = \sum_i \frac{1}{2}m\dot{\rho_i}^2 + \frac{1}{2}k_i\rho_i^2.$$

From this, we can obtain mode frequencies as $\sqrt{k_i/m}$.

For our dimensionless potential energy $\tilde{V} = V/(m\omega_x^2 l^2)$, we can directly diagonalize the Hessian matrix $\tilde{H}$ corresponding to $\tilde{V}$ to obtain a diagonal matrix $\tilde{K}$ with diagonal elements $\tilde{k}_i$. Then, we have

$$\tilde{H}_{ij} = \frac{\partial^2\tilde{V}}{\partial\eta_i\partial\eta_j} = \frac{1}{m\omega_x^2}\frac{\partial^2 V}{\partial qiqj} = \frac{1}{m\omega_x^2}H_{ij}, \tag{2.22}$$

where q_i represents real space coordinates x_i, y_i, z_i. Eq. 2.22 indicates that the eigenvalues of the real space Hessian matrix are $k_i = m\omega^2 x\tilde{k}i$. Thus, we can first diagonalize the dimensionless Hessian matrix $\tilde{H}$ to obtain eigenvalues $\tilde{k}_i$, and calculate the mode frequencies by

$$\omega_i = \sqrt{\frac{k_i}{m}} = \omega_x\sqrt{\tilde{k}_i}$$

2.5 Qubits encoded with trapped ions

2.5.1 Types of qubits

The simplest ions that can be used to encode qubits are hydrogen-like ions, which have only one electron in their valence shell. Compared to more complex ions with multiple valence electrons, hydrogen-like ions exhibit simpler energy structures and closed-cycle optical transitions between the ${}^2S_{1/2}$ and ${}^2P_{1/2}$ manifolds, which can be easily manipulated by lasers. Typically, the most frequently used ions possess only two electrons in their outermost shell, with all other inner shells being either completely filled or empty. Therefore, all Group IIA elements of the periodic table can be employed. Group IIA elements include Beryllium (Be), Magnesium (Mg), Calcium (Ca), Strontium (Sr), Barium (Ba), and Radium (Ra). In addition to Group IIA elements, other elements that meet this requirement can be predicted based on the filling order of atomic orbitals. As depicted in Fig. 2.1, when the s shell is fully filled, electrons can still be added to the inner shell. This category of elements includes Helium (He, $1s^2$), Zinc (Zn, $3d^{10}4s^2$), Cadmium (Cd, $4d^{10}5s^2$), Ytterbium (Yb, $4f^{14}6s^2$), Mercury (Hg, $4f^{14}5d^{10}6s^2$), Nobelium (No, $5f^{14}7s^2$), and Copernicium (Cn, $5f^{14}6d^{10}7s^2$).

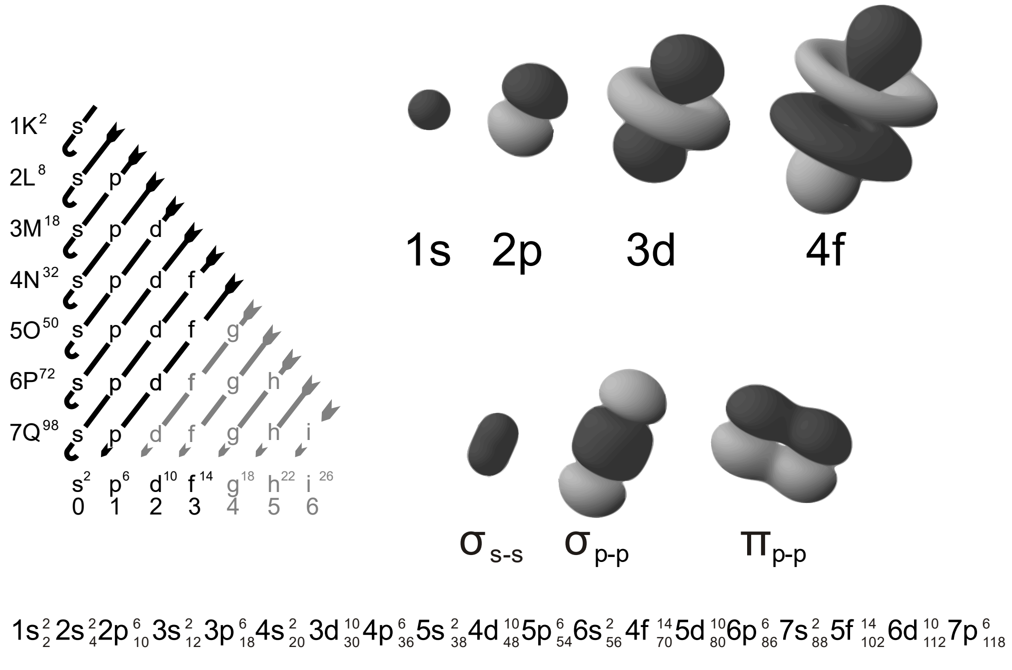

Figure 2.1 Electron orbitals

Depending on the choice of energy level, there are three methods for encoding qubits: encoding into optical energy levels with optical transition, encoding into optical energy levels of the ground state manifold, and encoding into optical energy levels of metastable manifolds. Qubits can be encoded into the ground states of ions. For ions without nuclear spin, qubits are encoded into the Zeeman states of the S manifold, often referred to as Zeeman qubits. For ions with nuclear spin, qubits are typically encoded into the clock state of hyperfine energy levels, often called clock state qubits, and the clock states consist of two $m_F = 0$ states in the hyperfine manifold. Clock states' energies are first-order insensitive to magnetic field fluctuations due to $m_F = 0$, and also to qubit splitting. Consequently, qubits encoded in clock states can have long coherence times exceeding 1 hour[38]. Qubits can also be encoded into energy levels with optical transitions, such as using a state in the ground state manifold as $|0\rangle$ and a state in a metastable manifold as $|1\rangle$. This encoding method is often called an optical qubit. Compared to clock state qubits, optical qubits can exhibit better detection efficiency due to larger energy splitting of the qubit, which reduces off-resonant coupling. Meanwhile, states in metastable manifolds also have relatively long lifetimes and $m = 0$ states, so optical qubits can also maintain relatively long coherence times. Qubits encoded into energy levels of metastable manifolds are referred to as metastable state qubits. Metastable state qubits can be utilized as memory to temporarily store information during cooling or detection[39].

2.5.2 Initialization

To use qubits encoded in ions' internal states, we must first initialize the qubits into a specific state. The technical details for different types of qubits and energy level structures may vary, but the main idea involves using a laser to generate a single dark state.

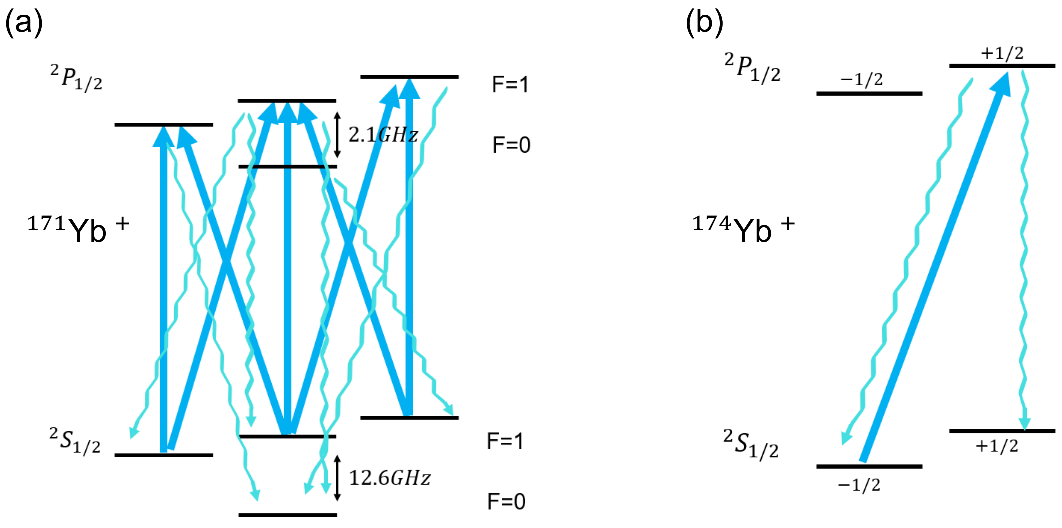

Figure 2.2 Clock state qubit and Zeeman qubit initialization

Fig.2.2 illustrates the initial state preparation methods for clock state qubits and Zeeman qubits. In Fig.2.2(a), the initialization of a clock state qubit is achieved by simultaneously exciting the $F = 1$ states in the S manifold to the $F = 1$ states in the P manifold, leaving the $F = 0$ state in the S manifold uncoupled. Since the transition cycle is not closed, the population is continuously pumped into the $F = 0$ state in the S manifold. This scheme will not work if we excite the $F = 1$ states in the S manifold to the $F = 0$ state in the P manifold, as the transition from the $F = 0$ state in the P manifold to the $F = 0$ state in the S manifold is forbidden. In Fig. 2.2(b), the initialization of a Zeeman qubit is accomplished by using only a σ_+ laser to excite ions, causing the population in the $m = -1/2$ state to be pumped into the $m = +1/2$ state. This method is sensitive to the laser's polarization, and if any σ_- or π component exists, the fidelity of the qubit initialization will decrease.

The initialization method for optical qubits is the same as the method for clock state qubits or Zeeman qubits. An optical qubit typically consists of at least one state in the ground state manifold, and the state in the ground state manifold can be prepared using the methods described above.

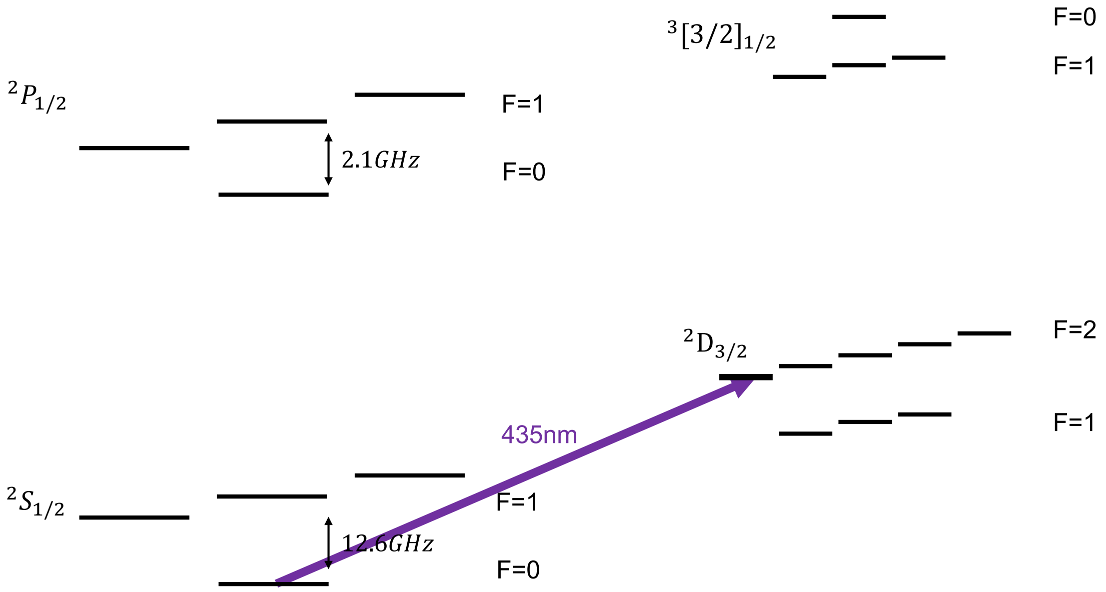

Figure 2.3 Optical qubit initialization

Fig. 2.3 displays an optical qubit in a $^{171}\text{Yb}^+$ ion. To initialize this optical qubit, we can use the same method for the clock state qubit, since the $|0\rangle$ state of the clock state qubit and the optical qubit is encoded into the same energy level.

For metastable state qubits, population transfer is required. We first use the method described in Fig. 2.2 to initialize the ion's internal state into the $F = 0$ state in the S manifold. For example, if we want to initialize a qubit in the metastable manifold ${}^2F_{7/2}$ of ${}^{171}\mathrm{Yb}^+$, we need to first initialize a clock state qubit in the S manifold, and then transfer the population to the ${}^2F_{7/2}$ manifold, as shown in Fig.2.4. Alternatively, we can first prepare a coherent state of a clock state qubit and then coherently transfer it into a metastable state qubit[39].

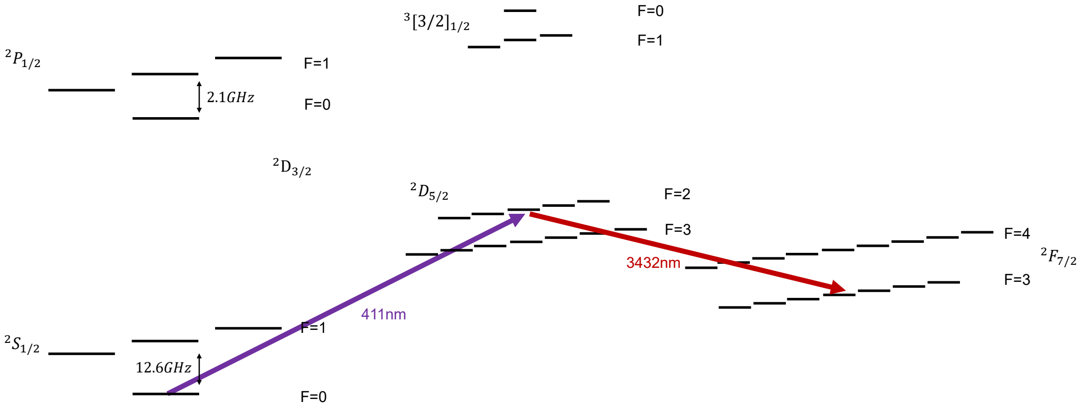

Figure 2.4 Metastable state qubit initialization

2.5.3 Operation

There are two primary methods to manipulate the qubit encoded in ions. The first is to directly drive the qubit states, where the frequency of the external driving field exactly matches the qubit splitting. For clock state qubits, Zeeman qubits, and metastable state qubits, the qubit splittings are typically in the giga or mega Hertz level, and the external driving fields are often microwaves. For optical qubits, the qubit splitting is in the optical range, and the external driving fields are usually visible lasers. Since the external driving field interacts with the ion's motional degree of freedom through the dependency of laser phase $\vec{k} \cdot \vec{x}$, microwaves typically cannot drive the motional modes of ions due to their small wave vector $\vec{k}$. One way to solve this limitation is to use a spatial magnetic field gradient[40-41], where the magnetic field gradient adds a spatial dependency of qubit energy splitting.

$$\hat{H}\text{lab} = \frac{\hbar\omega 0}{2}\hat{S}z + \hbar\nu\hat{a}^{\dagger}\hat{a} + \hbar\Omega 0\hat{S}(e^{i(k\hat{x}-\omega t)} + \text{h.c.}) + \hbar\vec{S}\cdot\Delta\vec{B}(\vec{x}), \tag{2.23}$$

where $\Delta\vec{B}(\vec{x}) = (\vec{x}\cdot\nabla)\vec{B}$. The red term represents the effect of the magnetic field gradient on the ion, and by changing which component of the magnetic field has a gradient and which one of x, y, z the gradient is dependent on, we can realize $\hat{S}_i\hat{j}$, where

$i, j \in x, y, z$. For instance, if we want to generate $\hat{S}_y \hat{x}$, we can use a magnetic field $\vec{B} = (0, \Omega_g x, B_0)$, where Ω_g represents the strength of the gradient.

The other method is using Raman transitions to drive qubits. Raman beams consist of visible lasers with a large wave vector, which can also drive gigahertz transitions matching their frequency difference.

2.5.4 Measurement

To measure the information stored in a qubit, we need a way to distinguish the $|0\rangle$ and $|1\rangle$ states. The main idea of measuring atomic qubits is to make only one of $|0\rangle$ and $|1\rangle$ emit fluorescence during measurement, and collect emitted photons using photon detectors. For the detection of clock state qubits, we excite the $F = 1$ states in the S manifold to the $F = 0$ state of the P manifold, as shown in Fig. 2.5(a). Since the transition from the $F = 0$ state of the P manifold to the $F = 0$ state of the S manifold is forbidden, if the ion's internal state is in $F = 1$, there will be fluorescence, and if the ion's internal state is in $F = 0$, there will be no fluorescence. If the transition were allowed, the $F = 0$ state of the P manifold could decay to the $F = 0$ state of the S manifold, and the ion could not continuously emit photons. Ideally, if the ion is in the $F = 0$ state of the S manifold, it should not emit any photons. However, the existence of $F = 1$ states in the P manifold enables the $|0\rangle$ state to emit photons through off-resonant coupling, which is the main limitation for the detection fidelity of a clock state qubit. The detection of Zeeman qubits typically involves shelving qubits to a metastable state, since the lack of hyperfine structure makes it difficult to find a forbidden transition. As shown in Fig. 2.5(b), to detect a Zeeman qubit, we first need to shelve one of the qubit states into another state outside the detection cycle, and then turn on the detection beam to continuously excite fluorescence. The detection of optical qubits is similar to the detection of Zeeman qubits.

The detection of metastable qubits requires repumping the population from the metastable state back to the ground state to excite fluorescence. As shown in Fig. 2.5(c), we first need to apply a 3432 nm laser without an additional sideband to selectively repump one of the qubit states back to the $^2\mathrm{D}_{5/2}$ state, and then use a 976 nm laser to repump the population back to the ground state manifold.

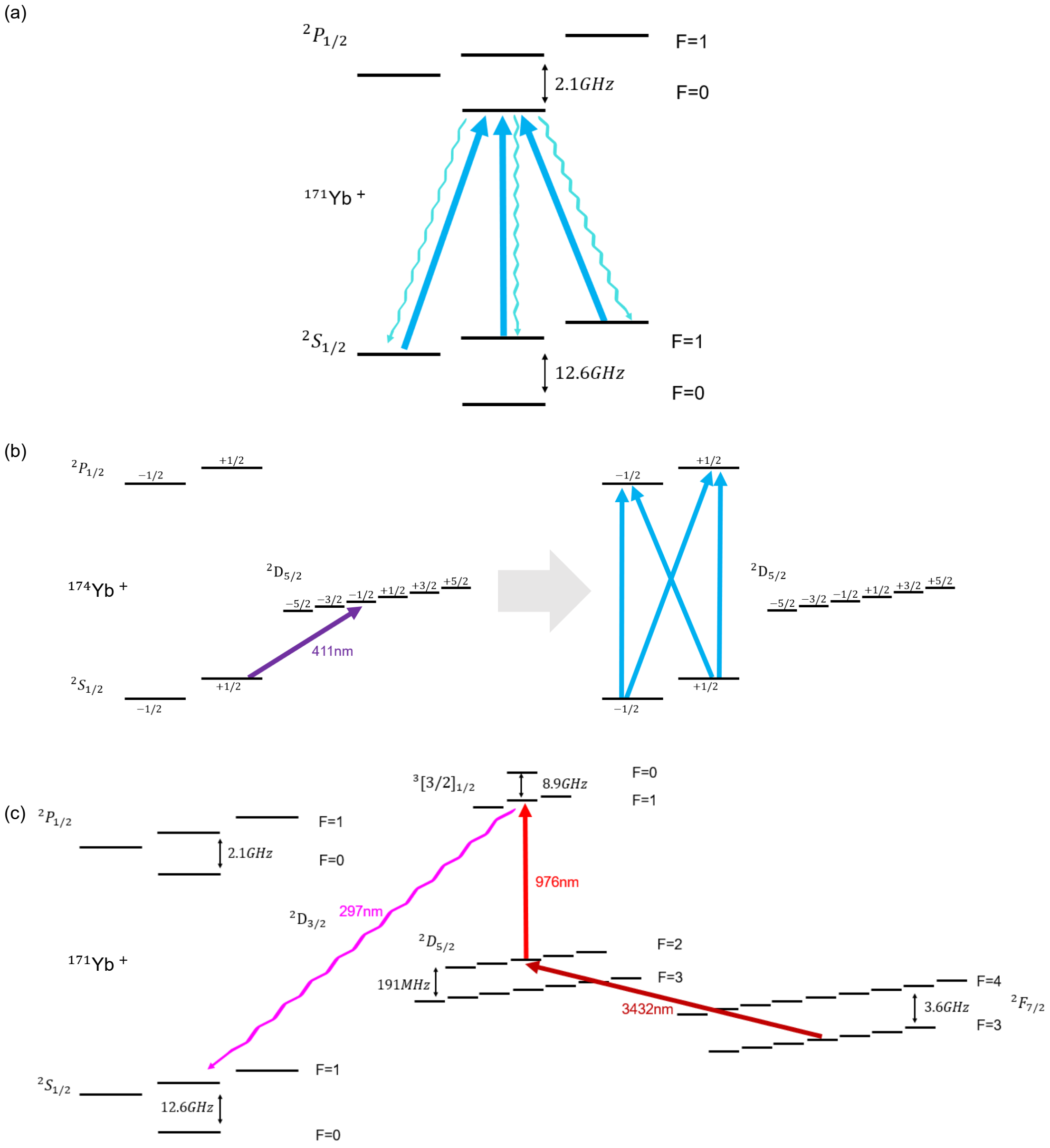

Figure 2.5 Qubit measurement methods.
(a) Detection scheme of clock state qubit. (b) Detection scheme of Zeeman qubit. (c) Detection scheme of metastable state qubit.

CHAPTER 3 EXPERIMENT SETUP

3.1 The vacuum setup

3.1.1 Baking procedure

During the baking procedure, we used three different vacuum pumps: a turbopump, a big ion pump, a small ion pump, and a getter pump, as shown in Fig. 3.1. The turbopump reduces the vacuum level from atmospheric pressure to High Vacuum (HV). The big ion pump brings the system from the HV region to the Ultra-High Vacuum (UHV) region. The small ion pump and the getter pump are used for daily operations. Typically, the ion pump works in an environment where the pressure is below 10^{-6}mBar, and we usually use it after the turbopump reduces the pressure to that level.

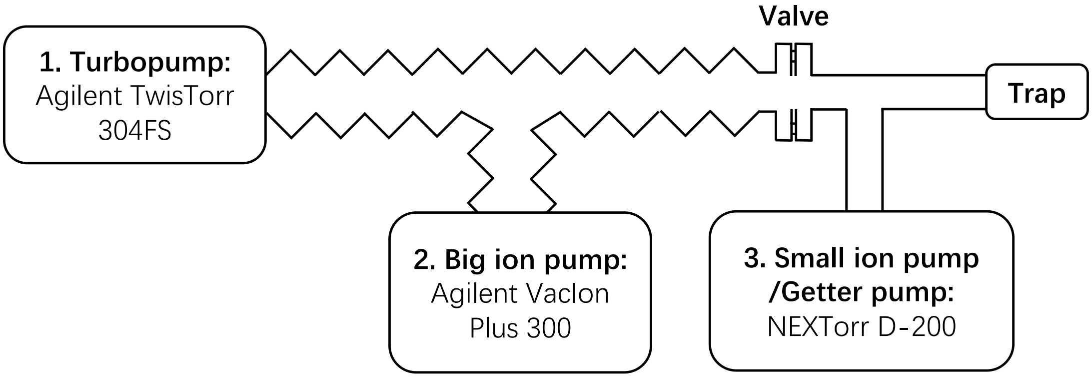

Figure 3.1 Vacuum pumps used during baking
The three vacuum pumps used during baking. The turbopump and big ion pump are purchased from Agilent, and the small ion pump and getter pump are obtained from SAES Getters.

Table.3.1 presents the baking procedure. The baking process is primarily conducted at 150 °C. The turbopump remains open throughout the baking process, while the big ion pump is opened when the turbopump cannot further reduce the pressure. As depicted in Fig.3.1, both the turbopump and the big ion pump are placed outside the chamber and are used only for baking. These two pumps handle the majority of the baking process. The small ion pump and the getter pump are not used during baking, and we open them only for degassing contamination. The degassing for the ion pump is relatively quick; typically, rapidly opening and closing the ion pump several times is sufficient. However,

Table 3.1 Baking procedure

Time	IMG (mBar)	Big ion pump (mBar)	Small ion pump	Temperature	Other operations
08/14 17:00	7.8×10^{-6}	closed	closed	25	Start baking, increase T
08/15 10:00	6.7×10^{-8}	closed	closed	150	
08/15 10:00	6.7×10^{-8}	closed	closed	150	Degassing the small ion pump. Note: before opening the small ion pump we must check whether the pressure below 10^{-5} Torr
08/15 10:01	7.0×10^{-7}	closed	closed	150	Degassing make vacuum a little bit worse
08/15 10:10	6.5×10^{-8}	closed	closed	150	Start conditioning, pressure begin to increase
08/15 10:11	7.1×10^{-7}	closed	closed	150	Wait the pressure decrease
08/15 10:50	4.4×10^{-8}	closed	closed	150	Open the big ion pump
08/15 10:51	3.7×10^{-8}	9.9×10^{-9}	closed	150	
08/16 8:00	7.6×10^{-9}	1.1×10^{-9}	3.4×10^{-9} mBar (222nA)	150	
08/16 17:58	6.9×10^{-9}	9.8×10^{-9}	closed	150	Begin to decrease the temperature
08/16 22:50	4.9×10^{-9}	8.2×10^{-9}	closed	100	Start TmdActivation mode
08/16 23:50	3.0×10^{-8}	1.8×10^{-7}	closed	100	During the activation, hydrogen go out and make the vacuum worse.
08/16 23:53	6.3×10^{-9}	3.8×10^{-8}	closed	100	
08/17 02:46	4.4×10^{-9}	8.0×10^{-9}	6nA	100	The hydrogen had been clear out. Isolate the trap (close the valve) and decrease the temperature

the activation process for the getter pump takes several hours, and after activation, we need to wait for the hydrogen released during the activation process to be absorbed by the big ion pump and the turbopump. After degassing and activation, we isolate the vacuum chamber from the big ion pump and the turbopump by closing the valve. For the UHV valve we used, we must ensure that each time we close the valve, the torque applied is slightly greater than the previous time. This requires us to record the torque used for closing the valve.

3.1.2 The vacuum chamber

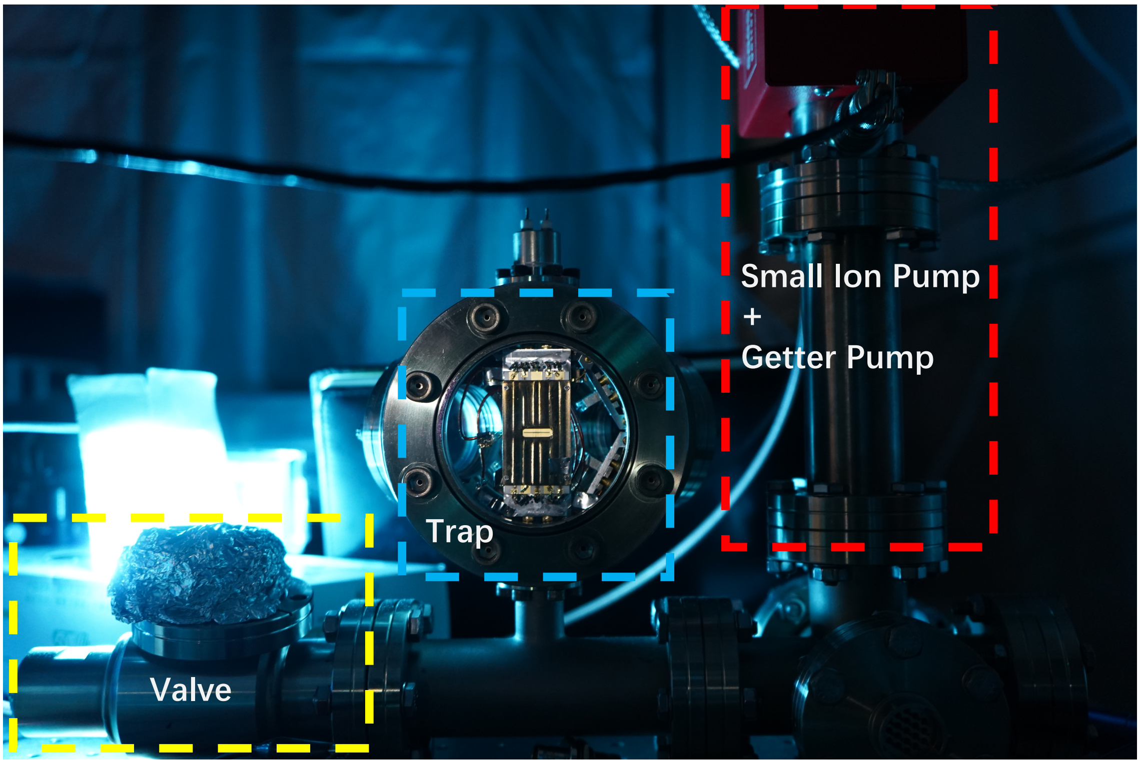

Figure 3.2 The vacuum chamber
The vacuum chamber consists of three main parts: valve, trap, and ion&getter pump.

As depicted in Fig. 3.2, we use a hemispherical chamber to hold the trap, which is placed at the front of the largest viewport. The vacuum chamber can be separated into three parts: valve part, trap part, and pump part. The valve part is used only before baking. The trap part houses the trap and contains ovens and electrodes connected inside. The pump part is responsible for maintaining the UHV environment. In previous experiments, we found that the 355nm pulsed laser could induce accumulated charges on the viewport, causing ion shifts during Raman operation. In our latest version, we use a metallic mask to shield charges accumulated on the viewport. The largest viewport is also used for imaging ions, while the other viewports are primarily used for transmitting operation lasers. On top of the hemispherical chamber, a feedthrough is used for transmitting RF power. At the bottom of the hemispherical chamber, a thin neck connects the hemispherical chamber and the other parts. Due to the neck's diameter being only 16 mm, the vacuum conductance of the neck is limited. In the next version, we could add a non-evaporable getter inside the hemispherical chamber to improve the vacuum.

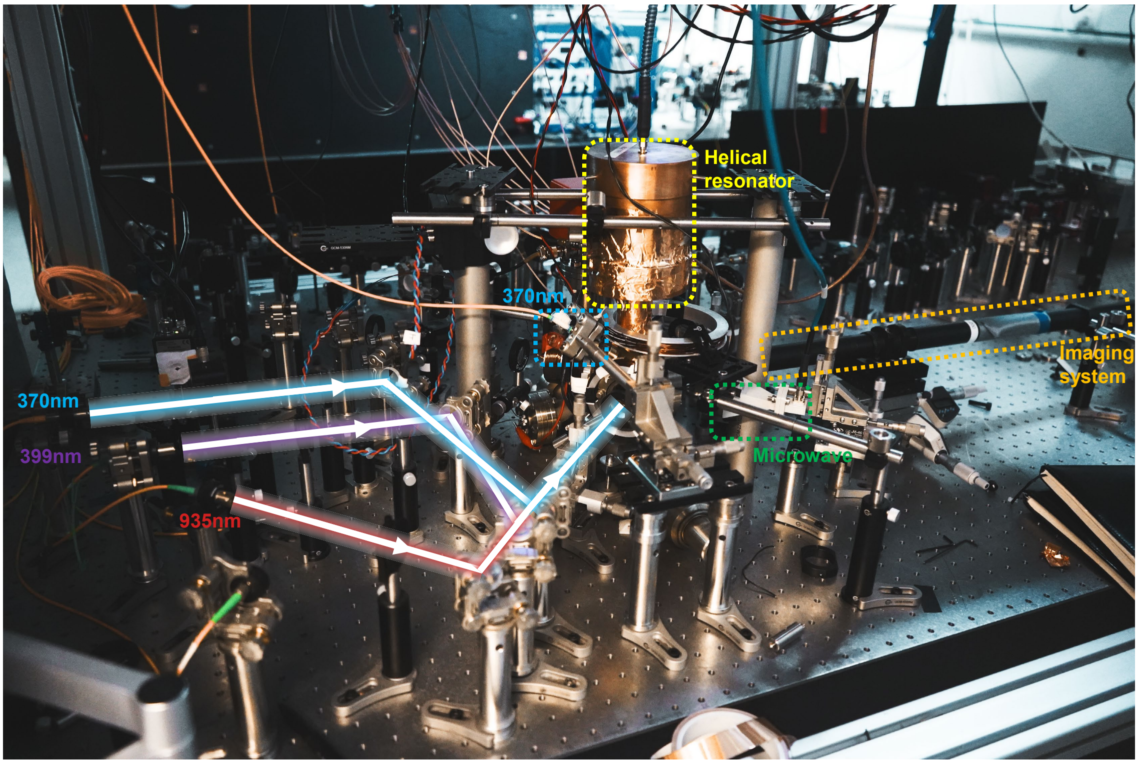

Figure 3.3 The whole system
The whole system consists of the vacuum chamber, the helical resonator, and the optical elements.

Fig. 3.3 illustrates the external setup around the vacuum chamber. At the top of the vacuum chamber, a helical resonator is placed to filter and amplify the RF signal. The orange square indicates the position of the imaging system, where a long tube is used to hold lenses inside. The green square shows a horn used to generate microwaves, which are primarily used for calibrating camera detection. The 370nm, 399nm, and 935nm lasers are combined by two dichromatic mirrors. The blue square displays an additional 370nm laser used for cooling down the vertical motional mode. This is necessary because, during 2D experiments, one of the motional modes is vertical and cannot be efficiently cooled down only by the horizontal 370nm laser.

3.2 The monolithic ion trap

We have developed a Paul trap capable of producing a pancake-like harmonic potential to trap a 2D crystal of ions and set the direction of micromotions on the plane of the 2D crystal. The trap is a three-dimensional monolithic trap[42-44] constructed on a single layer of gold-plated laser-machined alumina[45-46]. Fig. 3.4 illustrates the structure of our trap. In this configuration, the 2D crystals of ions reside in the z-x plane, which is achieved by compressing the harmonic potential along the y-axis, where the micromotion occurs along the z-axis. The net-propagation direction of the Raman laser beam is along the y-axis, which is perpendicular to the direction of micromotion. Consequently, quantum operations performed by Raman laser beams will not be affected by the micromotion.

The trap is functionally divided into three layers: the front and back layers contain dc electrodes, and the middle layer serves as the RF electrode, as conceptually depicted in Fig. 3.4(a). The RF electrode has a slope with an angle of 45° relative to the normal direction of the alumina piece. In each DC layer, there are ten electrodes, with five on both the upper and lower sides and a 50 μm spacing. At the trap's center, a 260 μm × 4 mm slot is present, where ions are trapped. Fig. 3.4(b) displays the trap's front side. The angle of the slope and the gap between DC and RF electrodes are optimized to maximize the trap frequency. We employ CPO (Charged Particle Optics) software to calculate the electric potential generated by the electrodes. We also compare the simulated potential with the real potential to calibrate the simulation coefficient for further trap simulation. In the experiment, only six of the twenty electrodes are connected to the stable DC sources, while the others are connected to GND, as shown in Fig. 3.4(b).

The monolithic trap is situated inside a vacuum chamber depicted in Fig. 3.4(c). The trap and vacuum system are designed to ensure sufficient optical access. $^{171}\mathrm{Yb}^+$ ions are loaded into the middle of the trap through photo-ionization and Doppler cooling[47]. We create a 2D crystal of ions in a plane that consists of the axial axis (x-axis) and one of the radial axes (z-axis). We apply two Doppler-cooling laser beams to couple all three directions of ion motions, as shown in Fig. 3.4(a). The magnetic-field insensitive states of $^{171}\mathrm{Yb}^+$ ions in the ground-state manifold $^2S_{1/2}$, $|F=0, m_F=0\rangle$, and $|F=1, m_F=0\rangle$ are mapped to qubit states $|0\rangle$ and $|1\rangle$, respectively. The qubit state is detected by the laser beam resonant to the transition between $F=1$ of $^2S_{1/2}$ and $F=0$ of $^2P_{1/2}$ and initialized to $|0\rangle$ by applying the optical pumping laser beam resonant with the transition between $F=1$ of $^2S_{1/2}$ and $F=1$ of $^2P_{1/2}$. The qubit is coherently manipulated by a pair of 355 nm picosecond pulse laser beams with a beatnote frequency close to the qubit transition $\omega_0 = 2\pi \times 12.642821$ GHz.

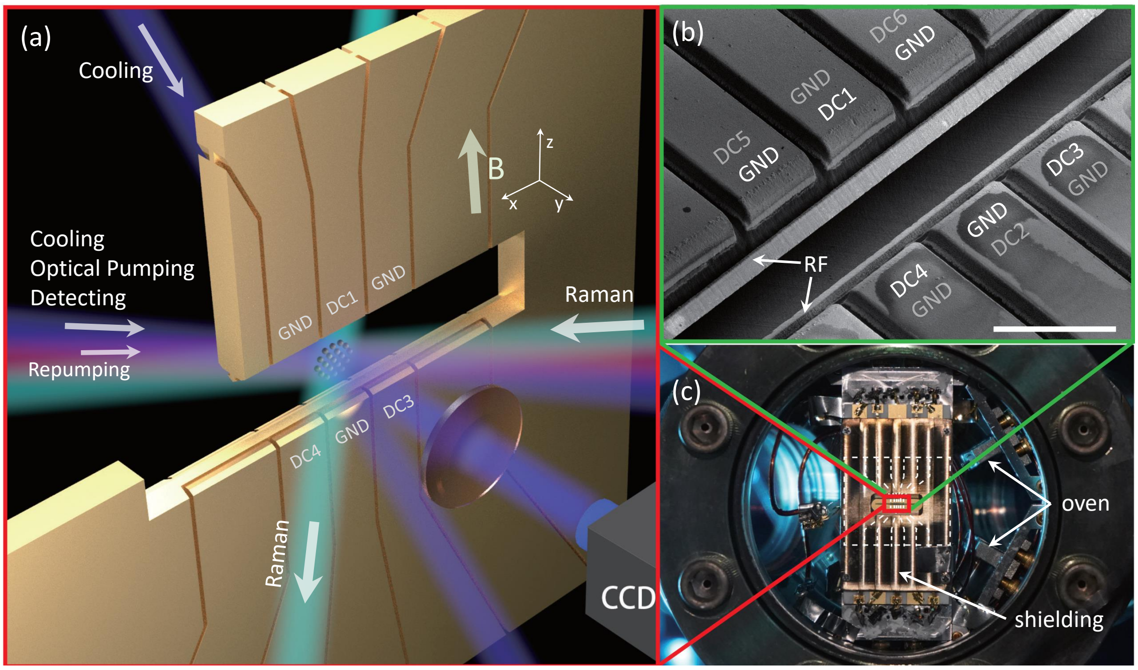

Figure 3.4 Trap structure and beam configuration.
(a) Conceptual drawing of our trap and the configuration of laser beams for cooling, pumping, detection (370 nm and 935 nm) and coherent operations (355 nm). The magnetic field is applied vertically. (b) Scanning electron microscope (SEM) image of our trap (white scale bar, 400 μm). The trap structure is laser-machined on a single piece of alumina with less than 10 μm precision. Gold is electro-plated on the surface of alumina with 10 μm thickness. The trap has a total of 20 electrodes, where fourteen of them are connected to GND and the others to DC sources. The gray letters label the electrodes on the opposite side of the trap.(c) Image of our monolithic trap mounted in a hemi-sphere vacuum chamber. The trap is shielded with stainless steel plates on the front and back, respectively, which are connected to GND. The dashed lines show the electrodes underneath the shield.

3.2.1 Fabrication processes

The substrate is a single piece of alumina with a thickness of 380 μm and a surface flatness of less than 30 nm. The electronic structure is fabricated by laser-machining and coated with 3 μm gold using electroplating technology. The detailed procedure to fabricate the electrode structure is as follows: 1) Carve a 260 μm slot at the center of the piece, as shown in Fig. 3.6(a); 2) Create a 45° slope on each side by cutting small steps to fit the slope, as shown in Fig. 3.6(b); 3) Make a tiny groove on each slope with a width of around 50 μm; 4) Apply gold coating on both sides of the chip, as shown in Fig. 3.6(c); 5) Cut deeper in the groove position to remove gold, electrically separating the center layer from the top and bottom layers; 6) Laser cut the slots on the top and bottom layers to electrically separate all DC electrodes. Among all the steps, the second is the most

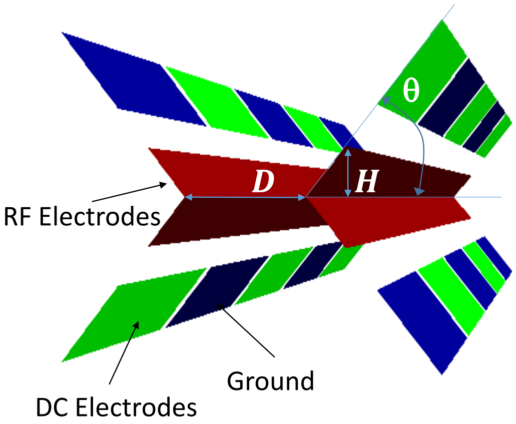

Figure 3.5 Important geometric parameters for the trap design
We generate 3D models with all combinations of three parameters and calculate the pseudo-potential and the secular frequency with CPO software. Maximizing the secular frequencies given fabrication limitation and laser-light scattering, we choose $D = 260\ \mu$m, $\theta = 45^\circ$ and $H = 40\ \mu$m for the trap.

subtle one. The geometry of the four slopes is crucial for ion control with DC voltages. In step 2), for each slope, we apply 40 laser cutting iterations with different durations and a 5 μm shift in cutting position. The cutting duration for each pulse is calculated based on the calibrated relationship between cutting depth and cutting time. The laser cutting precision is $\pm 1\ \mu$m, limited by worktable instability. Using a laser with a power of 2W, a wavelength of 355 nm, and a beam waist of around 15 μm, we achieve a cutting speed of 100 mm/s.

3.2.2 Structure of the trap

We use CPO software to simulate the trap performance with various geometric parameters. There are three important parameters for the trap design: the distance between two RF electrodes D, the height of RF electrodes H, and the angle of the slope θ, as shown in Fig. 3.5. We optimize these three parameters primarily to achieve large secular frequencies in the radial direction, given fabrication limitations. The secular frequency is approximately inversely proportional to D^2[37], which is confirmed in our numerical simulation. We balance the requirement of a large trap frequency and low UV-light scattering, leading to the choice of $D = 260\ \mu$m. For the slope angle θ, our simulation shows the best performance at $\theta \approx 47^\circ$. Due to the fabrication difficulty of the angle, we choose $\theta = 45^\circ$. Our simulation shows the best value of H is around 30 μm. Considering the laser cutting precision, we decide on $H = 40\ \mu$m.

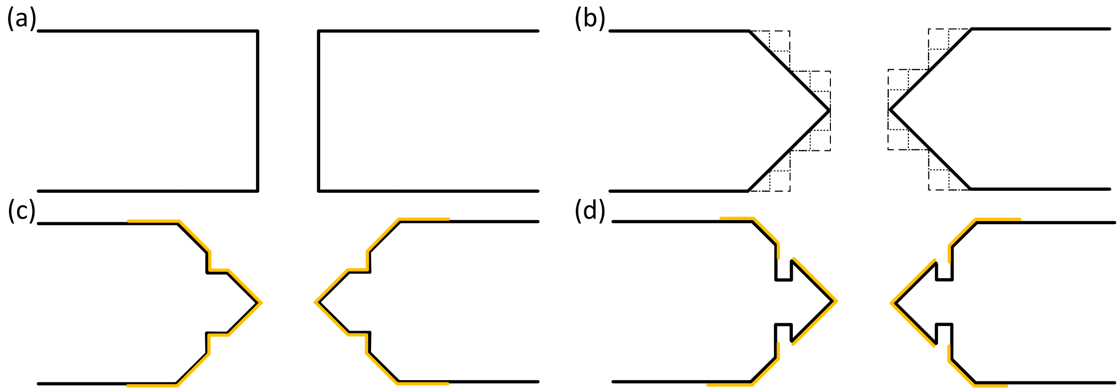

Figure 3.6 Steps for fabricating the structure of electrodes.
(a) Laser cut the 260 μm slot. (b) Cut 40 small steps for each slope with 45°. (c) Laser cut the small groove and electroplate gold on the surface. (d) Cut the slots on the grooves and two sides of the chip to electrically separate all DC and RF electrodes.

3.2.3 Trap simulation calibration

Due to fabrication imperfections, the actual trap potential may deviate from the ideal model in the simulation. We develop a method to quantitatively calibrate the differences between reality and simulation, which is useful for further simulations and predictions of trap behavior. Taking $\phi_{\mathrm{C}}(x,0,0)$ as an example, we can describe the difference between reality and simulation as follows:

$$\phi_{\mathrm{real,C}}(x,0,0) = \eta_{\mathrm{C,x}}\phi_{\mathrm{sim,C}}(x,0,0), \tag{3.1}$$

where $\phi_{\mathrm{real,C}}(x,0,0)$ is the actual potential generated by electrode $\mathrm{DC_C}$ along the x-axis, ϕsim, C$(x,0,0)$ is the simulated potential, and $\eta_{\mathrm{C,x}}$ is the imperfection coefficient for $\mathrm{DC_C}$ in the x-axis. We study the relationship between the actual axial trap frequency and the simulated axial trap frequency to calibrate $\eta_{\mathrm{C,x}}$.

We begin by calculating the axial mode frequency, which is $\omega_{\mathrm{x}} = \sqrt{\partial^2\phi(x,0,0)/\partial^2 x}|_{x=0}$. Using the expression of ϕ in Eq. (4.1), we obtain

$$\omega_x^2 = V_{\mathrm{C}}\frac{\partial^2\phi_{\mathrm{C}}(x,0,0)}{\partial^2 x} + V_{\mathrm{NC}}\frac{\partial^2\phi_{\mathrm{NC}}(x,0,0)}{\partial^2 x}|x = 0. \tag{3.2}$$

With Eq. (3.2) and a fixed value of VNC, we can treat ω_x^2 as a linear function of V_{C}, which has a slope $a = \frac{\partial^2\phi_{\mathrm{C}}(x,0,0)}{\partial^2 x}|x = 0$ and an intercept $b = V\mathrm{NC}\frac{\partial^2\phi_{\mathrm{NC}}(x,0,0)}{\partial^2 x}|_{x=0}$. We can write two versions of Eq. (3.2)

$$\omega^2_{\mathrm{x,real}} = a_{\mathrm{real}} V_{\mathrm{C}} + b_{\mathrm{real}}, \tag{3.3}$$

$$\omega^2_{\mathrm{x,sim}} = a_{\mathrm{sim}} V_{\mathrm{C}} + b_{\mathrm{sim}}, \tag{3.4}$$

where

$$a_{\mathrm{real}} = \frac{\partial^2 \phi_{\mathrm{real,C}}(x,0,0)}{\partial^2 x}, \tag{3.5}$$

$$a_{\mathrm{sim}} = \frac{\partial^2 \phi_{\mathrm{sim,C}}(x,0,0)}{\partial^2 x}. \tag{3.6}$$

Thus, we obtain

$$\eta_{\mathrm{C,x}} = \frac{\phi_{\mathrm{real,C}}(x,0,0)}{\phi \mathrm{sim,C}(x,0,0)} = \frac{a_{\mathrm{real}}}{a_{\mathrm{sim}}}. \tag{3.7}$$

Combining Eq. (3.3), Eq. (3.4), and Eq. (3.7), with the same value of V_{C}, we obtain

$$\omega^2_{\mathrm{x,real}} = \eta_{\mathrm{C,x}} \omega^2_{\mathrm{x,real}} + b_{\mathrm{C}}, \tag{3.8}$$

where b_{C} is an intercept determined by V_{NC} and the geometries of other electrodes. We measure the axial trap frequency $\omega_{\mathrm{x,real}}$ by adding a modulation signal to one of the DC electrodes and examining the ion image. When the modulation frequency is close to the axial mode frequency, the motion of the ion is resonantly excited and melts in the axial direction. By changing V_{C} and plotting the points $\omega^2_{\mathrm{x,real}}, \omega^2_{\mathrm{x,sim}}$ in Fig. 3.7(a), we can fit the coefficient of $\eta_{\mathrm{C,x}} = 0.97$. By performing the same measurement but only changing V_{NC}, we can obtain $\eta_{\mathrm{NC,x}} = 0.87$. $\eta_{\mathrm{C,x}}$ is close to 1, which means the geometry of the center electrodes is nearly perfect in the axial direction. On the other hand, $\eta_{\mathrm{NC,x}} = 0.87$ indicates that the $\mathrm{DC_{NC}}$ electrodes are farther away from the ion in reality than in the simulation. Whenever we want to simulate the axial potential, we need to take into account $\eta \mathrm{C,x}$ and $\eta_{\mathrm{NC,x}}$.

To calibrate the imperfection coefficients of the two radial principal axes, y-axis and z-axis, we execute the same procedure as for the axial calibration, but with more careful consideration regarding the principal-axes rotation. During the process of changing V_{NC} or V_{C}, only if we maintain the rotation angle of the principal axes within a small regime can we have similar equations to Eq. (3.8) for the y-axis and z-axis:

$$\omega^2_{\mathrm{y,real}} \approx \eta_{\mathrm{C,y}} \omega^2_{\mathrm{y,real}} + b_{\mathrm{C,y}}, \tag{3.9}$$

$$\omega^2_{\mathrm{z,real}} \approx \eta_{\mathrm{C,z}} \omega^2_{\mathrm{z,real}} + b_{\mathrm{C,z}}, \tag{3.10}$$

$$\omega^2_{\mathrm{y,real}} \approx \eta_{\mathrm{NC,y}}\omega^2_{\mathrm{y,real}} + b_{\mathrm{NC,y}}, \tag{3.11}$$

$$\omega^2_{\mathrm{z,real}} \approx \eta_{\mathrm{NC,z}}\omega^2_{\mathrm{z,real}} + b_{\mathrm{NC,z}}. \tag{3.12}$$

All the data are shown in Fig. 3.7. From the data and the linear fitting, we can obtain $\eta_{\mathrm{C,y}} = 1.65$, $\eta_{\mathrm{C,z}} = 1.92$, $\eta_{\mathrm{NC,y}} = 1.23$, and $\eta_{\mathrm{NC,z}} = 1.11$. All these imperfection coefficients are larger than 1, which indicates that, relative to the ideal model, the DC electrodes are closer to the ion in the radial direction in reality. When we simulate the radial potential and check the principal axes rotation in the yz-plane, we use the average values $\eta_{\mathrm{C,yz}} = 1/2(\eta_{\mathrm{C,y}} + \eta_{\mathrm{C,z}}) = 1.785$ and $\eta_{\mathrm{NC,yz}} = 1/2(\eta_{\mathrm{NC,y}} + \eta_{\mathrm{NC,z}}) = 1.17$ as the coefficients multiplied to $\phi_{\mathrm{C}}(0, y, z)$ and $\phi_{\mathrm{NC}}(0, y, z)$.

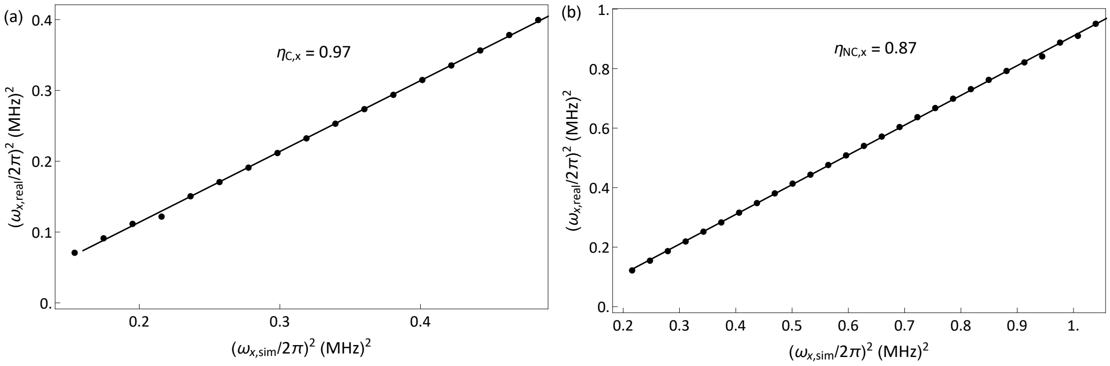

Figure 3.7 Axial potential calibration
(a) We only change the value of V_{NC} and measure $\omega_{\mathrm{real,x}}$. Then, we simulate the ideal $\omega_{\mathrm{sim,x}}$ using the same DC voltage condition. By linearly fitting the points $\omega^2_{\mathrm{x,real}}, \omega^2_{\mathrm{x,sim}}$, we obtain $\eta_{\mathrm{NC,x}} = 0.87$. (b) We only change the value of V_{C} and plot all the points $\omega^2_{\mathrm{x,real}}, \omega^2_{\mathrm{x,sim}}$. By linearly fitting the points, we obtain $\eta_{\mathrm{C,x}} = 0.97$.

3.3 The imaging system

3.3.1 Designing a high-NA objective lens

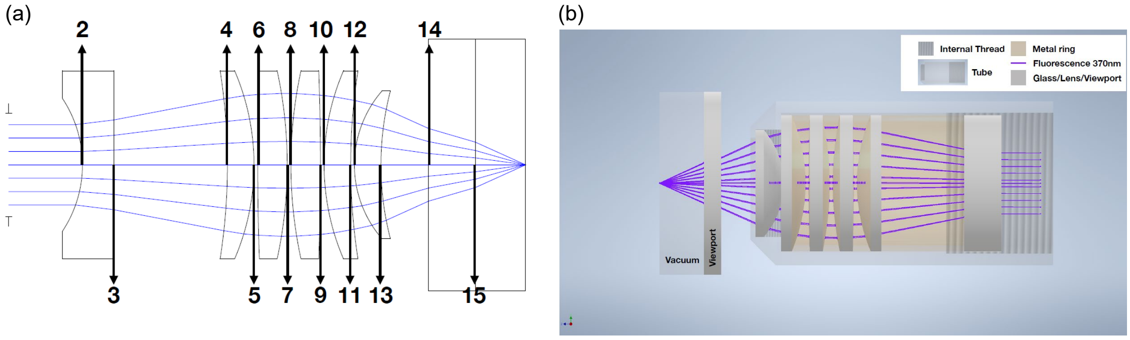

Figure 3.8 The structure of the custom-made lens.
(a) Surface SRF index. (b) 3D model.

To enhance detection fidelity, we designed a custom high-NA objective lens, the structure of which is depicted in Fig. 3.8. When designing a high-NA objective lens, the thickness of the viewport is a crucial parameter. Typically, a high-NA objective lens can only be used with the specific viewport for which it was designed. Utilizing the lens to image ions behind a viewport with a different thickness would significantly reduce the image quality. The quality of imaging could be reduced to the level of focusing quality. An ideal focus point requires all rays to have the same optical path length, but the presence of a viewport dramatically increases the optical path length difference between the center ray and the edge ray, especially for high-NA lenses. Therefore, it is imperative to carefully choose or design a high-NA objective lens for a viewport.

Our design is inspired by a design from the University of Maryland[48], and we modified the parameters to suit our experimental setup. The parameters we adjusted for optimization include the distance between Surface 3 and Surface 4, the distance between Surface 13 and Surface 15, the radii of Surfaces 2, 12, and 13, and the thickness of Surface 12. We used the point-spread function to evaluate the performance of the lens and employed Zemax to automatically optimize the parameters. To separate individual lenses with the specific distances generated by Zemax, we designed a set of spacers with the corresponding distances. These spacers ensure that the actual distances deviate minimally from the designed values, provided that individual lenses are attached to the spacers.

After finalizing the parameters, we collaborated with a domestic company, 福晶科技, to manufacture the individual lenses, and commissioned Taobao to produce the spacers. We then assembled the high-NA lens in-house.

3.3.2 The imaging setup

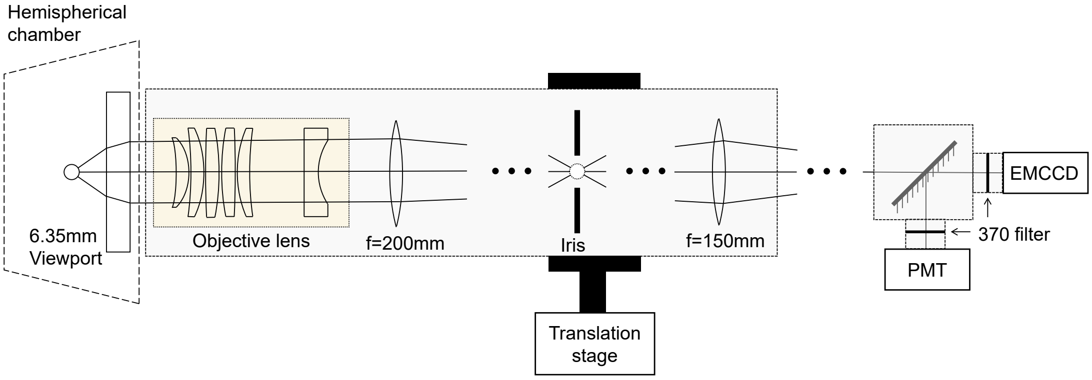

Figure 3.9 Imaging system for $^{171}\mathrm{Yb}^+$.

Fig. 3.9 shows the setup for imaging ions. The high-NA objective lens collects the fluorecense emitted by ions, and outputs a parallel beam. A lens of 200 mm focal length is used to focus the fluorecense on the plane of an iris, and the iris is used to block scattering of 370nm laser. After the iris, a lens of 150 mm focal length is used to image ions to the PMT or camera. At the begining, we use a 100 mm lens instead of 200 mm, and a 100 mm lens instead of 150 mm. But during experiment we find the detection fidelity using EMCCD is worse than PMT. Based on numerical simulation, we find the problem comes from the second lens, and the point spread function after the second lens is below 0.3. The beam size on the second lens is too large and induce aberrations that reduce the quality of the focus point. To improve the imaging quality, we change the focal length of the first lens from 100 mm to 200 mm, the focal length of the second lens from 100 mm to 150 mm. In this setup, the beam size on the second lens decreases, and a larger focal length also reduces the radius of the lens. Our simulations shows this modification could improve the point spread function to above 0.98.

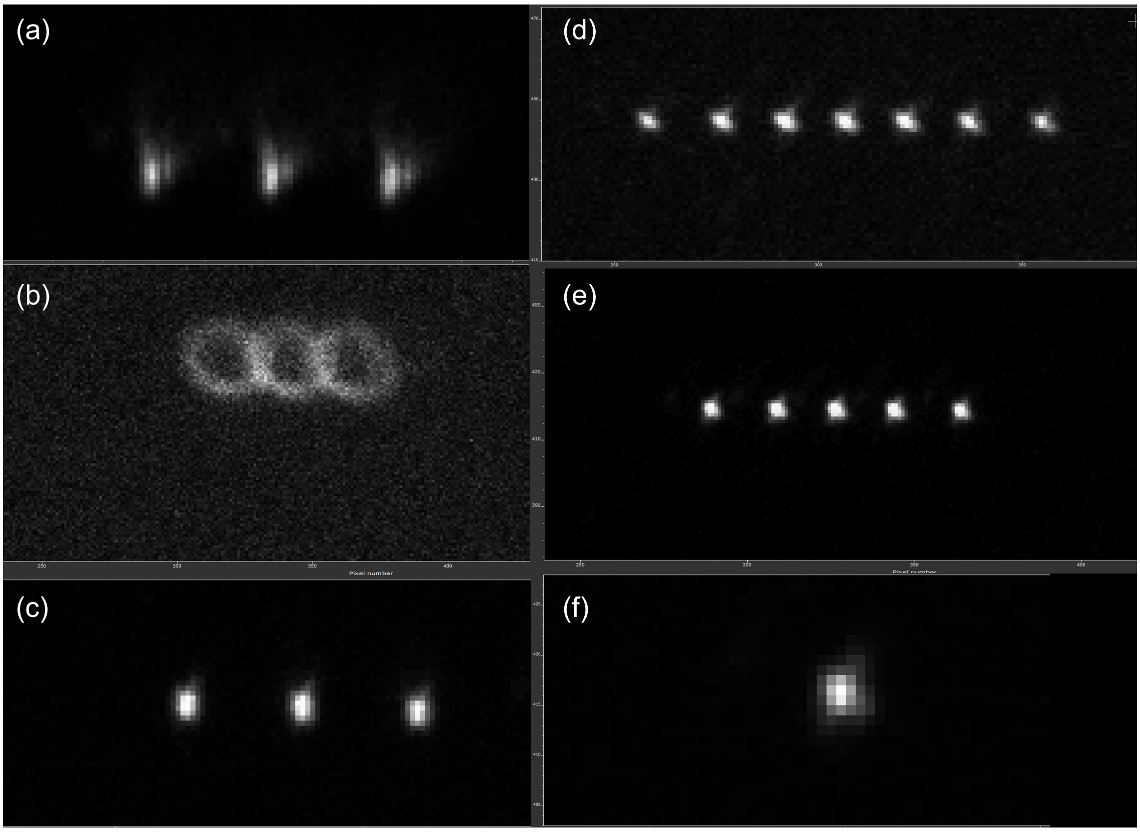

Figure 3.10 Adjust the aberration.

In an imaging system with a high-NA lens, the aberration is very sensitive to the relative position between the viewport and the objective lens. Fig. 3.10 shows how image quality changes with during the adjustment. Fig. 3.10(a) shows images of ions without any aberration compensation, and we can clearly observe comatic aberration which indicates the optical axis of the objective lens is mismatched with the optical axis of the viewport. Fig. 3.10(b) shows a defocusing image of ions, and ellipses also indicate comatic aberration. To eliminate the aberrations, we use a 5-axis translation stage to adjust the otical axis of the objective lens. After the aberration compensation, the quality of imaging improves a lot. Fig. 3.10(c,d,e,f) show images after aberration compenstion, and from (c) to (e) still needs a little bit of compensation.

3.4 Laser settings

3.4.1 Hollow-cathode lock

We lock the wavelength of the 369 nm laser to a hollow cathode using polarization spectroscopy. Polarization spectroscopy employs two counter-propagating beams to generate a Doppler-free signal: one for pumping and the other for probing. Compared with saturated absorption spectroscopy, polarization spectroscopy is more robust against amplitude fluctuations[49].

In polarization spectroscopy, a circularly polarized pumping beam is used to saturate the transition from $m = -1$ to $m = 0$, and to generate an unbalanced absorption rate for left-circularly-polarized and right-circularly-polarized lasers, a phenomenon called circular dichroism. The difference in absorption rates, $\Delta\alpha = \alpha^+ - \alpha^-$, can be converted to a difference in refractive indices according to the Kramers-Kronig dispersion relation:

$$n^+ - n^- = \frac{c}{\omega_0}\frac{\Delta\alpha_0 x}{1 + x^2} \tag{3.13}$$

Here, $x = (\omega_0 - \omega)/(\Gamma/2)$, ω_0 is the frequency of the atomic transition, ω is the frequency of the laser, and Γ is the spontaneous emission rate of the corresponding excited state. We then use a linearly polarized beam to probe the circular dichroism. Let the laser propagating direction be the z-axis, and the vertical axis be the x-axis. Assume the polarization of the probe beam has an angle of ϕ with respect to the x-axis. The electric field of the probe beam can be written as:

$$E_p = E_0 e^{i(\omega t - kz)}(\cos\phi\hat{x} + \sin\phi\hat{y}) \tag{3.14}$$

The left-circularly polarized component and the right-circularly polarized component are then $E^+ = \frac{1}{2}E_0 e^{i(\omega t-kz)}e^{-i\phi}(\hat{x}+i\hat{y})$ and $E^- = \frac{1}{2}E_0 e^{i(\omega t-kz)}e^{i\phi}(\hat{x}-i\hat{y})$, respectively. If the length of the circular dichroism region is L, the circular dichroism induces a phase difference on the circularly polarized components. The phases of the circularly polarized beams become $\phi^+ = -\frac{2\pi}{\lambda}n^+L - \phi$ and $\phi^- = -\frac{2\pi}{\lambda}n^-L + \phi$. Due to the unbalanced absorption, the amplitudes of the circularly polarized beams become $E^+ = E_0 e^{-\frac{\alpha^+}{2}L}$ and $E^- = E_0 e^{-\frac{\alpha^-}{2}L}$, where $\alpha/2$ is used for intensity decay with $e^{-\alpha L}$. The circularly polarized components can then be written as:

$$E^+ = \frac{1}{2}E_0 e^{-\frac{\alpha^+}{2}L} e^{i\omega t} e^{-i(\frac{2\pi}{\lambda}n^+L+\phi)}(\hat{x}+i\hat{y})$$

$$E^- = \frac{1}{2}E_0 e^{-\frac{\alpha^-}{2}L} e^{i\omega t} e^{-i(\frac{2\pi}{\lambda}n^-L-\phi)}(\hat{x}-i\hat{y})$$

After the circular dichroism region, if we project the light field into horizontal and vertical directions using a PBS, we obtain (note that $e^A+e^B = e^{(A+B)/2}(e^{(A-B)/2}+e^{-(A-B)/2})$):

$$E_x = \frac{1}{2}E_0 e^{i\omega t} e^{-\frac{\alpha L}{2}} e^{-i\frac{kL}{2}} \left(e^{-\frac{\Delta\alpha}{4}L} e^{-i(\frac{\Delta k}{2}L+\phi)} + e^{\frac{\Delta\alpha}{4}L} e^{i(\frac{\Delta k}{2}L+\phi)}\right)$$

$$E_y = \frac{i}{2}E_0 e^{i\omega t} e^{-\frac{\alpha L}{2}} e^{-i\frac{kL}{2}} \left(e^{-\frac{\Delta\alpha}{4}L} e^{-i(\frac{\Delta k}{2}L+\phi)} - e^{\frac{\Delta\alpha}{4}L} e^{i(\frac{\Delta k}{2}L+\phi)}\right)$$

Here, $\alpha = \frac{\alpha^+ + \alpha^-}{2}$, $k = \frac{k^+ + k^-}{2}$, $\Delta\alpha = \alpha^+ - \alpha^-$, and $\Delta k = k^+ - k^- = \frac{2\pi}{\lambda}(n^+ - n^-) = \frac{2\pi c}{\lambda\omega_0}\frac{\Delta\alpha x}{1+x^2}$. If we probe the power difference of these two components using a balanced PD, we get:

$$I_b = |E_x|^2 - |E_y|^2 = E_0^2 e^{-\alpha L}\cos(\Delta k L + 2\phi)$$

Let $\phi = \frac{\pi}{4}$; the formula above can be simplified to:

$$I_b \approx I_0 e^{-\alpha L}\sin(\Delta k L) \approx I_0 e^{-\alpha L}\Delta\alpha L\frac{x}{1+x^2}$$

Fig. 3.11 shows the optical path used for polarization spectroscopy. The output power of the laser head is approximately 8.3 mW, and 0.7 mW is used for the hollow-cathode lock. Initially, we put all of the power into the lock part to observe the hole burning signal. In daily use, we can only see the error signal after a lock-in amplifier and cannot directly observe the hole burning.

Fig.3.12 displays the hole burning signal directly observed in the absorption spec-

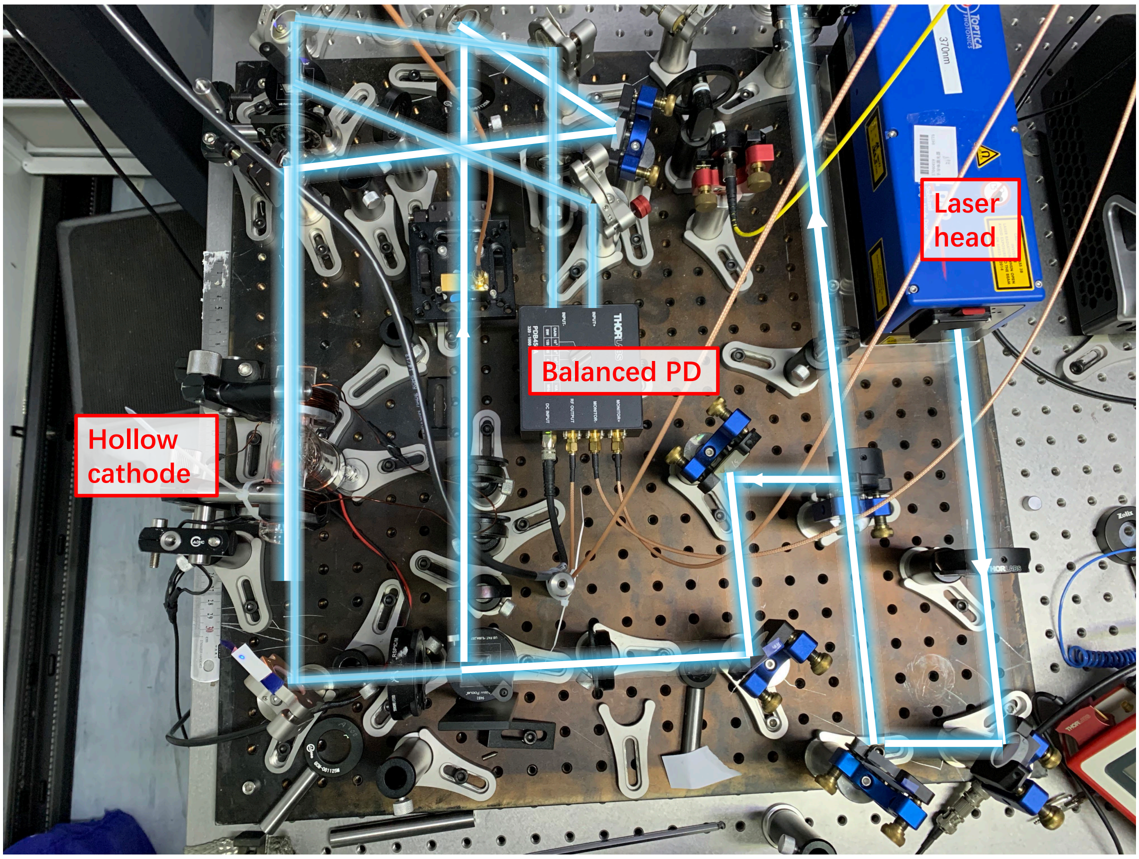

Figure 3.11 Optical path for 370 lock

troscopy. To measure the absorption spectroscopy, we scan the laser frequency by changing the piezo voltage with a triangular waveform. We separately measure outputs of the balanced PD, where one output is proportional to the power of the horizontally polarized component, while the other is proportional to the power of the vertically polarized component. We adjust a quarter-wave plate applied to the pumping beam to maximize the difference between the outputs of the balanced PD. Fig.3.12 (a,c) show the spectroscopy without a pumping beam, and the deep signal represents the Doppler absorption of the ions in the hollow cathode. Fig.3.12(d) displays the hole burning generated by a circularly polarized pump beam, where the absorption from ions is suppressed. Fig.3.12(b) exhibits the spectrum of the other polarization, and the result shows the absorption on the other polarization is enhanced.

3.4.2 Phase Locked Loop Implementation

Given the constant fluctuations in the repetition rate of the pulsed laser, we implement a phase locked loop (PLL) to track these changes in the repetition rate. This feedback mechanism helps stabilize the Raman transition. Fig. 3.14 depicts the electronic circuitry

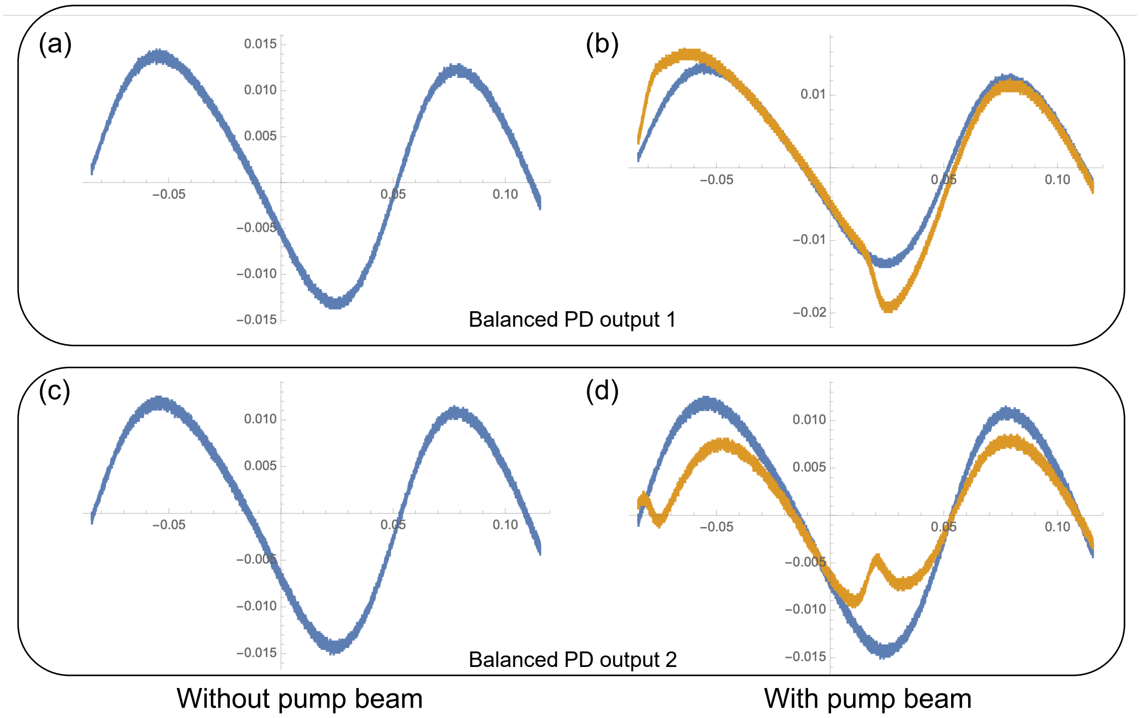

Figure 3.12 Cicurlar dichroism signal of $^{171}\mathrm{Yb}^{+}$.
(a,c) The absorption spectroscopy of a Ytterbium hollow cathode without an extra pumping beam. (b,d) The absorption spectroscopy with an extra pumping beam, and the hole burning signal. The orange curves represent the signal with pumping, and the blue curves are the same as (a,c), and are used to guide the eye. (a,b) are collected from port 1 of the balanced PD. (c,d) are collected from port 2 of the balanced PD. The horizontal axis represents time, and the vertical axis represents voltage.

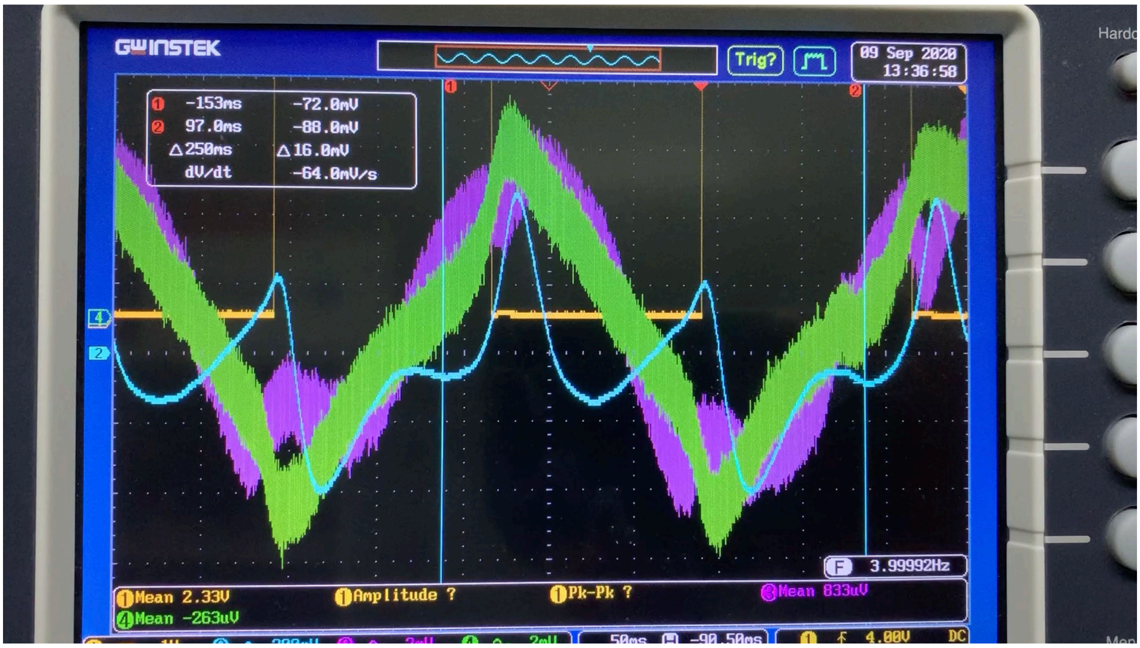

Figure 3.13 The error signal.
The blue curve is the error signal after a lock-in amplifier. The green and purple curves are the outputs of the balanced PD.

associated with the phase locked loop.

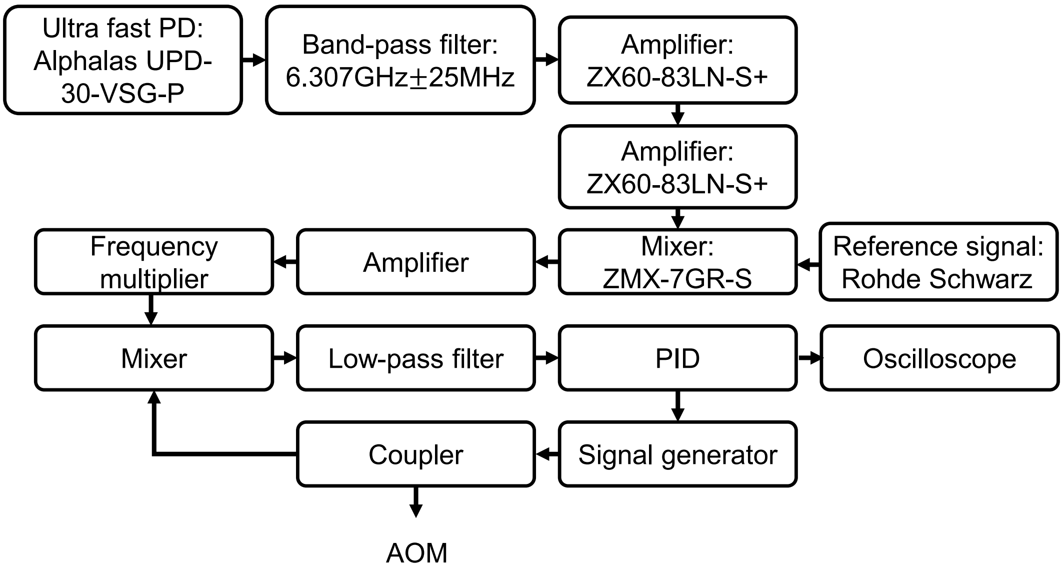

Figure 3.14 Schematic of the phase locked loop circuit.

3.5 Observed Imperfections

3.5.1 Rapid Decay of Rabi Oscillation

Upon reviving the system, we encountered an unexpected issue where the Rabi oscillations decayed at an accelerated rate. This phenomenon was so severe that almost no oscillation could be observed, as demonstrated in Fig.3.15(a). Initially, we speculated that the problem might be due to some leakage from the carrier transition to nearby undesired transitions, with the Rabi frequency being too high to encompass them. In order to validate this hypothesis, we reduced the power and conducted a new Rabi oscillation scan. The results were in line with our assumption. As seen in Fig.3.15(b,c,d,e,f), as the Rabi frequency decreases, the decay weakens. When we set a Rabi frequency with a π-time of 160 µs, the first two oscillations exhibit virtually no decay, as demonstrated in Fig. 3.15(f).

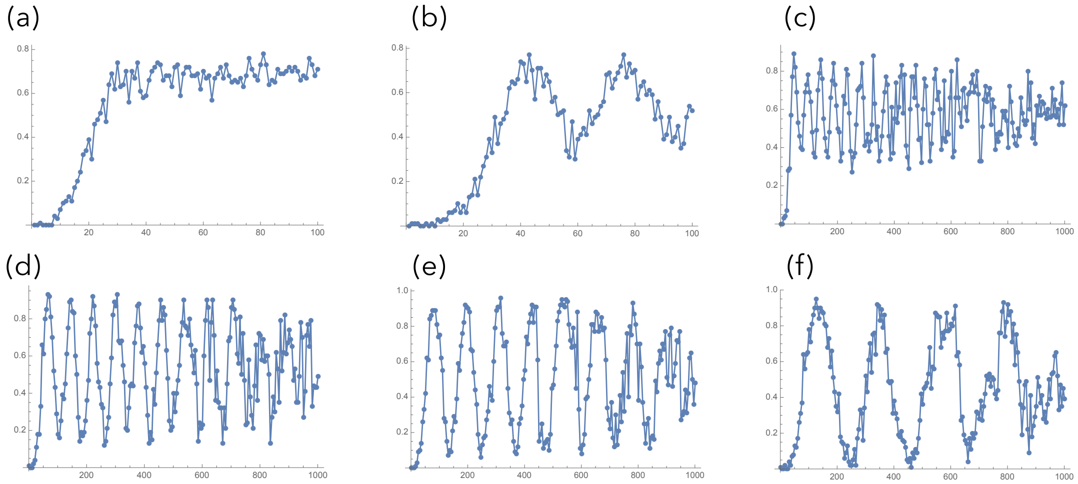

Figure 3.15 Issue: Rapid Decay of Rabi Oscillations
The Rabi oscillations decay unusually rapidly, with the decay speed correlating with the value of Rabi frequencies. The higher the frequency, the faster the decay. Figures a,b,c,d,e,f illustrate the decay of Rabi oscillation at various Rabi frequencies.

However, upon performing a meticulous scan around the carrier transition, we failed to identify any aberrant transitions. No such transitions were found near the carrier transition. Consequently, we hypothesized that the decay may not originate from the ion, but rather from the operation itself. We separated the Rabi oscillation from pumping and detection by introducing a waiting time before and after the Rabi oscillation, and discovered that if a waiting time is inserted between the optical pumping and the Rabi oscillation, the decay is significantly reduced, as demonstrated in Fig. 3.16(a,b,c,d).

This observation strongly suggests that the optical pumping process is not cleanly

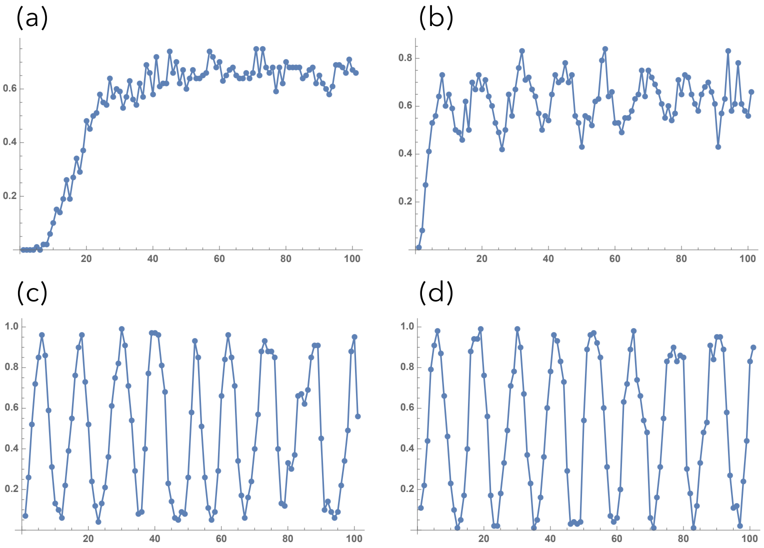

Figure 3.16 Insight: Introducing a Waiting Time between Rabi Oscillation and Pumping Proves Beneficial

Maintaining the same Rabi frequency, an increase in the waiting time between pumping and the Rabi oscillation results in a slower decay of the resulting oscillation. (a) introduces a waiting time of 2 µs. (b) introduces a waiting time of 20 µs. (c) introduces a waiting time of 40 µs. (d) introduces a waiting time of 50 µs.

terminated, resulting in leakage of some optical pumping beams into the Rabi oscillation. To substantiate this hypothesis, we employed a fast photodetector (PD) to monitor the temporal evolution of the optical pumping beam, revealing a long tail, as illustrated in Fig.3.17(a). To confirm this issue, we replaced the original Acousto-Optic Modulator (AOM) with a different one, which exhibits no such long tail in its temporal behavior. Following this modification, we observed a much clearer Rabi oscillation, as illustrated in Fig.3.17(b).

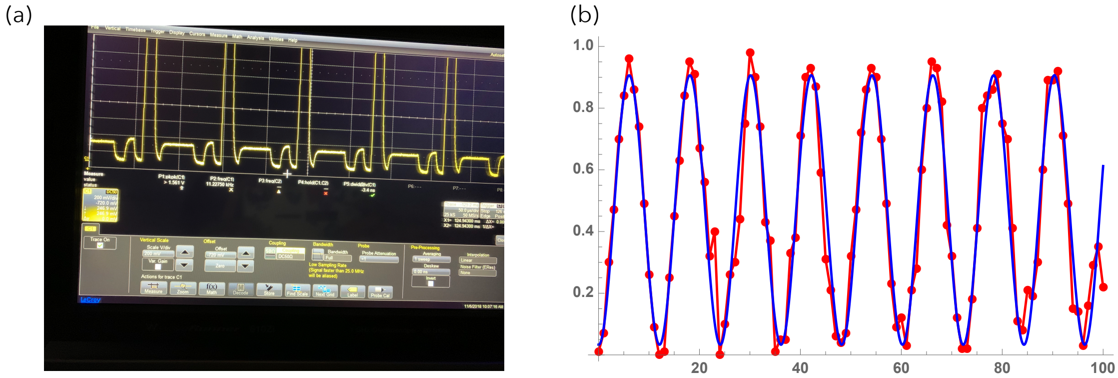

Figure 3.17 Resolution: AOM Replacement

(a) The persistent tail of the optical pumping beam. (b) Following the replacement of the AOM, the Rabi oscillation is significantly clearer.

3.5.2 Issues Encountered in Repetition Rate Lock

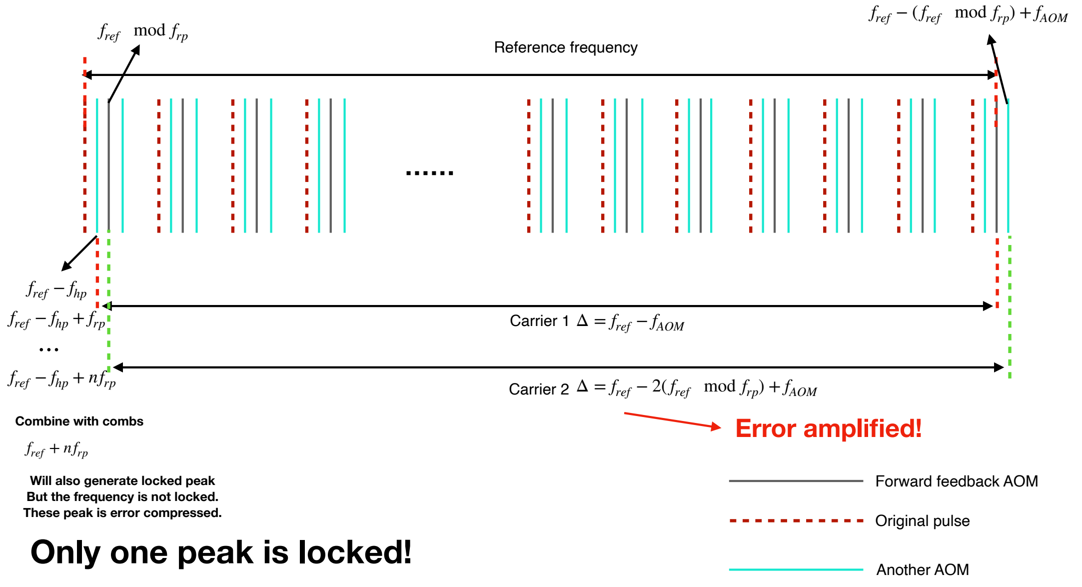

Figure 3.18 Erroneous Repetition Lock
The red dashed lines represent the frequency comb generated directly by the pulsed laser. The black lines represent the frequency combs following the feedforward Acousto-Optic Modulator (AOM), which have an overall additional frequency shift representing repetition rate fluctuation. The blue lines represent the frequency combs following another AOM.

Upon first locking the 355 nm pulsed laser, we observed no improvement in coherence time. We soon discovered that we had not locked directly onto the hyperfine splitting frequency of 12.6 GHz, but rather locked the frequency comb to 6.3 GHz due to the bandwidth limitation of the photodetector (PD). Given that the repetition rate of our pulsed laser is 120.139 93 MHz, the 105th frequency comb is closest to the hyperfine splitting. This situation is problematic, as there is no 52.5th frequency comb. We can only lock onto the 52nd or 53rd frequency comb, and then add or subtract an additional 120.139 93 MHz after frequency doubling.

For instance, if we sample the frequency fluctuation of the 52nd frequency comb, which is $52\delta f_r$, after doubling the fluctuation, the output of the phase-locked loop (PLL) could compensate a fluctuation of $104\delta f_r$. We cannot directly utilize the 105th comb, as we only compensate the accumulated noise of 104 combs. The frequency difference between the 105th comb and the hyperfine splitting is 28 MHz, while the difference between the 104th comb and the hyperfine splitting is 148 MHz, necessitating that the AOMs used for the Raman transition also have a frequency difference of 148 MHz. In the alternative scenario, we can lock onto the 106th comb, and the frequency difference would be

92 MHz, which is more manageable when selecting an AOM.

Therefore, if we blindly lock the PLL to half of the hyperfine splitting and use the calculated frequency difference between the 105th comb and the hyperfine splitting, the Raman transition is effectively unlocked. The key to understanding this phenomenon is to recognize that there is only one comb stabilized in the feedforward method, and any transitions driven by unlocked combs will exhibit significant decoherence. For example, if we lock the 105th comb, the transition driven by the 105th comb of the locked beam and the 0th comb of the unlocked beam is stabilized, but the transition driven by the 0th comb of the locked beam and the 105th comb of the unlocked beam will have a frequency fluctuation twice as large.

3.5.3 Unanticipated Raman Transitions

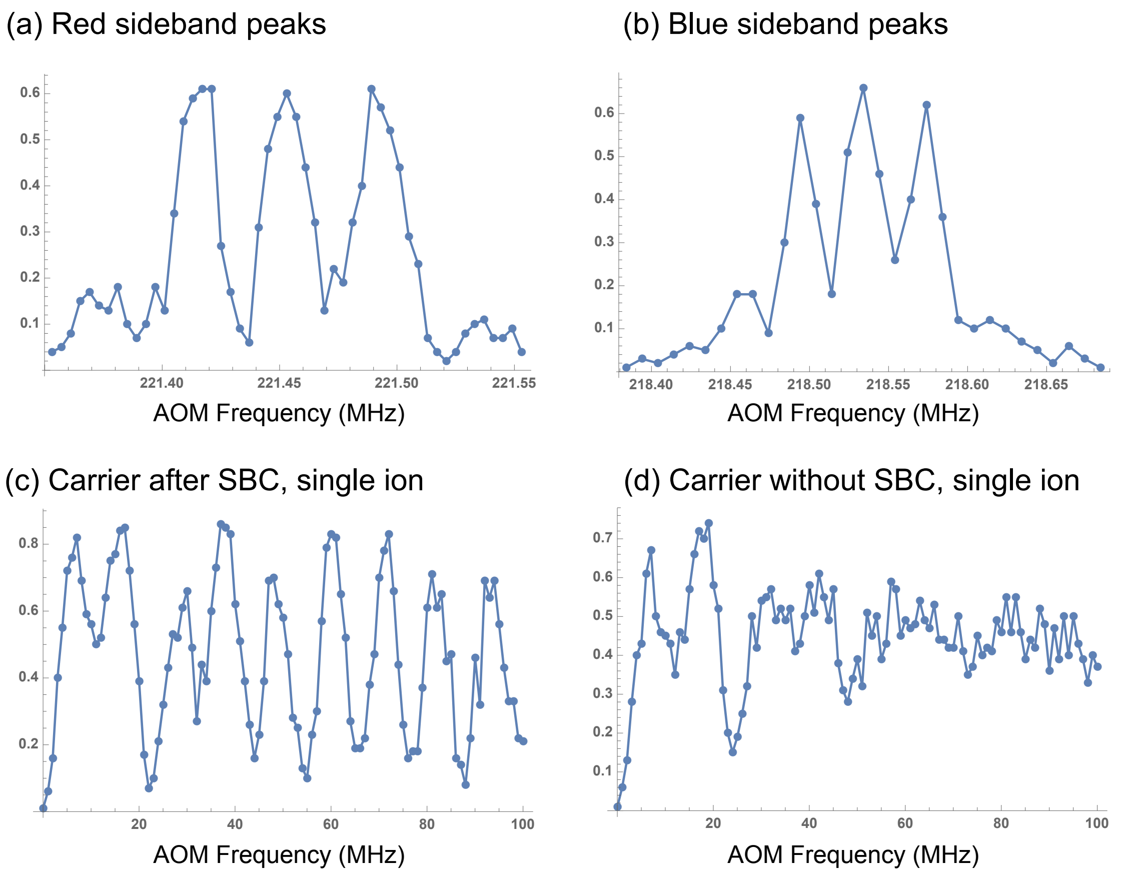

Figure 3.19 An Unexpected Raman Peak
(a) The red-sideband peak. (b) The blue-sideband peak. (c) Carrier Rabi oscillation following sideband cooling. (d) Carrier Rabi oscillation prior to sideband cooling.

One day, our Raman signal unexpectedly deviated from the norm. As illustrated in Fig.3.19(a,b), the red-sideband and blue-sideband peaks significantly deviated from the ideal profile. Initially, we hypothesized that these unusual peaks occurred because the duration we set exceeded the π-time. However, upon attempting to scan the Rabi oscillation to determine the correct π-time, we found that the Rabi oscillation of the carrier transition also behaved oddly, as shown in Fig.3.19(c,d).

After considerable troubleshooting, we traced the problem back to the PLL. We discovered that the gain of the Proportional–Integral–Derivative (PID) controller was set too high, causing the error signal to oscillate slightly. Upon reducing the PID gain, the sideband peaks became clear, as shown in Fig. 3.20.

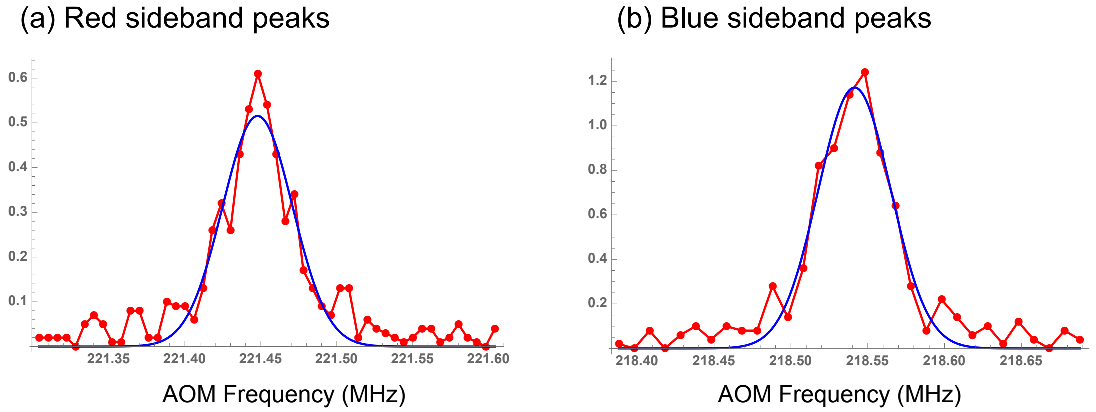

Figure 3.20 Raman Peaks
(a) The red-sideband peak. (b) The blue-sideband peak.

Nonetheless, we continued to observe these strange peaks on multiple occasions. Each time, the issue originated from the repetition rate lock, which either jumped or became unstable.

3.5.4 Electrical Breakdown of the Trap

One day, after repeatedly and rapidly toggling the power of the RF signal between high and low levels, we noticed that the ion suddenly vanished, and the reflection signal from the helical resonator intensified. We also observed that the vacuum record (as indicated by the ion number) jumped from 0 nA to over 60 nA. We inferred that a significant event had occurred. First, we activated the conditioning mode of the Non-Evaporable Getter (NEG) pump and waited several hours to reduce the chamber pressure. While waiting, we attempted to minimize the reflection signal from the helical resonator, but noticed that the resonant frequency had shifted by approximately 500 kHz. After reloading the ions, we found that the trap had become very unstable. We attempted to minimize the micromotion once again, but as we suspected that a sharp power change might have triggered a significant event, we added a low-pass filter to the output of the power switch. When we switched from high to low power, the ions moved upwards, indicating micromotion. Surprisingly, when we switched back from low to high power, the ions did not return to their original position along the same path but instead followed a different, longer path. We speculated that this unusual behavior could have originated from a strange capacitance induced by the electrical breakdown.

Since the trap was no longer functional, we opened the vacuum and checked the connection between electrodes, finding that a spark had indeed occurred between the electrodes, completely disrupting the surrounding structure. To understand how the spark had formed, we examined other unused traps that were produced concurrently with the broken trap. Fig. 3.21 shows the Scanning Electron Microscope (SEM) image of unused traps. It is clear that at certain positions on the trap, the distance between the coating layer of electrodes is too short.

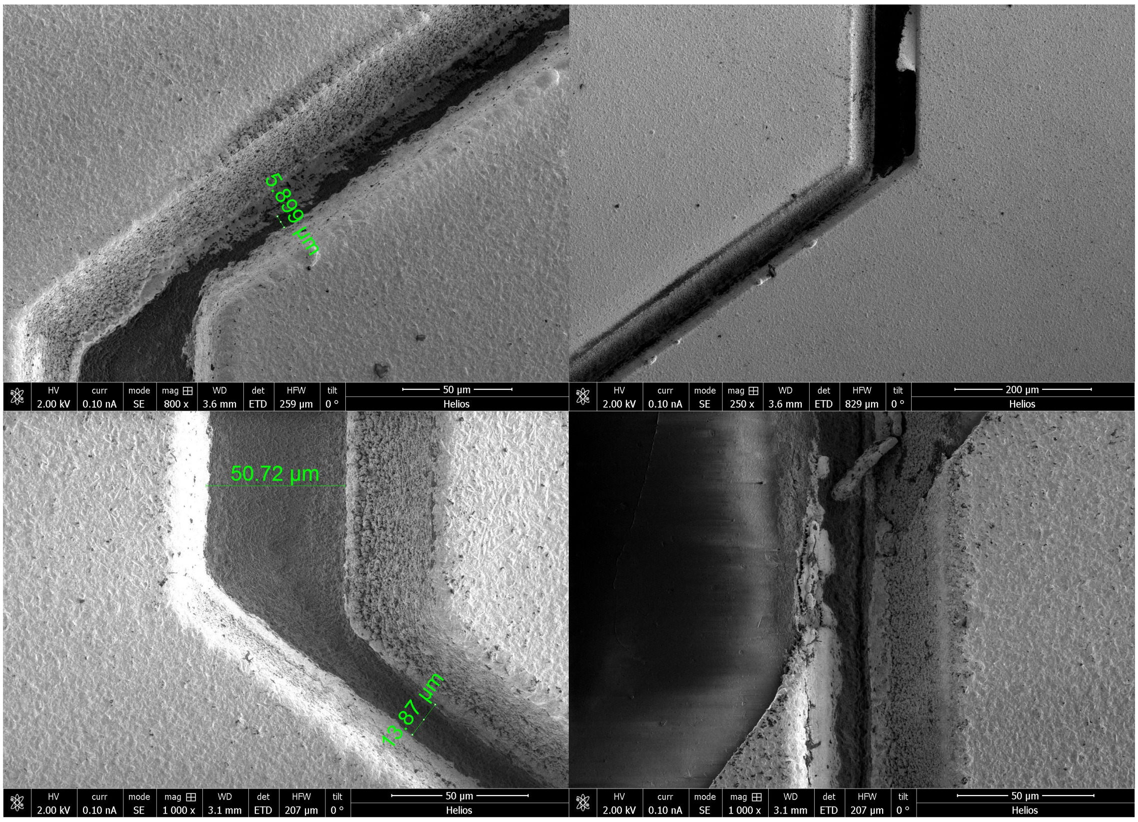

Figure 3.21 Potential sites for electrical breakdown.

To address this issue, we sent the unused traps back to the manufacturer for modification. They used a laser to increase the insulating gap between electrodes. With the improved trap, we have not experienced any further sparks.

CHAPTER 4 PREPARATION OF 2D CRYSTALS

4.1 Rotation of principle axes

We demonstrate the capability of rotating the principle axes of the trap potential to ensure the micromotions to be on the 2D plane, which will be perpendicular to the net k-vector of Raman laser beams. We rotate the principle axes in the y-z plane by adjusting voltages V_{C} and V_{NC} on both of the center electrodes DC_{C} (DC1, DC2 in Fig. 3.4(b)) and all of the next to the center electrodes $\mathrm{DC}_{\mathrm{NC}}$ (DC3, DC4, DC5, and DC6 in Fig. 3.4(b)), respectively.

The total pseudo-potential with voltages of V_{C}, V_{NC} and V_{RF} is described by

$$\phi(x, y, z) = V_{\mathrm{C}}\phi_{\mathrm{C}} + V_{\mathrm{NC}}\phi_{\mathrm{NC}} + V_{\mathrm{RF}}\phi_{\mathrm{RF}}, \tag{4.1}$$

where ϕ_{C} and ϕ_{NC} are electric potentials at the position of (x, y, z) generated by DC_{C} and $\mathrm{DC}_{\mathrm{NC}}$ electrodes with unit voltage. And ϕ_{RF} is the pseudo-potential generated by the RF electrode with root-mean-square voltage of 1 V. In y-z plane, the symmetric RF pseudo-potential can be broken by DC potentials, which leads to a elliptical total potential $\phi(x, y, z)|_{x=0}$. The two axes of the elliptical potential are the principle axes. In order to rotate the principle axes to y axis and z axis, we need to satisfy

$$\partial\phi(0, y, \delta z)/\partial y|_{y=0} = 0, \tag{4.2}$$

where δz is the radius of a 2D crystal and small enough to be in harmonic regime for our consideration. In our numerical calculation, we use 30 μm for δz. Noticing $\partial\phi_{\mathrm{RF}}(0, y, \delta z)/\partial y|_{y=0} = 0$ is always true, we can calculate the solution of $V_{\mathrm{NC}}/V_{\mathrm{C}}$, to satisfy Eq. (4.2) based on numerical simulation. In our trap, $V_{\mathrm{NC}}/V_{\mathrm{C}} \approx 5.11$. We should also notice that whenever we set $V_{\mathrm{NC}}/V_{\mathrm{C}}$ to the right value and rotate the principle axes to y axis and z axis, V_{RF} will no longer affect the rotation of the principle axes. Here, we do not consider the rotation of the principal axes along the x-direction in the small area near the trap center due to the transnational symmetry. Indeed, our numerical simulation also shows a negligible rotation of the principal axes up to $\delta x = 50$ μm, which would introduce a micromotion disturbance similar to the level of intrinsic micromotion.

We numerically calculate ϕ_{C}, ϕ_{NC} and ϕ_{RF} with CPO software. We set the RF signal to be $\omega = 2\pi \times 40$ MHz and $V_{\mathrm{RF}} = 80$ V. When $V_{\mathrm{NC}}/V_{\mathrm{C}} = \infty$ with $V_{\mathrm{NC}} = 1.5$ V, vertical principle axis (green line in Fig. 4.1(a)) is clockwise rotated by 22.9° from the z-axis.

When the ratio $V_{\mathrm{NC}}/V_{\mathrm{C}} = 0$ with $V_{\mathrm{C}} = 1.5$ V, the green axis is counter-clockwise rotated by 5.7° from the z-axis. As shown in Fig. 4.1(b), when the ratio $V_{\mathrm{NC}}/V_{\mathrm{C}} = 5.11$, the green axis is in line with z-axis.

We experimentally confirm the rotation of the principle axes in y-z plane with single ion by observing the disappearance of the Raman coupling to z-axis vibrational mode. The spectrum of vibrational modes, as shown in Fig. 4.1(c)(d) is measured by the following procedure: 1) we perform Doppler cooling on ion-crystal, which results in thermal states with $\bar{n} \approx 7.1$ for mode frequency $\omega_y \approx 2$ MHz, and initialize the internal states to $|\downarrow\rangle$ by applying the standard optical pumping technique. 2) We apply Raman beams with a net k-vector perpendicular to the z-x plane. Once the beatnote-frequency ω_{R} of Raman beams matching to $\omega_0 \pm \omega_{\mathrm{y,z}}$, sideband transitions occurs[37], which can be detected by the fluorescence of ions that is collected by imaging system and PMT (Photo-multiplier tube). In Fig. 4.1(c), the voltage ratio is close to the condition of $V_{\mathrm{NC}}/V_{\mathrm{C}} = \infty$ in Fig. 4.1(a), where the principle axes are tilted away from y-z axes. The net k-vector of Raman beams is along the y-axis, which can excite both directions of vibrational modes. Thus, two peaks in blue-sidebands $\left(\delta = \omega_{\mathrm{y,z}}\right)$ as well as red-sidebands $\left(\delta = -\omega_{\mathrm{y,z}}\right)$ are clearly visible in Fig. 4.1(c), where detuning $\delta = \omega_{\mathrm{R}} - \omega_0$. However, when the principle axes are rotated to y-z axes as shown in Fig. 4.1(b), Raman beams cannot excite the vibrational mode along z-axis, which results in vanishing a peak in the Raman spectrum. Based on the spectrum of Fig. 4.1(d), we estimate that deviation of the principle axes from y-z axes is below 0.40°.

4.2 Loading and imaging of 2D-ion-crystals

In order to produce a 2D ion-crystal in z-x plane, we need to satisfy $\omega_{\mathrm{y}} > (2.264N)^{1/4}\omega_{\mathrm{x,z}}$ (when $\omega_{\mathrm{x}} = \omega_{\mathrm{z}}$)[50-51]. In general, we need four control parameters to rotate the principal axes and set three trap-frequencies independently. In the experiment, we find that three control voltages, $V_{\mathrm{C}}, V_{\mathrm{NC}}$, and V_{RF} in Eq. (1), are enough to produce various geometries of the 2D crystals, which is only determined by the ratio of ω_x and ω_z when ω_y is large enough to be 2D crystals. First, keeping the principle axes to y-z axes, we can calculate the voltage solution for DC electrodes with a given axial trap frequency ω_{x}, which is mostly determined by V_{NC}. With determined DC potential, the relation between ω_{y} and ω_{z} is given by[37]

$$\omega_{\mathrm{y}}^2 - \omega_{\mathrm{z}}^2 = C V_{\mathrm{NC}}, \tag{4.3}$$

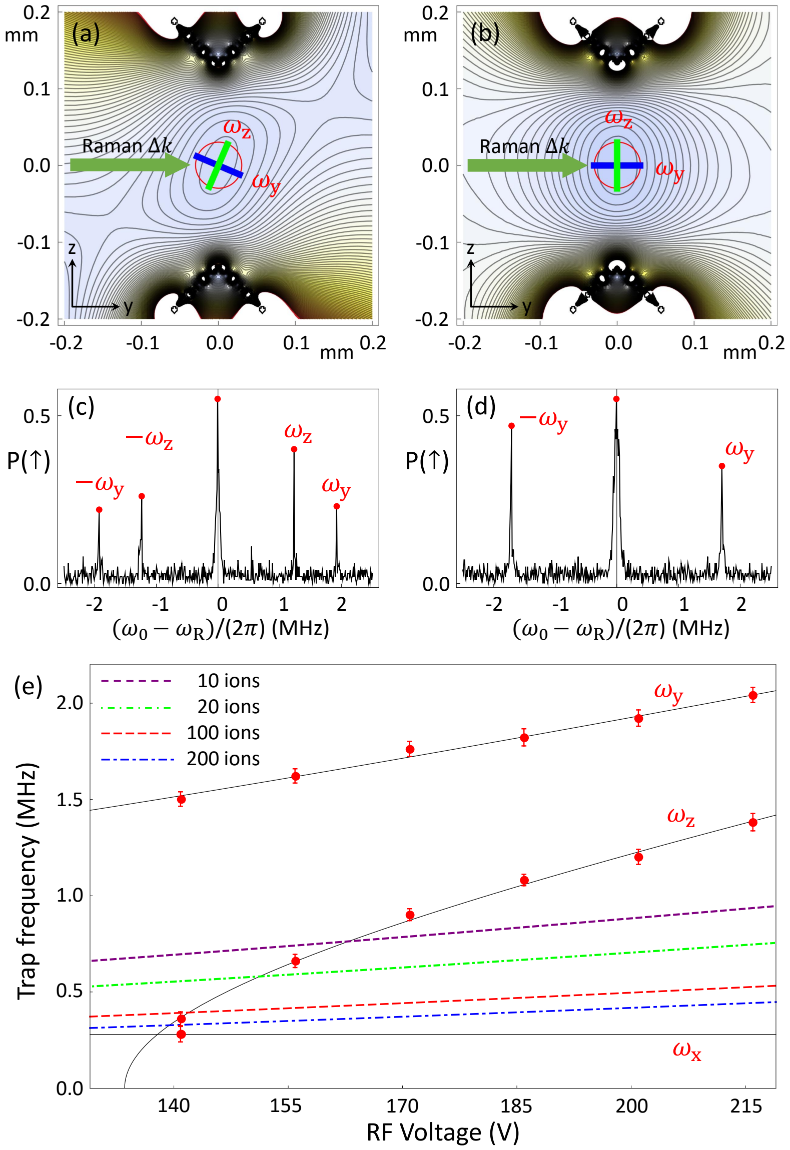

Figure 4.1 Principle axis rotation

(**a**) The contour plot of pseudo-potential when $V_{\mathrm{NC}}/V_{\mathrm{C}} = \infty$, central electrodes are connected to GND. (**b**) The contour plot of pseudo-potential when the principle axes are overlapped with y and z axes, where the voltage ratio is $V_{\mathrm{NC}}/V_{\mathrm{C}} = 5.11$. (**c**) The Raman spectrum with principle axes in the condition of (a), where we can see both of the transverse modes. (**d**) The Raman spectrum with principle axes in the condition of (b). In this situation, the Raman beams can only drive the mode of the y-axis, not that of the z-axis. (**e**) Relation between two radial-mode frequencies and the RF voltages. By merely changing the RF voltage, we can realize different ratios of trap frequencies. The red dots are the experimental data, the dark lines are the fitting results. The dashed lines, which are calculated by $\omega_y/(2.264N)^{1/4}$ for different RF voltage, are the up bounds of the region where the symmetric 2D crystal can be formed for different numbers of ions.

(see Appendix D) where C is a positive constant determined by the trap geometry. In the case of $V_{\mathrm{RF}} = 0$, the z-axis potential, the shallower potential respective to that of the y-axis according to Eq. (4.3), becomes anti-harmonic, which indicates $\omega_{\mathrm{z}}^2 < 0$ and $\omega_{\mathrm{y}}^2 < CV_{\mathrm{NC}}$. On the other hand, since $\omega_{\mathrm{y}} and\ \omega_{\mathrm{z}}$ are monotonously increase with V_{RF}, there is a critical value of V_{RF} that makes $\omega_{\mathrm{y}}^2 = CV_{\mathrm{NC}}$ and $\omega_{\mathrm{z}}^2 = 0$. Therefore, we can tune ω_{y} from $\sqrt{CV_{\mathrm{NC}}}$ to ∞, ω_{z} from near zero to ∞ by tuning V_{RF}. As shown in Fig. 4.1(e), with different values of V_{RF}, we can have $\omega_{\mathrm{z}}/\omega_x$ from 0 to 2.72 for 10 ions to realize 2D ion-crystal with different aspect ratios.

Once the requirements of principle axes and trap-frequencies for 2D crystal are satisfied as discussed above, we can confine ions in the z-x plane. Fortunately, the strongest trap frequency in our monolithic trap is in y-axis due to the geometry of the trap, which allows us to easily image the 2D crystal with the same imaging system to 1D chain. The fluorescence of ions in 2D crystal can be directly imaged through an objective lens to CCD camera as shown in Fig. 3.4(a). Fig. 5.4(a) are the images of the 2D crystals and demonstrate the control capability for shapes of 2D crystals with various settings of trap frequencies. For the image of 10 ions, the trap frequencies are $\{\omega_{\mathrm{x}}, \omega_{\mathrm{y}}, \omega_{\mathrm{z}}\}/(2\pi) = \{0.427, 1.50, 0.561\}$MHz. For the image of 19 ions and 25 ions the trap frequencies are $\{\omega_{\mathrm{x}}, \omega_{\mathrm{y}}, \omega_{\mathrm{z}}\}/(2\pi) = \{0.28, 1.50, 0.26\}$MHz and $\{\omega_{\mathrm{x}}, \omega_{\mathrm{y}}, \omega_{\mathrm{z}}\}/(2\pi) = \{0.28, 1.63, 0.68\}$MHz respectively. For 25 ions, the dashed line in Fig. 4.1(e) is the upper bound of the ω_{x} and ω_{z} where the symmetric 2D crystal can be formed. However, for forming an asymmetry 2D crystal in Fig. 5.4(a), the criteria are complicated and have been discussed in[52-53]. We numerically study the situation in Appendix E. We can imagine an oblate ellipsoidal 3D crystal ($\omega_{\mathrm{y}} > \omega_{\mathrm{z}} = \omega_{\mathrm{x}}$) whose in-plane trap frequencies are above the bound, then if we reduce ω_{x}, the crystal will tend to 2D and finally results in a linear chain. The geometries of the crystal are in agreement with the numerical simulation. We simulate the geometry configuration of the ion-crystal by numerically minimizing the electrical potential of the ions in a three dimensional harmonic trap[50].

4.3 Raman Spectrum of Transverse Vibrational Modes in 2D Crystals

Upon loading 2D ionic crystals, we manipulate various transverse modes of a 10-ion-crystal by modulating the detuning between Raman beams, a procedure akin to the

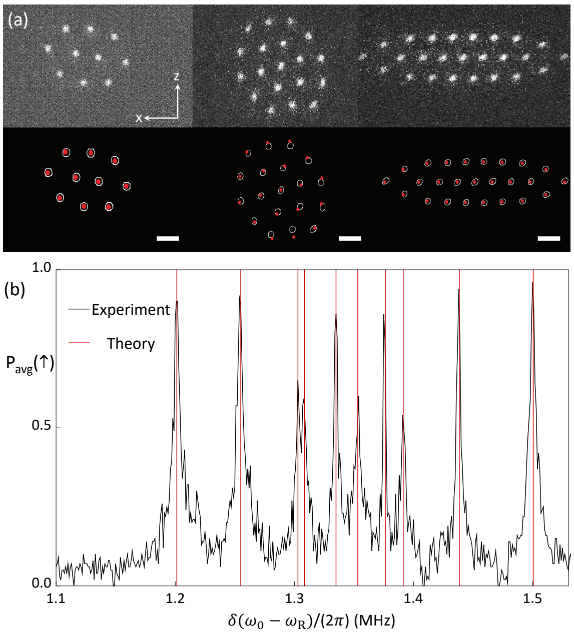

Figure 4.2 Geometry and mode structure of 2D-ion-crystals.
(**a**) CCD images of 10,19, and 25 ion-crystals with different trap frequencies. The above ones are raw data taken from EMCCD, and the bottom ones compare the numerical simulation and the real data where the white cycles are the positions of ions read out from the CCD pictures and the red points are simulation results. The white scale bars represent 5 μm distance. (**b**) Raman spectrum of the 2D crystal with ten ions. The crystal is first cooled by 1000 μs Doppler cooling, then a 3 μs optical pumping is performed to prepare the ground-state of qubits. The vibrational modes are excited by a 400 μs Raman sequence with 5 kHz Rabi frequency. The spectrum is obtained by collecting the fluorescence with PMT, and each data point is measured 100 times. The black curve is the experiment result and the red lines are the theoretical prediction of the mode frequencies[50].

single ion scenario. Fig. 5.4(b) displays the resultant spectrum, with each peak denoting a motional mode along the y-axis. To conduct the measurement, we initially cool the crystals to their vibrational ground-state using Doppler and EIT cooling, subsequently applying the Raman beams to drive the motional sidebands. The measured mode spectrum aligns with the theoretical simulation predicated on trap frequencies and the 2D ion-crystal's geometry[50]. The trap frequencies utilized for the simulation are $\{\omega_x, \omega_y, \omega_z\}/(2\pi) = \{0.427, 1.5, 0.561\}$MHz. We perform direct measurements of the trap frequencies along the y and x axes, employing the trap frequency along the z-axis as a fitting parameter. The congruence between experimental data and the pseudo-potential simulation indicates a negligible micromotion induced shift in our system. Further, we numerically simulate each ion's micromotion amplitude[54], estimating a maximum micromotion-induced frequency shift of 930 Hz[50]. Drawing parallels with the linear chain case[55-59], when a phase transition from a 2D crystal to a 3D crystal transpires, the minimal frequency of the modes along the y-axis will incline towards negativity. The frequencies we measured are significantly distinct from zero, which affirms the existence of 2D ionic crystals.

4.4 Compensation and Quantification of Micromotion in 2D Crystals

Ideally, the crystal, situated in the z-x plane, exhibits micromotion along the z-axis and perpendicular to the y-axis, aligned with the net propagation direction of Raman beams. In reality, two potential sources of imperfection could cause deviation from the ideal micromotion condition: 1) Stray electric fields, resulting in displacement; 2) Imperfections in electrode fabrication, inducing a tilt around the z-axis. To mitigate micromotion from these sources, we initially offset the stray field using a single-ion, and subsequently ameliorate tilt errors by gently rotating the crystal. With the single ion, we accomplish micromotion compensation by aligning the ion's position with the null point of the RF electric field[60-61]. Initially, we offset the extra-field in the z-direction by modulating the voltage of $\{\mathrm{DC2}, \mathrm{DC3}, \mathrm{DC4}\}$ or {DC1,DC5,DC6} concurrently with the ratio {1,5.11,5.11}, an approach that preserves the principle axes direction while precluding the generation of displacement along the y-axis. We can also modify the voltage of electrodes {DC1,DC3,DC4} or {DC2,DC5,DC6} with a ratio of {1,5.11,5.11} to offset the extra-field in the y direction. For z-axis compensation, we minimize the change in ion position based on RF power, whereas for y-axis compensation, we aim to reduce the micromotion sideband transition of Raman beams. To address the error induced by fabrication imperfections, we minutely adjust the voltage of electrodes {DC3,DC4,DC5,DC6} with a ratio of {1,1,1,1} to rotate the crystal around the x-axis and a ratio of {1,-1,1,-1} for rotation around the z-axis. Concurrently, we strive to minimize the Rabi-frequency of the micromotion sideband transition with three ions.

We quantify the micromotion strength by gauging the ratio between two Rabi frequencies of the carrier and the micromotion transition[60]. We perform this measurement on a three-ion 2D crystal. Initially, we apply Doppler cooling and EIT cooling sequentially[62] to cool the 2D crystal down to near the motional ground state. Then, we trigger Rabi flopping and measure the Rabi frequencies of both the carrier and the micromotion sideband transition. For each flopping, we tally the total counts of three ions using PMT and fit the results with three Rabi frequencies. The fitting yields three carrier π-time values: $\{5.96, 5.40, 5.19\}\mu$s and three micromotion sideband π-time values: {474, 440, 317}μs. The modulation index, expressed as $\beta/2 = \Omega_{\text{micro}}/\Omega_{\text{carrier}}$, possesses a maximum possible value of 0.038 and a minimum possible value of 0.021, analogous to a single ion situation.

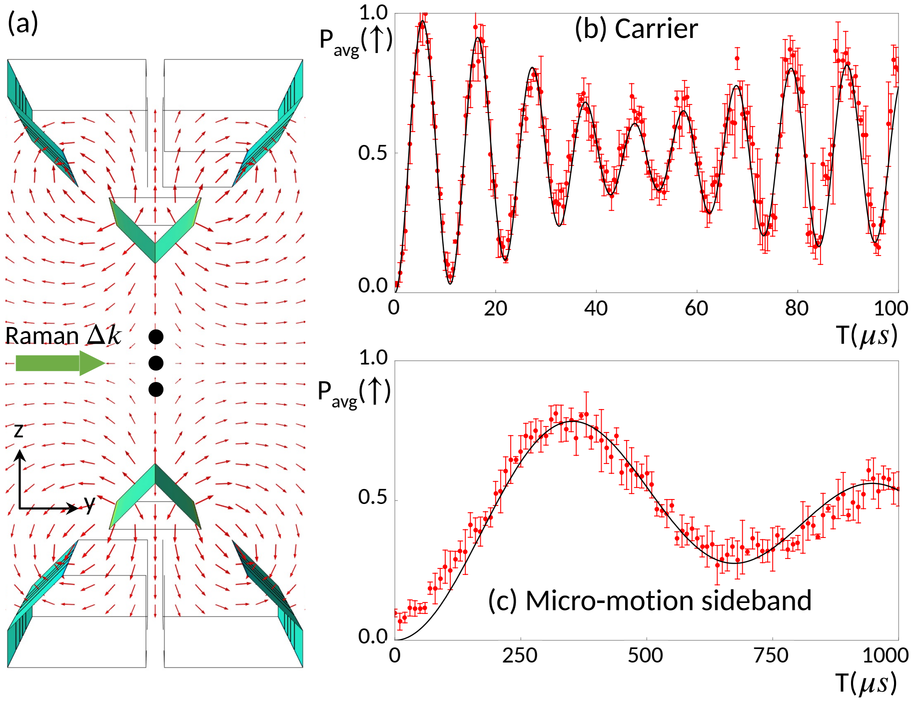

Figure 4.3 Direction and intensity of micromotion in the trap.
(**a**) A vector plot of the RF field is rendered by CPO. The simulation reveals that if the crystal is situated in the z-x plane, the direction of micromotion aligns with the z-axis and is perpendicular to the y-axis, which is the net propagation direction of Raman beams. (**b**) Carrier transition of three ions in a triangular crystal. (**c**) Micromotion transition of the three-ion-crystal post micromotion compensation. For (b) and (c), similar to Fig. 3(b), after 1000 μs of Doppler cooling and 3 μs of optical pumping, we deploy Raman laser beams with frequency differences of (a) carrier transition and (b) micro-motion sideband transition (distanced by 40 MHz from the carrier) and aggregate the total fluorescence of all three ions using PMT. The beating signal originates from the unbalanced Rabi-frequency of each ion. Error bars represent the standard deviation of project measurements over 100 repetitions.

4.5 Coherent Operations on the Vibrational Sidebands of 2D Crystals

Upon the minimization of micromotion strength, we carry out coherent manipulations of collective motional modes along the y-axis in a 2D crystal comprising three ions. The three vibrational mode frequencies are denoted as $\omega_{y1}/(2\pi) = 1.33\,\text{MHz}$, $\omega_{y2}/(2\pi) = 1.27\,\text{MHz}$, and $\omega_{y3}/(2\pi) = 1.21\,\text{MHz}$. The ions form an isosceles triangle with an apex angle measuring 260.7 degrees. For a clearer visualization of the evolution, we collect only the fluorescence from the ion at the apex angle using a PMT in this experiment.

The crystal is initially cooled to the motional ground-state through 1000 μs of Doppler cooling and 200 μs of EIT cooling. Following 3 μs of optical pumping, we implement Raman beams globally on all three ions, thus driving a blue-sideband transition for the coherent manipulation. This blue-sideband transition inadvertently induces off-resonant couplings to other motional modes.

The corresponding Hamiltonian is expressed as follows:

$$H = -\frac{i\eta}{2}\sum_{i=1}^{3}\sum_{j=1}^{3}\Omega^{(j)}b_i^{(j)}\sigma_+^{(j)}a_i e^{-i\delta_i t} + \text{H.C.}, \tag{4.4}$$

where η signifies the Lamb-Dicke parameter for a single ion, $\Omega^{(j)}$ and $\sigma_+^{(j)}$ represent the carrier Rabi frequency and spin raising operator for the j^{th} ion, respectively, and $b_i^{(j)}$ $(j = 1, 2, 3)$ embodies the i^{th} normalized mode vector of the collective mode[63].

The time evolution of the Hamiltonian as depicted in Eq. 4.4 is intricate, especially considering the off-resonant couplings to the other two motional modes. Neglecting these off-resonant couplings leads to a severe divergence between simulation and experimental data, as indicated by the black-dashed line in Fig. 4.4(b). The good agreement between red data points and the black line in Fig. 4.4(b) suggests that the coherent manipulation is reliable and the micromotion effect is negligible during the coherent operation.

We further numerically study the time evolution in the basis of quantum states, revealing a coherent evolution primarily involving states $|000\rangle\,|n=0\rangle$ and $|101\rangle\,|n=2\rangle$ (for detailed discussions, see Appendix F and Fig. 11).

We conducted an experimental study of vibrational mode heating in our trap that contains a single ion. Initially, we prepared the ground-state of the radial vibrational modes using Raman-sideband cooling. We then allowed a certain duration to pass before measuring the average phonon-number $\bar{n}$ for the mode of interest. We estimated $\bar{n}$ through Fourier transformation of the blue-sideband transitions[37]. Our findings indicate that the heating rate for the y-axis mode, corresponding to the principal axes of the 2D crystal (see Fig. 4.1(b)), is approximately 670 quanta per second. This rate is roughly 4.65 times greater than the rate under the conditions depicted in Fig. 4.1(a). Such a disparity can be justified considering that environmental electric field noise along the y-axis is likely more intense than along other axes.

4.6 Calculation of Trap Frequency

In line with Ref.[37], we formulate the time-dependent potential of the trap as follows:

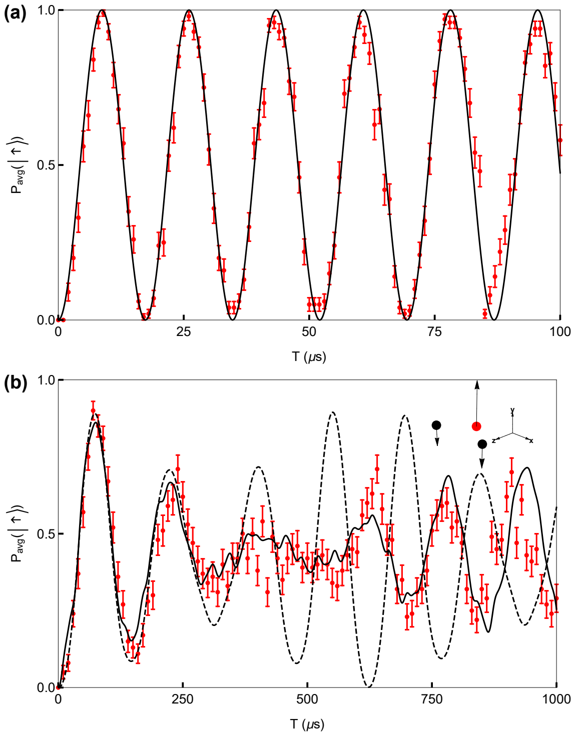

Figure 4.4 Coherent Dynamics in a Three-Ion 2D Crystal
(**a**) Carrier Rabi oscillation. (**b**) Rabi oscillation for the blue sideband transition on the zig-zag mode. Here, all the data is obtained from a three-ion 2D crystal forming an isosceles triangle with an apex angle of 260.7 degrees. We only collect fluorescence from the center ion located at the apex angle, which is highlighted in the ion structure schematic. The crystal is first subjected to a 1000 μs Doppler cooling, followed by a 200 μs EIT cooling to reach the ground state. After a 3 μs optical pumping, Raman beams are applied to the crystal to drive the blue-sideband transition of the zig-zag mode. Red points represent the experimental data, and the error bars denote the standard deviations. The solid black lines display the simulation results considering all three motional modes, while the dashed black line shows the simulation result excluding the off-resonant coupling to the other two motional modes. The mode frequencies are $\omega_{y1}/(2\pi) = 1.33\,\mathrm{MHz}$, $\omega_{y2}/(2\pi) = 1.27\,\mathrm{MHz}$, and $\omega_{y3}/(2\pi) = 1.21\,\mathrm{MHz}$. For both carrier and sideband oscillation, experimental sequences are repeated 100 times.

$$\phi(x,y,z,t) \quad = \textstyle\sum_{\mathrm{E}\in\mathrm{DC}} \frac{1}{2} V_{\mathrm{E}}(\alpha_{\mathrm{E}}x^2 + \beta_{\mathrm{E}}y^2 + \gamma_{\mathrm{E}}z^2) \tag{4.5}$$

$$nonumber \quad +V_{\mathrm{RF}}\cos(\omega_{\mathrm{RF}}t)(\alpha' x^2 + \beta' y^2 + \gamma' z^2), \tag{4.6}$$

where V_{E} denotes the voltage applied to the DCE electrode. The geometric factors αE, β_{E}, and γ_{E} are determined by the geometry of the DCE electrode. Similarly, VRF signifies the root mean square of the voltage applied to the RF electrode. The geometric factors α', β', and γ' are determined by the geometry of the RF electrode. It should be noted that the x, y, and z axes in Eq. (4.5) should represent the three principal axes of the trap potential. As the rotation of the principal axes changes, all geometric factors also change. The Laplace equation, $\Delta\Phi = 0$, imposes certain constraints on the potential:

$$\alpha + \beta + \gamma = 0, \qquad \alpha' + \beta' + \gamma' = 0. \tag{4.7}$$

Considering our symmetric RF electrodes in the axial direction, we can confidently assert that $\alpha' = 0$, implying $\beta' = -\gamma'$. By solving the Mathieu equation in three directions, we derive the following results:

$$\omega_{\mathrm{x}} = \sqrt{\frac{4e\sum_{\mathrm{E}\in\mathrm{DC}} V_{\mathrm{E}}\alpha_{\mathrm{E}}}{m\omega_{\mathrm{RF}}^2} + \frac{2e^2V_{\mathrm{RF}}^2\alpha'^2}{m^2\omega_{\mathrm{RF}}^4}}\frac{\omega_{\mathrm{RF}}}{2}, \tag{4.8}$$

$$\omega_{\mathrm{y}} = \sqrt{\frac{4e\sum_{\mathrm{E}\in\mathrm{DC}} V_{\mathrm{E}}\beta_{\mathrm{E}}}{m\omega_{\mathrm{RF}}^2} + \frac{2e^2V_{\mathrm{RF}}^2\beta'^2}{m^2\omega_{\mathrm{RF}}^4}}\frac{\omega_{\mathrm{RF}}}{2}, \tag{4.9}$$

$$\omega_{\mathrm{z}} = \sqrt{\frac{4e\sum_{\mathrm{E}\in\mathrm{DC}} V_{\mathrm{E}}\gamma_{\mathrm{E}}}{m\omega_{\mathrm{RF}}^2} + \frac{2e^2V_{\mathrm{RF}}^2\gamma'^2}{m^2\omega_{\mathrm{RF}}^4}}\frac{\omega_{\mathrm{RF}}}{2}. \tag{4.10}$$

From $\beta' = -\gamma'$, we obtain

$$\omega_{\mathrm{y}}^2 - \omega_{\mathrm{z}}^2 = \frac{e}{m}[\sum_{\mathrm{E}\in\mathrm{DC}}(\beta_{\mathrm{E}} - \gamma_{\mathrm{E}})V_{\mathrm{E}}]. \tag{4.11}$$

This equation elucidates Eq. (4.3) in the main text. As we have mentioned previously, all geometric factors are dictated by the rotation of the principal axes.

4.7 Ion-Crystal Geometry and Mode Frequency Simulation

The dashed lines in Fig. 4.1(e) are computed using the equation $\omega_y/(2.264N)^{1/4}$[50], where ω_y is a function of the RF voltage. As ω_x and ω_z surpass $\omega_y/(2.264N)^{1/4}$, the ions compose a 3D crystal. Conversely, as ω_x and ω_z fall below this threshold, the ions configure into a 2D crystal. The phase transition from a 2D crystal to a 3D crystal lacks a simple mathematical expression when the two frequencies do not concurrently exceed or drop below the threshold. For instance, if one mode lies below the bounds and the other above, a 2D crystal can still materialize. We can envision such a scenario with a homogenous crystal where $\omega_\mathrm{x} = \omega_\mathrm{z} > \omega_\mathrm{y}/(2.264N)^{1/4}$. Initially, the ions form a 3D crystal rather than a 2D one, but on lessening the ω_x confinement, the ions can create a 2D crystal at a certain ω_x. This scenario is validated for 10, 19, and 25 ions through numerical simulations of ion equilibrium positions and crystal structure studies in 2D, as illustrated in Fig. 4.5. The crystal geometries are simulated by minimizing the crystal's pseudo-potential at zero temperature. The pseudo-potential solution shifts the critical point compared to the molecular dynamics simulation that includes oscillating fields, but the overall structure resemblance remains[50,64-65]. The structural phase transition's critical point can be calculated more accurately by mapping it to the six-state clock model and including finite temperature and quantum fluctuation effects[52].

In the vicinity of the phase transition from 2D to 3D, the minimal frequency of the transverse modes tends towards zero, as described in the main text. We also numerically investigated this behavior on a 10-ion 2D crystal and displayed the result in Fig. 4.5 (d).

4.8 State Evolution in a 3-Ion 2D Crystal When Driving the Zig-Zag Mode

We numerically simulate the coherent dynamics of the blue-sideband transition on the zig-zag mode, as depicted in Fig. 4.4(b), using the Hamiltonian given in Eq. 4.4. Fig. 4.6(a) illustrates the time evolution simulation of three internal states after tracing out motional states. The evolution is complex, particularly due to the off-resonant coupling to the other two motional modes. Nonetheless, the evolution remains coherent. The initial state $|000\rangle$ is primarily transferred to $|101\rangle$ around 75 μs and is reverted around 150 μs. Even after a longer evolution period of approximately 860 μs, the $|000\rangle$ state coherently returns, which is strongly indicated in Fig. 4.4(b) experimental data. Fig. 4.6(b) illustrates the time evolution simulation of the zig-zag mode's motional states after tracing out internal

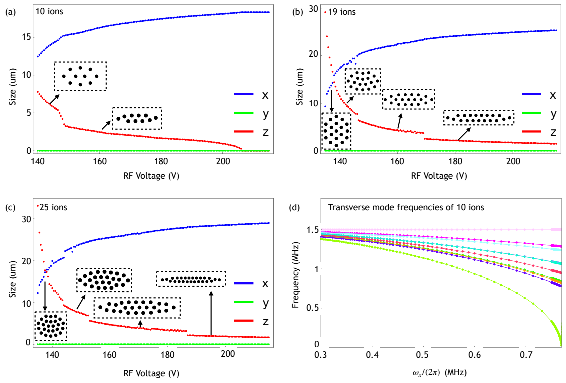

Figure 4.5 Simulation of geometry and mode frequencies
(**a-c**) The relation between crystal size and the RF voltage for the cases of 10,19, and 25 ions. Here we define the size of crystal as the maximal coordinate difference in the x, y, or z axes among the ions. The zero value of the crystal size along the y-axis shows the crystal is confined in 2D on the x-z plane. And when the size of z axis becomes zero, the ions form a linear chain. The sudden jumps of the crystal size indicates a structure phase transition. (**d**) If we squeeze the crystal formed by 10 ions along the x, z-axis, defined in Fig.3.4 (a), by increasing ω_x and ω_z, and keep the ratio $\omega_z/\omega_x = 1.3$ and $\omega_y = 1.5$MHz, the frequency of the motional modes along the y-axis will become broader. And once the minimal frequency meet zero, a phase transition from 2D to 3D happens.

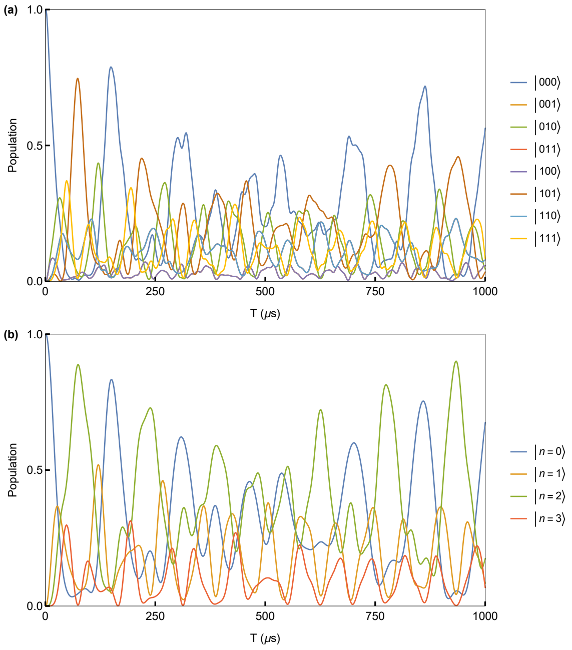

Figure 4.6 Simulations of time evolution for internal and motional states in a three-ion 2D crystal
(**a**) The time evolution for eight internal states after tracing out motional states. Due to the symmetric between two side ions, the evolution of states $|001\rangle$ and $|100\rangle$, $|011\rangle$ and $|110\rangle$ are identical. (**b**) The time evolution for the zig-zag mode in phonon number basis after tracing out internal states. The occupied phonon state is bounded to $|n = 3\rangle$ as the characteristic of three-ion blue-sideband transition.

states. Due to the three-ion blue-sideband transition characteristic, the occupied phonon state is restricted to $|n = 3\rangle$. Here we observe that the dominant motional dynamics occurs between $|n=0\rangle$ and $|n=2\rangle$ states. The $|n=2\rangle$ state is primarily associated with the $|101\rangle$ state, a notion that is validated from the motional mode vector of the zig-zag mode.

CHAPTER 5 GROUND STATE COOLING OF 2D CRYSTALS

5.1 Double-EIT cooling

Double-EIT cooling of $^{171}\mathrm{Yb}^{+}$ ions is an intricate process involving four distinct energy levels. This sets it apart from EIT cooling, which typically employs a three-level Λ scheme. As depicted in Fig.6.1 (a), the excited state $|e\rangle \equiv |F = 0, m = 0\rangle$ in the $P_{\frac{1}{2}}$ manifold is linked to the three states of $|-\rangle \equiv |F = 1, m = -1\rangle$, $|0\rangle \equiv |F = 1, m = 0\rangle$, and $|+\rangle \equiv |F = 1, m = +1\rangle$ in the $S_{1/2}$ manifold. This four-level system can be viewed as comprising two Λ-schemes, resulting in a pair of Fano-like profiles in the absorption spectrum. For instance, one Λ scheme encompasses the $|-\rangle$, $|0\rangle$ (or $|+\rangle$, $|0\rangle$) states and the excited state $|e\rangle$, which are coupled by a driving beam featuring σ^{+} (or σ^{-}) polarization and a probe beam with π polarization, respectively.

In Fig.6.1(b), we illustrate how the probe beam's absorption spectrum for an ion at rest presents two null points corresponding to two-dark states when the transition detuning $|0\rangle \leftrightarrow |e\rangle$ aligns with the detuning of the transitions $|\pm\rangle \leftrightarrow |e\rangle$. Also noteworthy are the two narrow peaks, which signify dressed states constituted by $|\pm\rangle$ and $|e\rangle$. We can ascertain the distances between these null points and the corresponding narrow peaks by evaluating the ac Stark shift of the dressed states.

The double-EIT cooling process shares a similar principle with single-EIT cooling, which leverages the asymmetric absorption profile to enhance red-sideband transitions and suppress carrier/blue-sideband transitions. This concept is illustrated in Fig. 6.1(b). The broad width of the peak allows for comprehensive cooling. Larger crystals' motional modes can be effectively cooled to near ground state due to the disparity in scattering amplitude between red- and blue-sideband transitions. The probe beam's detuning Δ_{p} is set equal to $\Delta_{\sigma+} \equiv \Delta_{\mathrm{d}} + \delta_{\mathrm{B}}$, and this action prompts the ion's internal state to be pumped to a dark state. Consequently, the ion will not absorb any photon unless the ion motion induces a differential Doppler shift $\vec{v} \cdot (\hat{k}_{\pi} - \hat{k}_{\sigma^{+}})/c = \delta_{+}$ between the π and σ^{+} transitions. As previously noted, double-EIT cooling is only capable of cooling down motional modes that are not perpendicular to the difference in wave vector $(\hat{k}_{\pi} - \hat{k}_{\sigma^{+}})$. Thus, the net k-vector should be properly aligned to the direction of the targeted motional modes. In our experiment, we opted for the right peak for cooling. Nonetheless, either

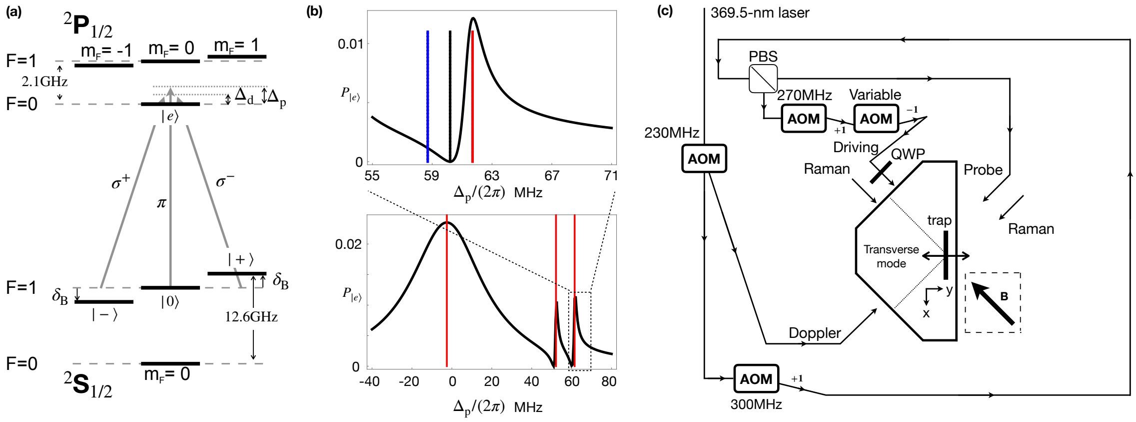

Figure 5.1 Setup for EIT cooling

(a) Pertinent energy levels of $^{171}\mathrm{Yb}^+$ applicable to EIT cooling. (b) Double-EIT's Fano-like profile. The spectrum's calculation hinges on the steady-state solution of the master equation or the scattering amplitude. The simulation parameters include $\Delta_d/(2\pi) = 55.6\mathrm{MHz}$, $\delta_B/(2\pi) = 4.6\mathrm{MHz}$, $\Omega_{\sigma,\pm}/(2\pi) = 17\mathrm{MHz}$, $\Omega_\pi/(2\pi) = 4\mathrm{MHz}$, $\nu/(2\pi) = 1.5\mathrm{MHz}$, with ν representing the mode's frequency that we aim to cool. The lower spectrum showcases a broad range, with the red lines predicting the positions of dressed states. The upper one highlights the peak used for cooling, with the blue (red) line indicating the position of the motional sideband, and the dark line signifying the carrier transition. The red-sideband is lower energy, translating to a higher detuning. (c) The optical configuration. The EIT beam is initially segregated from the Doppler cooling beam with a 14 GHz sideband, then divided into the driving and probe beams by a PBS. The relative detuning, $\Delta_d - \Delta_p$, is governed by two AOMs targeting the driving beam. The first-order diffraction of the 270MHz AOM and the negative first-order of the variable AOM are employed. The net propagating vectors Δk of both the EIT and Raman beams follow the direction of the transverse mode. A quarter-wave plate (QWP) is utilized to modify the polarization of the driving beam.

peak in the absorption spectrum can be exploited with comparable cooling rates and limits. Theoretically, it is feasible to make only one peak dominant, akin to the simple Λ-system, by unbalancing the Rabi frequencies of the σ^+ and σ^- components of the driving beam. However, in practice, we did not observe an enhancement in cooling efficiency when utilizing an unbalanced driving beam.

We present an experimental demonstration of double-EIT cooling with $^{171}\mathrm{Yb}^+$ ions, which boast a clock-state qubit with an impressive coherence time exceeding 10 minutes[66]. The qubit states $|F = 1, m = 0\rangle$ and $|F = 0, m = 0\rangle$ in the $S_{\frac{1}{2}}$ manifold exhibit an energy splitting ω_0 of 12.642812 GHz. The $^{171}\mathrm{Yb}^+$ ions are confined in a pancake-shaped potential generated by a radio-frequency Paul trap, as detailed in Ref.[67]. This configuration allows the trapped ions to form a 2D crystal. We employ a horizontal B-field of 3.32 Gauss to disrupt the dark state resonance in Doppler cooling, as depicted in Fig.6.1 (c).

The EIT beams comprise two lasers that closely align with the $S_{\frac{1}{2}}|F = 1, m = 0\rangle$ to

$P_{\frac{1}{2}}|F=0,m=0\rangle$ transition. These EIT beams are arranged such that the difference in wave vectors parallels the transverse direction of the motional modes. One beam serves to drive the $\sigma_\pm$ transitions between $|\pm\rangle \leftrightarrow |e\rangle$, while the other acts as a probe beam, coupling the energy levels $|0\rangle \leftrightarrow |e\rangle$. The detuning Δ_p of the probe beam is fixed at $(2\pi)55.6$ MHz, and the detuning Δ_d of the driving beam is adjusted by modifying the frequency difference between two AOMs, as shown in Fig. 6.1(c). We assess the Rabi frequency and the polarization of the EIT beams by observing the differential ac Stark shift of the clock state qubit and the Zeeman state qubits[68? -69]. The Rabi frequencies, $\Omega_{\sigma_-}, \Omega_\pi, \Omega_{\sigma_+}/(2\pi)$, for the driving beam of 24μW and the probe beam of 5.5μW are 16.74,1.72, 18.03MHz and 1.49, 6.67, 3.17MHZ, respectively.

Fig.5.2 (a) outlines the experimental sequence undertaken to investigate double-EIT cooling with a single ion. For a single $^{171}\mathrm{Yb}^+$ ion, the secular trap frequencies amount to $\omega_\mathrm{y}/2\pi = 2.38$ MHz in the transverse direction and $\omega_\mathrm{x}, \omega_\mathrm{z}/2\pi = 0.42, 0.47$ MHz in the crystal plane. We initiate with Doppler cooling, resulting in Doppler-limit temperatures around a phonon number of $\bar{n} \approx 7$. Following Doppler cooling, 95% of the internal state of ions populates the $S_{\frac{1}{2}}|F=1\rangle$ manifold. Subsequently, we expose the system to the EIT beams for a duration τ_EIT. To measure the final phonon number $\bar{n}$, we perform a 3μs optical pumping to prepare the ground state $S_{\frac{1}{2}}|F=0,m=0\rangle$. By driving the blue-sideband transition and fitting time evolution[37], we extract the average phonon number $\bar{n}$.

Our experimental investigation of double-EIT cooling dynamics is conducted with relative detuning $\Delta_\mathrm{p} - \Delta_\mathrm{d} = 4.55$MHz. We measure the mean occupation number $\bar{n}$ at various cooling durations τ_EIT, as indicated in Fig.5.2 (b). The mean vibrational number $\bar{n}$ is ascertained by fitting the blue-sideband transitions, as displayed in Fig.5.2 (c) prior to and (d) subsequent to EIT cooling. Absent EIT cooling, oscillations on the blue-sideband transition decay quickly due to varying excitations on different vibrational number states with divergent Rabi frequencies. As shown in Fig.5.2 (d), the minimum value of $\bar{n}_\mathrm{min} = 0.06(\pm 0.059)$ achieved with EIT cooling is indicative of near ground-state cooling, comparable to sideband cooling. The $1/e$ cooling time $\tau_\mathrm{cool} = 1/\gamma_\mathrm{cool}$, where γ_cool is the cooling rate, is $30(\pm 1.6)\mu$s. Thus, a duration of 200 μs is sufficient to reach the ground state.

In order to identify the optimal detuning and cooling range for double-EIT cooling, we adjusted the frequency difference between the EIT beams. The efficiency of EIT cooling

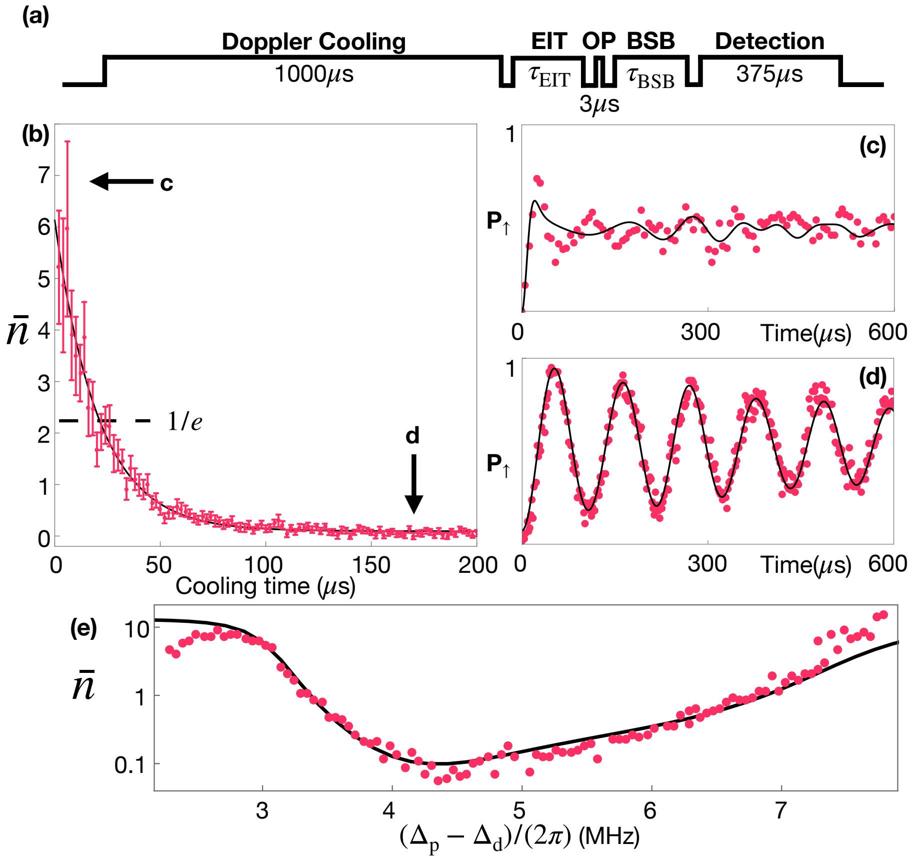

Figure 5.2 EIT cooling speed

(a) Experimental sequence for exploring EIT cooling of a single trapped ion. (b) Cooling dynamics for the transverse mode along the y-axis. Red points are experimental data obtained by fitting blue-sideband transitions shown in (c) and (d). Error bars denote fitting errors. The black line is exponential fit. The horizontal dashed line indicates 1/e of initial phonon number. (c,d) The blue-sideband transition after (c) Doppler cooling and (d) EIT cooling of 200μs. (e) Average phonon number $\bar{n}$ at the end of double-EIT cooling versus the relative detuning between the probe beam and the driving beam. The black line is numerical simulation result obtained by solving the master equation .

in our experiment is largely determined by the absorption strength ratio between the red-sideband and blue-sideband transitions, as shown in Fig. 6.1(b). This ratio is directly controlled by the detuning of the driving beam, denoted as Δ_d. We found the optimal detuning $(\Delta_p - \Delta_d)/(2\pi)$ for double-EIT cooling to be 4.55 MHz, which corresponds closely to the predicted value of 4.57 MHz. This value is derived from $\delta_B + \delta_{DR} - \nu$, where δ_{DR}= (2π) 2.31 MHz refers to the dressed-state ac Stark shift. To verify our experimental findings, we performed numerical simulations, accounting for a heating rate of 0.67ms^{-1} in the transverse direction. The simulated average phonon numbers, depicted by the solid line in Fig.5.2 (e), demonstrated a satisfactory agreement with our experimental results.

The EIT cooling rate $\gamma_{\rm cool}$ and the minimum phonon number $n_{\rm min}$ as functions of intensities of the EIT beams are shown in Fig. 5.3. We characterize the cooling efficiency

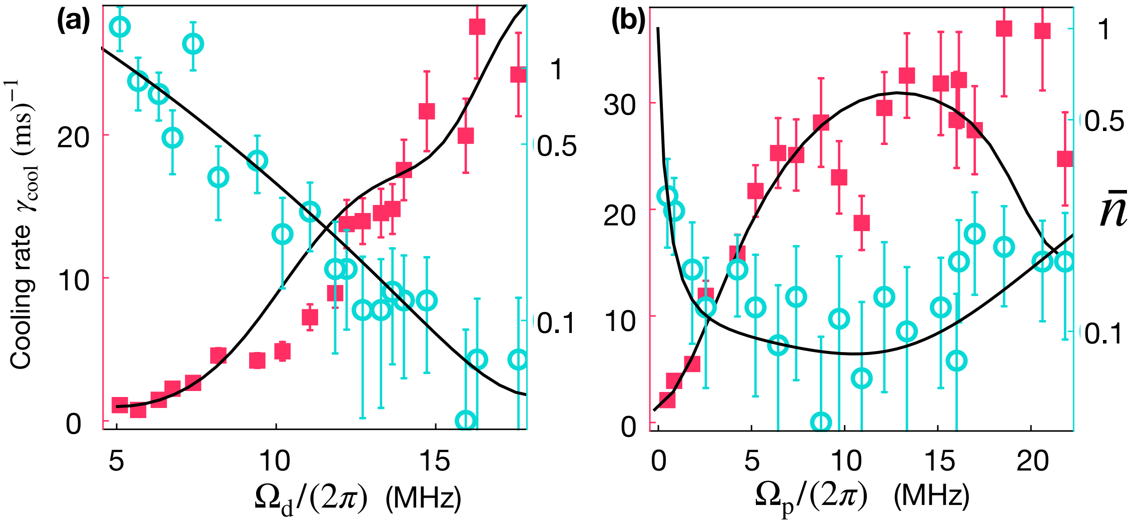

Figure 5.3 EIT power
The final mean phonon numbers (circular points) and the cooling rates (square points) are plotted versus the power of (a) the driving beam and (b) the probe beam. Error bars denote the fitting uncertainties of blue-sideband evolutions, similar to Fig. 5.2(c,d). Solid lines are numerical simulation results obtained by solving the master equation .

as the power of the driving (probe) beam varies while the power of the probe (driving) beam is fixed at 5.5μW, $\Omega_{\mathrm{p}}/2\pi = 6.67$ MHz (24μW, $\Omega_{\mathrm{d}}/2\pi = 17.39$ MHz). At each point of laser powers, we search the optimal EIT detuning ($\Delta_{\mathrm{p}} - \Delta_{\mathrm{d}}$). As shown in Fig. 5.3, numerical simulations match the experimental results fairly well, while the discrepancies of cooling rates could origin from the overall power fluctuations. As the power of the driving beam increases to the maximal possible value in our experiment, the cooling efficiency is also enhanced, as shown in Fig.5.3(a). On the other hand, Fig.5.3(b) shows that both cooling rate and limit have a local optimum. To balance the cooling rate and limit, we determine the optimal power of the probe beam by minimizing the ratio between final phonon number and cooling rate of the numerical curve in Fig. 5.3(b). Finally, we found $\Omega_{\mathrm{p}}/(2\pi) = 11$ MHz is optimal for cooling.

To assess double-EIT cooling on a large ion crystal, we store a 2D crystal of 12 ions in a pancake harmonic potentials with secular trap frequencies $\omega_{\mathrm{y}}/(2\pi) = 1.22$MHz in the transverse direction, and $\{\omega_{\mathrm{x}}, \omega_{\mathrm{z}}\}/(2\pi) = \{0.34, 0.42\}$MHz in the crystal plane. With this smaller ω_{y}, the heating rate is increased to 0.77ms^{-1}. We suppress the micromotion of the 2D crystal in the transverse modes by adjusting the plane of the crystal to be in line with the micromotion direction, which is the z-axis shown in Fig. 6.1(c). Then, the direction of dominant micromotion is perpendicular to directions of the transverse modes and the net-propagation direction of the EIT beams. In such a situation, the effect of micromotion is eliminated in double-EIT cooling; therefore, we can perform efficient cooling. Indeed, we measure the strength of the micromotion sideband in the Raman spectroscopy and observe it is at a similar level to a single ion[67]. Double-EIT cooling of a 12-ion crystal is observed from Raman absorption spectrum. Fig. 5.4 (a) depicts the spectrum with only Doppler cooling, where the peaks of blue-sideband (blue curve) and red-sideband (red curve) transitions possess similar heights across all motional modes, which indicates the phonon numbers are much larger than 1. Fig.5.4 (b) shows the spectrum after both Doppler and EIT cooling, where the reduction of red-sideband transitions indicates simultaneous ground-state cooling of all transverse modes. The small peak in the spectrum of red-sideband transitions originates from imperfect ground-state cooling of the center of mass (COM) mode with linearly scaled heating rate. We numerically simulate the red-sideband absorption spectrum of the crystal in the vicinity of each mode for the parameters of our experiment[70]. The estimated phonon numbers of COM mode is 1.04 (±0.26) .

We also employ optical-dipole-force (ODF) thermometry[71] to measure the final phonon number of the center-of-mass (COM) mode. The ODF is generated by simultaneously driving red-sideband and blue-sideband transitions, resulting in the emergence of the $\sigma_x\sigma_x$ interaction. With ion-phonon coupling, this interaction can induce decoherence in the x basis. To probe this decoherence, we adopt Ramsey measurements, as shown in Fig. 5.4(c). Initially, all qubits are prepared in their ground state in the σ_z basis, denoted as $|\downarrow\rangle$ z. Then, the ODF is applied for two fixed durations, τODF, with a spin-echo pulse sandwiched in between. Fig. 5.4(d) presents the spectrum near the COM mode of the crystal with different phonon numbers. The crystal's temperature is measured by fitting the spectrum to the formula given in Equation (35), where the $\bar{n}$ values for Doppler cooling and EIT cooling are 10.72 (±4.23) and 1.04 (±0.61), respectively. We calibrate the strength of the ODF beams by measuring the Lamb-Dicke parameter and the Rabi frequency of the carrier transition.

To investigate the cooling dynamics for the COM mode of a crystal with 12 ions, we develop a simple method to estimate $\bar{n}$ instead of using the entire ODF spectrum in Fig. 5.4(d). By fixing the detuning at the position with the largest decoherence, we convert the heights of the ODF signal to the mean phonon number, $\bar{n}$. We observe a cooling rate and a cooling limit consistent with those of a single ion. In the case of 12 ions, the measured cooling rate and limit for a single ion are 22.1 (±0.1)ms^{-1} and 0.34(±0.25), respectively, as shown in Fig. 5.4(e). With 12 ions, the rate and limit are 15.9(±0.1)ms^{-1} and 1.04(±0.61), respectively. The cooling rate is reduced, and the cooling limit is in-

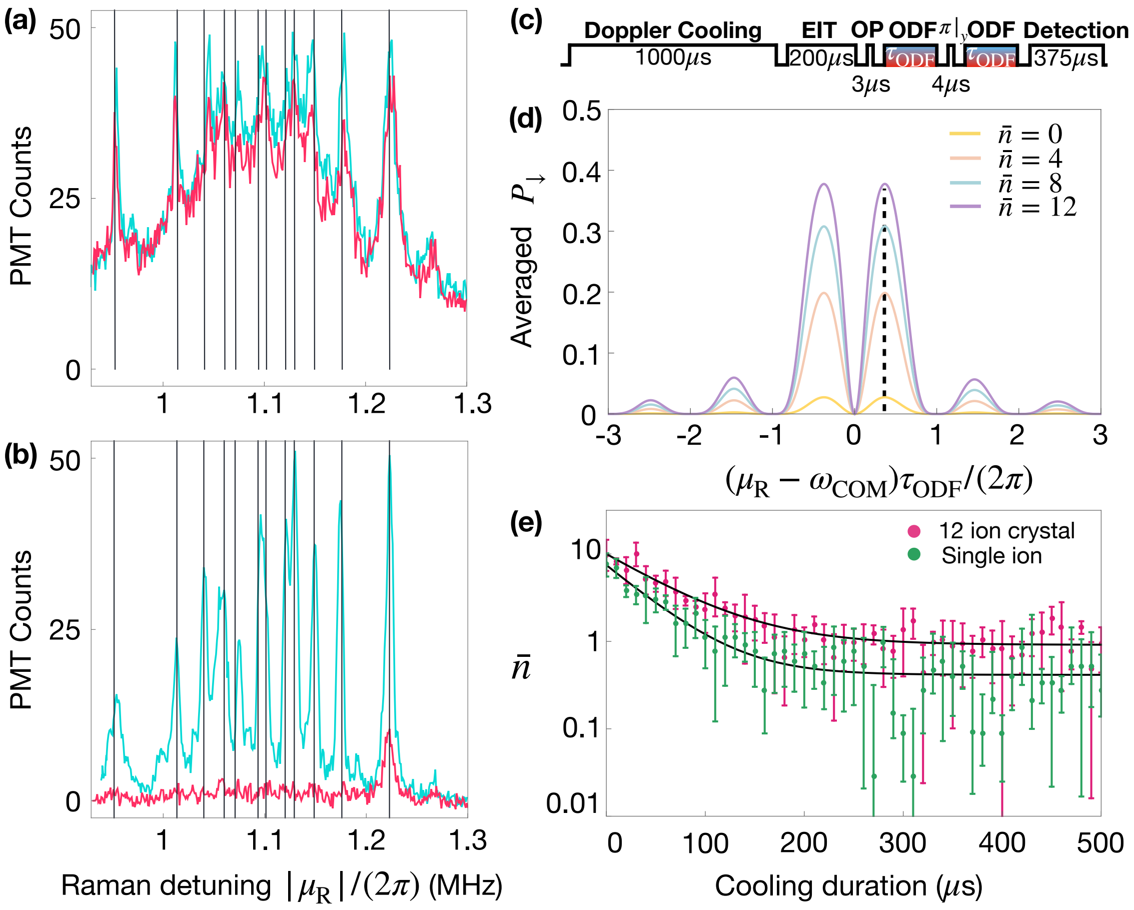

Figure 5.4 EIT cooling for 2D ion crystal
(a,b) Blue-sideband (blue curve) and red-sideband (red curve) spectrum after (a) Doppler cooling and (b) EIT cooling. The vertical axis represents the count globally collected by PMT. The horizontal axis $\mu_R = \omega_R - \omega_0$ is the detuning of the Raman transition from the qubit transition. Vertical lines indicate the locations of 12 motional modes perpendicular to the 2D-crystal plane. (c) Pulse sequence for the ODF thermometry. (d) ODF spectrum with different average phonon number. The dashed black line indicates the position we choose for the cooling rate measurement. (e) Cooling dynamics for a single ion (green) and a 2D crystal with 12 ions (red). The dots are experimental data. The error bars represent the standard deviation induced by the quantum projection noise. Solid lines are fitting curves by exponential decay functions.

creased for 12 ions due to heating rates proportional to the number of ions, which amount to 0.61(±0.08) ms^{-1} per ion. In our experiment, we do not observe the more efficient EIT cooling reported in Refs.[72-73] within our error bars, indicating the need for further experimental or theoretical investigation.

5.2 The dark states

Considering the semi-classical treatment for the system of Fig. 6.1(a) in the rotating frame, we have the Hamiltonian

$$\hat{H} = \begin{pmatrix} 0 & \frac{\Omega_{\sigma-}}{2} & -\frac{\Omega_\pi}{2} & \frac{\Omega_{\sigma+}}{2} \\ \frac{\Omega_{\sigma-}}{2} & \Delta_\mathrm{d} + \delta_\mathrm{B} & 0 & 0 \\ -\frac{\Omega_\pi}{2} & 0 & \Delta_\mathrm{p} & 0 \\ \frac{\Omega_{\sigma+}}{2} & 0 & 0 & \Delta_\mathrm{d} - \delta_\mathrm{B} \end{pmatrix} \tag{5.1}$$

where the basis is $\{|e\rangle, |+\rangle, |0\rangle, |-\rangle\}$, Δ_d is the detuning between the driving laser and the $|0\rangle \leftrightarrow |e\rangle$ transition, Δ_p is the detuning between the probe laser and the $|0\rangle \leftrightarrow |e\rangle$ transition, and δ_B is the Zeeman splitting. Here we denote $\hbar = 1$.

Once the detuning of the probe beam matches to one of the Zeeman level $\Delta_\mathrm{p} = \Delta_\mathrm{d} + \delta_\mathrm{B} \equiv \Delta$, the Hamiltonian can be written as

$$\hat{H} = \begin{pmatrix} 0 & \frac{\Omega_{\sigma-}}{2} & -\frac{\Omega_\pi}{2} & \frac{\Omega_{\sigma+}}{2} \\ \frac{\Omega_{\sigma-}}{2} & \Delta & 0 & 0 \\ -\frac{\Omega_\pi}{2} & 0 & \Delta & 0 \\ \frac{\Omega_{\sigma+}}{2} & 0 & 0 & \Delta - 2\delta_\mathrm{B} \end{pmatrix} \tag{5.2}$$

This Hamiltonian gives us one dark state

$$|D_1\rangle = \frac{1}{\sqrt{\Omega_\pi^2 + \Omega_{\sigma-}^2}}(\Omega_\pi\,|+\rangle + \Omega_{\sigma-}|0\rangle) \tag{5.3}$$

And the coincidence with the other Zeeman level gives us the second dark state

$$|D_2\rangle = \frac{1}{\sqrt{\Omega_\pi^2 + \Omega_{\sigma+}^2}}(\Omega_{\sigma+}|0\rangle + \Omega_\pi\,|-\rangle) \tag{5.4}$$

5.3 The scattering amplitude interpretation for the bright Resonance

To gain a more precise understanding of the interaction between laser beams and this four-level atomic system, we can quantize the laser field. This allows us to express the Hamiltonian as follows:

$$H = H_0 + V_{\sigma+} + V_{\sigma-} + V_\pi + \sum_v V_v, \tag{5.5}$$

where

$$\begin{aligned} H_0 &= E_{\sigma+} \left|-\right\rangle \left\langle-\right| + E_\pi |0\rangle\langle 0| + E_{\sigma-} \left|+\right\rangle \left\langle+\right| + E_e |e\rangle\langle e| + \omega_{\sigma-} a^\dagger_{\sigma-} a_{\sigma-} \\ &\quad + \omega_\pi a^\dagger_\pi a_\pi + \omega_{\sigma+} a^\dagger_{\sigma+} a_{\sigma+} + \sum_v \omega_v a^\dagger_v a_v \\ V_{\sigma+} &= \frac{d_{\sigma+}}{2} (a_{\sigma+} |e\rangle \left\langle-\right| + a^\dagger_{\sigma+} \left|-\right\rangle \langle e|) \\ V_\pi &= \frac{d_\pi}{2} (a_\pi |e\rangle\langle 0| + a^\dagger_\pi |0\rangle\langle e|) \\ V_{\sigma-} &= \frac{d_{\sigma-}}{2} (a_{\sigma-} |e\rangle \left\langle+\right| + a^\dagger_{\sigma-} \left|+\right\rangle \langle e|) \\ V_v &= \frac{d_v}{2} (a_v |e\rangle \left\langle-\right| + a^\dagger_v \left|-\right\rangle \langle e| + a_v |e\rangle\langle 0| + a^\dagger_v |0\rangle\langle e| + a_v |e\rangle \left\langle+\right| + a^\dagger_v \left|+\right\rangle \langle e|). \end{aligned} \tag{5.6}$$

Here, the last term represent the interaction with the vacuum field. Basically, the absorption spectra is proportional to the squared scattering amplitude of the transition

$$|i\rangle \equiv |0, 1, N_1, N_2, 0\rangle \rightarrow |f\rangle \equiv |0, 0, N_1, N_2, 1\rangle, \tag{5.7}$$

where the first index represent the atom‘s internal state, the second index represents the Fock state of the probe field, and the last three terms represent the Fock states of the σ_- field, σ_+ field, and the vacuum field, respectively. It is important to note that the absorption spectrum refers to the process in which the atom absorbs one photon and subsequently emits it into the vacuum, with a portion of it being detectable by a photomultiplier tube (PMT).

The scattering amplitude of such a process can be calculated by the T matrix

$$T = \langle f|V|\mathrm{i}\rangle + \lim_{\eta \to 0_+} \left\langle f \middle| V \frac{1}{E_\mathrm{i} - H + i\eta} V \middle| i \right\rangle \tag{5.8}$$

and due to $V = V_{\sigma+} + V_{\sigma-} + V_\pi + \sum_v V_v$, $V|i\rangle$ and $V|f\rangle$ can be written by

$$V|i\rangle = \frac{\Omega_\pi}{2}|\varphi_e\rangle,\ V|f\rangle = \frac{\Omega_v}{2}|\varphi_e\rangle. \tag{5.9}$$

where we denote $|\varphi_e\rangle \equiv |e, 0, N_1, N_2, 0\rangle$. There are two states strongly coupled to $|\varphi_e\rangle$, which are

$$|-, 0, N_1 + 1, N_2, 0\rangle,\ |+, 0, N_1, N_2 + 1, 0\rangle, \tag{5.10}$$

since

$$V|+, 0, N_1 + 1, N_2, 0\rangle = \frac{\Omega_{\sigma-}}{2}|\varphi_e\rangle,\ V|-, 0, N_1, N_2 + 1, 0\rangle = \frac{\Omega_{\sigma+}}{2}|\varphi_e\rangle, \tag{5.11}$$

respectively. We note that the subspace is closed. We can calculate the T matrix by projecting the Hamiltonian to the subspace spanned by $\{|+, 0, N_1+1, N_2, 0\rangle, |-, 0, N_1, N_2+1, 0\rangle, |\varphi_e\rangle\}$.

In the second order perturbation theory[74], the effective Hamiltonian in this subspace can be calculated by

$$PH_{\text{eff}}P = PH_0P + PVP + PVQ\frac{1}{E_0 - QH_0Q}QVP, \tag{5.12}$$

where P is the projection operator to the subspace and $Q = 1 - P$. After calculating all the terms, the effective Hamiltonian can be simplified by

$$\hat{H}_{\text{eff}} = \begin{pmatrix} \Delta_\pi + i\frac{\Gamma}{2} & -\frac{\Omega_{\sigma-}}{2} & -\frac{\Omega_{\sigma+}}{2} \\ -\frac{\Omega_{\sigma-}}{2} & \Delta_\pi - \Delta_{\sigma-} & 0 \\ -\frac{\Omega_{\sigma+}}{2} & 0 & \Delta_\pi - \Delta_{\sigma+}. \end{pmatrix} \tag{5.13}$$

Therefore the fluorescence, $W(\Delta) = |T(\Delta)|^2$, which is proportional to the square of the scattering amplitude is

$$W(\Delta_\pi) = \frac{16(\Delta_\pi - \Delta_{\sigma-})^2(\Delta_\pi - \Delta_{\sigma+})^2}{Z} \tag{5.14}$$

where

$$\begin{aligned} Z =& 4\Gamma^2(\Delta_\pi - \Delta_{\sigma-})^2(\Delta_\pi - \Delta_{\sigma+})^2 + \\ & \left[4\Delta_\pi(\Delta_\pi - \Delta_{\sigma+})(\Delta_\pi - \Delta_{\sigma-}) - (\Delta_\pi - \Delta_{\sigma+})\Omega_{\sigma-}^2 - (\Delta_\pi - \Delta_{\sigma-})\Omega_{\sigma+}^2\right]^2 \end{aligned}$$

And Γ is the total decay rate of the excited state. The bright resonance will appear when

$$4\Delta_\pi(\Delta_\pi - \Delta_{\sigma-})(\Delta_\pi - \Delta_{\sigma+}) - (\Delta_\pi - \Delta_{\sigma+})\Omega_{\sigma-}^2 - (\Delta_\pi - \Delta_{\sigma-})\Omega_{\sigma+}^2 = 0 \tag{5.15}$$

In the experiment, we control Δ_π by changing the detuning of the probe beam that has only the π-polarization. The three roots independently correspond to the big Doppler peak and two narrow Fano peaks.

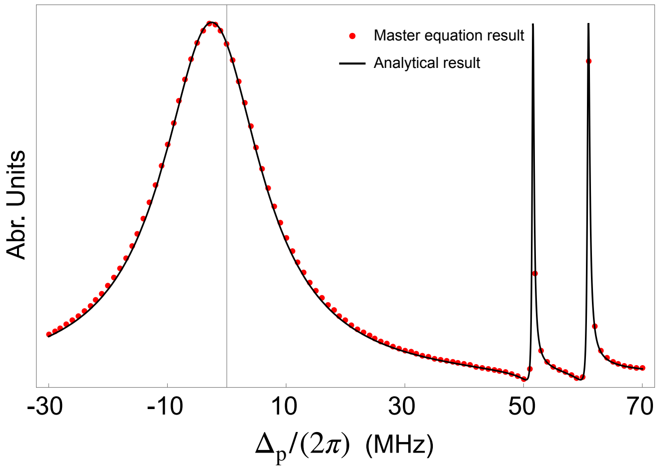

Figure 5.5 The spectrum calculated by the master equation and the analytical solution. Here we set $\Gamma/(2\pi) = 21$ MHz, $\Delta_{\sigma+}/(2\pi) = 50.4$ MHz, $\Delta\sigma-/(2\pi) = 59.6$ MHz, $\Omega_{\sigma-}/(2\pi) = \Omega_{\sigma+}/(2\pi) = 17$ MHz, and $\Omega_\pi/(2\pi) = 0.5$ MHz. The dot represent the result calculated from the master equation and the curve is calculated by the Eq.(5.14).

5.4 The dressed-states interpretation for the bright resonance

With only two driving beams and no probe beam, we have the Hamiltonian

$$\hat{H} = \begin{pmatrix} 0 & \frac{\Omega_{\sigma-}}{2} & 0 & \frac{\Omega_{\sigma+}}{2} \\ \frac{\Omega_{\sigma-}}{2} & \Delta_{\sigma-} & 0 & 0 \\ 0 & 0 & 0 & 0 \\ \frac{\Omega_{\sigma+}}{2} & 0 & 0 & \Delta_{\sigma+} \end{pmatrix} \tag{5.16}$$

The energy of the dressed states can be calculated by diagonalizing the above Hamiltonian, which results in solving the following equation

$$\frac{1}{4}\lambda\left[4\lambda(\lambda-\Delta_{\sigma+})(\lambda-\Delta_{\sigma-})-(\lambda-\Delta_{\sigma+})\Omega_{\sigma-}^2-(\lambda-\Delta_{\sigma-})\Omega_{\sigma+}^2\right]=0. \tag{5.17}$$

The energies of the dressed states can be observed by applying a probe beam with π-polarization, as shown in Fig. 5.6. This observation is consistent with the result obtained from Equation (5.15).

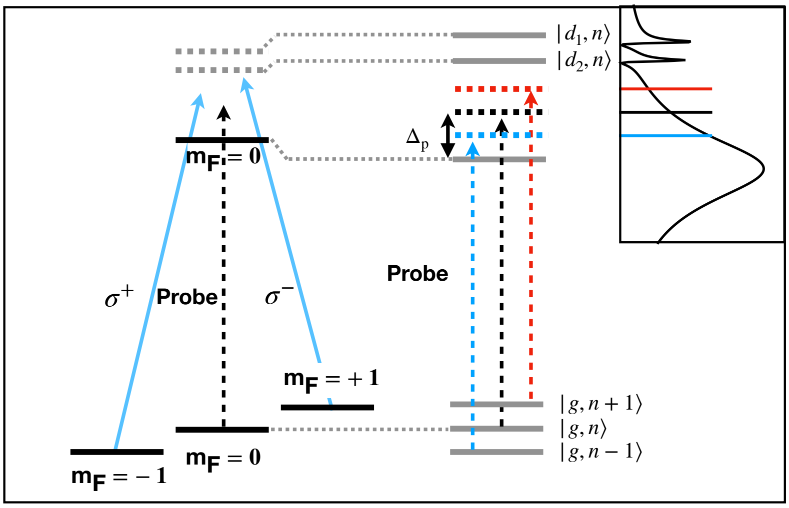

Figure 5.6 Dressed states

The dressed states. The gray dotted lines are the energy levels without the interaction with the $\Omega_{\sigma,\pm}$ fields. The gray solid lines are the dressed states formed by the laser field and the atomic levels. $|d_1, n\rangle$ and $|d_2, n\rangle$ represent the dressed states with phonon number n. $|g, n\rangle$ represent the $m_F = 0$ state with phonon number n. The dashed colored lines represent the virtual excited state of $|g\rangle$ with different phonon number, and blue- and red-sideband transitions, as shown in the spectrum. When the red dashed line matches $|d_2, n\rangle$, the transition $|g, n+1\rangle \leftrightarrow |d_2, n\rangle$ is driven, which is a red-sideband transition.

5.5 The master equation treatment for the double-EIT cooling

The Hamiltonian that describes the interaction between the four-level system and the laser fields shown in Fig. 1(a) can be written as

$$\hat{H} = \begin{pmatrix} \omega_{|e\rangle} & \frac{\Omega_{\sigma-}}{2}e^{-i(\vec{k}_\mathrm{d}\cdot\vec{r}-\omega_\mathrm{d}t)} & -\frac{\Omega_\pi}{2}e^{-i(\vec{k}_\mathrm{p}\cdot\vec{r}-\omega_\mathrm{p}t)} & \frac{\Omega_{\sigma+}}{2}e^{-i(\vec{k}_\mathrm{d}\cdot\vec{r}-\omega_\mathrm{d}t)} \\ \frac{\Omega_{\sigma-}}{2}e^{i(\vec{k}_\mathrm{d}\cdot\vec{r}-\omega_\mathrm{d}t)} & \omega_{|+\rangle} & 0 & 0 \\ -\frac{\Omega_\pi}{2}e^{i(\vec{k}_\mathrm{p}\cdot\vec{r}-\omega_\mathrm{p}t)} & 0 & \omega_{|0\rangle} & 0 \\ \frac{\Omega_{\sigma+}}{2}e^{i(\vec{k}_\mathrm{d}\cdot\vec{r}-\omega_\mathrm{d}t)} & 0 & 0 & \omega_{|-\rangle}, \end{pmatrix} \tag{5.18}$$

where $\vec{k}_{\mathrm{p(d)}}$ and $\omega_{\mathrm{p(d)}}$ are the k-vector and the frequency of the probe (driving) beam and $\omega_{|e\rangle}, (\omega_{|-\rangle}\omega_{|0\rangle}, \omega_{|+\rangle})$ are the energies of the corresponding levels. For a rest ion, in the rotating frame the Hamiltonian can be simplified to

$$\hat{H}_\mathrm{s} = \begin{pmatrix} 0 & \frac{\Omega_{\sigma-}}{2} & -\frac{\Omega_\pi}{2} & \frac{\Omega_{\sigma+}}{2} \\ \frac{\Omega_{\sigma-}}{2} & \Delta_\mathrm{d}+\delta_\mathrm{B} & 0 & 0 \\ -\frac{\Omega_\pi}{2} & 0 & \Delta_\mathrm{p} & 0 \\ \frac{\Omega_{\sigma+}}{2} & 0 & 0 & \Delta_\mathrm{d}-\delta_\mathrm{B} \end{pmatrix} \tag{5.19}$$

The absorption spectrum can be obtained by numerical solving the steady state solution of the master equation corresponding to the Hamiltonian Eq.(5.19)

$$\frac{d\hat{\rho}}{dt} = -i[\hat{H}_\mathrm{s}, \hat{\rho}] + \mathcal{L}\rho, \tag{5.20}$$

where $\mathcal{L}$ is the Lindblad operator corresponding to the three spontaneous decay channel $\mathcal{L}\rho = \sum_{i=1}^{3} c_i\rho c_i^\dagger - \frac{1}{2}\{c_i^\dagger c_i, \rho\}$ and $c_1 = \sqrt{\Gamma/3}\,|+\rangle\langle e|$, $c_2 = \sqrt{\Gamma/3}\,|0\rangle\langle e|$, $c_1 = \sqrt{\Gamma/3}\,|-\rangle\langle e|$.

For a moving ion, the Hamiltonian in rotating frame can be written as

$$\hat{H}_\mathrm{m} = \begin{pmatrix} 0 & \frac{\Omega_{\sigma-}}{2}e^{-i\vec{k}_\mathrm{d}\cdot\vec{r}} & -\frac{\Omega_\pi}{2}e^{-i\vec{k}_\mathrm{p}\cdot\vec{r}} & \frac{\Omega_{\sigma+}}{2}e^{-i\vec{k}_\mathrm{d}\cdot\vec{r}} \\ \frac{\Omega_{\sigma-}}{2}e^{i\vec{k}_\mathrm{d}\cdot\vec{r}} & \Delta_\mathrm{d}+\delta_\mathrm{B} & 0 & 0 \\ -\frac{\Omega_\pi}{2}e^{i\vec{k}_\mathrm{p}\cdot\vec{r}} & 0 & \Delta_\mathrm{p} & 0 \\ \frac{\Omega_{\sigma+}}{2}e^{i\vec{k}_\mathrm{d}\cdot\vec{r}} & 0 & 0 & \Delta_\mathrm{d}-\delta_\mathrm{B}. \end{pmatrix} \tag{5.21}$$

In the simulation of the cooling effect, we set $\vec{k}\mathrm{d} = -\vec{k}\mathrm{p} = \hat{y}$ to selectively address the relevant motional mode using the laser beams. Considering the quantized motion of ions trapped in a harmonic potential, the position operator can be decomposed into the creation and annihilation operators of the phonon as $\hat{y} = \sqrt{\frac{1}{2M\omega_{\mathrm{COM}}}}(\hat{a} + \hat{a}^{\dagger})$, where ω_{COM} is the frequency of the harmonic potential. The cooling rate can be calculated by solving the time evolution of the master equation corresponding to $\hat{H}_{\mathrm{m}}$, and the cooling limit can be determined by the average phonon number of the steady-state solution of the master equation.

The heating is represented by an additional Lindblad operator $c_{\mathrm{h}} = \alpha a^{\dagger}$, where α describes the strength of heating and $a^{\dagger}$ is the creation operator of the COM mode. In the numerical simulation presented in the main text, we use the parameter values $\alpha = 0.0259$, corresponding to a heating rate of 0.67 quanta/ms, $\Delta_{\mathrm{d}}/(2\pi) = 55.6$ MHz, $\Delta_{\mathrm{p}}/(2\pi) = 59.82$ MHz, $\Omega_{\pi}/(2\pi) = 6.67$ MHz, $\Omega_{\sigma,+}/(2\pi) = 19.91$ MHz, $\Omega_{\sigma,-}/(2\pi) = 19.52$ MHz, $\delta_{\mathrm{B}}/(2\pi) = 4.6$ MHz, and the trap frequency $\nu/(2\pi) = 2.38$ MHz.

5.6 Measurements of Rabi frequencies of the probe and driving beams

We measure the Rabi frequencies of the probe and driving laser beams by observing Ramsey oscillations from the differential AC-stark shift of the beams. We use the clock qubit and the Zeeman qubits to measure all the three components of polarization, as shown in the Fig.5.7.

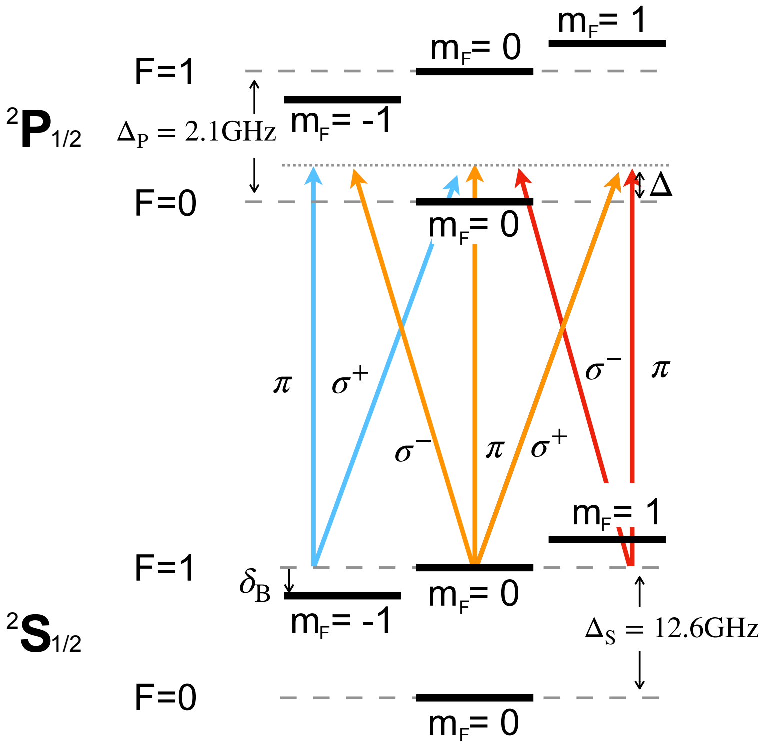

Figure 5.7 Energy levels

Energy levels of the ^{171}Yb$^+$. The AC stark shift originated from different transitions are labelled by different colors. The blue and red lines corresponding to the transitions contribute to the differential AC stark shift of the Zeeman qubits and the orange lines corresponding to the transitions for the clock qubit.

For the clock state qubit $^2S_{1/2}|F=0, m_F=0\rangle$ to $^2S_{1/2}|F=1, m_F=0\rangle$, the AC-stark is given by the following formula

$$\Delta_{\mathrm{AC}}^{\mathrm{clock}}(\Omega_+, \Omega_-, \Omega_\pi, \Delta) = \Omega_\pi^2\left(\frac{1}{\Delta} + \frac{1}{\Delta_P + \Delta_S - \Delta}\right) + (\Omega_-^2 + \Omega_+^2)\left(\frac{1}{\Delta_P + \Delta_S - \Delta} - \frac{1}{\Delta_P - \Delta}\right), \tag{5.22}$$

where the first term comes from the transition $^2S_{1/2}|F=1, m_F=0\rangle$ to $^2P_{1/2}|F=0, m_F=0\rangle$ and $^2S_{1/2}|F=0, m_F=0\rangle$ to $^2P_{1/2}|F=1, m_F=0\rangle$ while the second term comes from the transition $^2S_{1/2}|F=1, m_F=0\rangle$ to $^2P_{1/2}|F=1, m_F=\pm1\rangle$ and $^2S_{1/2}|F=0, m_F=0\rangle$

to ${}^2P_{1/2}|F = 1, m_F = \pm 1\rangle$. Including the dephasing due to the spontaneous emission whose strength is proportional to the $1/\Delta^2$, the Ramsey oscillation can be described by

$$\sin^2[\Delta_{\text{AC}}^{\text{clock}}(\Omega_+, \Omega_-, \Omega_\pi, \Delta)t] \times e^{-\Gamma*\Omega_\pi^2 t/\Delta^2} e^{-\Gamma*(\Omega_-^2+\Omega_+^2)t/(\Delta_\text{P}-\Delta)^2}. \tag{5.23}$$

In a similar way, Ramsey oscillations of the two Zeeman qubits can be described by

$$\sin^2[\Delta_{\text{AC}}^{\pm 1}(\Omega_+, \Omega_-, \Omega_\pi, \Delta)t] \times e^{-\gamma*\Omega_\mp^2 t/(\Delta\pm\delta_\text{B})^2} e^{-\gamma*\Omega_\pi^2 t/(\Delta_\text{P}-\Delta)^2}, \tag{5.24}$$

where $\Delta_{\text{AC}}^{\pm 1}$ are the differential AC-stark shifts of the Zeeman qubits which are given by

$$\begin{aligned}\Delta_{\text{AC}}^{\pm 1}(\Omega_+, \Omega_-, \Omega_\pi, \Delta) = \Omega_\mp^2 \left(\frac{1}{\Delta \pm \delta_\text{B}} - \frac{1}{\Delta_\text{P} - \Delta \mp \delta_\text{B}} + \frac{1}{\Delta_\text{P} + \Delta_\text{S} - \Delta}\right) + \\ \Omega_\pi^2 \left(-\frac{1}{\Delta_\text{P} - \Delta} + \frac{1}{\Delta_\text{P} + \Delta_\text{S} - \Delta}\right) + \frac{\Omega_\pm^2}{\Delta_\text{P} + \Delta_\text{S} - \Delta}.\end{aligned} \tag{5.25}$$

To measure the Ramsey oscillation, we begin by preparing the ion in its ground state ${}^2S_{1/2}|F = 1, m_F = 0\rangle$ through optical pumping. Subsequently, we apply a Ramsey sequence[68]. To measure the Rabi frequencies of the three components, we execute the Ramsey sequence on all three qubits. The measurement results and fitting outcomes are depicted in Fig. 5.8.

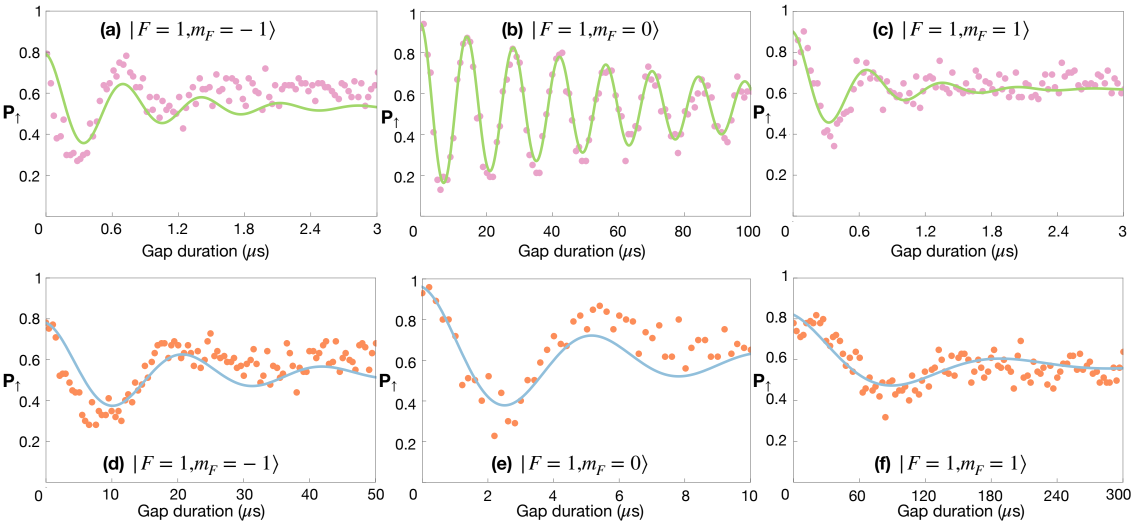

Figure 5.8 Ramsey measurement

Results of the Ramsey measurements (a-c) for the driving beam and (d-f) for the probe beam.

It is worth mentioning that the signal in Fig. 5.8 (b) is utilized to align the direction of the B-field. Once the B-field is aligned parallel to the driving beam, the π component of the driving beam is eliminated, resulting in a reduction of dephasing caused by spontaneous emission.

5.7 Extraction of the phonon number from the sideband transitions

In our experiment, we define the states $|F = 0, m_F = 0\rangle$ and $|F = 1, m_F = 0\rangle$ in the $^2S_{1/2}$ manifold, with an energy difference of ω_0, as the $|\downarrow\rangle$ and $|\uparrow\rangle$ states of the qubit, respectively. To drive the qubit through the Raman transition[75], a pair of 355 nm laser beams, as shown in Fig. 1(c), with a frequency difference of ω_R is employed. As mentioned in the main text, we define $\mu_\mathrm{R} \equiv \omega_\mathrm{R} - \omega_0$ as the detuning of the Raman transition relative to the qubit transition.

When the detuning of the transition, μ_R, matches the frequency of a motional mode, the Hamiltonians $\hat{H}\mathrm{r, m}$ and $\hat{H}\mathrm{b, m}$, representing the cases of $\mu_\mathrm{R} = -\omega_m$ and $\mu_\mathrm{R} = \omega_m$, respectively, can be expressed as:

$$\hat{H}_{\mathrm{r},m} = \hat{a}_m \sqrt{\frac{1}{2M\omega_m}} \sum_j b_j^m \hat{\sigma}_j^+ + \mathrm{h.c.} \tag{5.26}$$

$$\hat{H}_{\mathrm{b},m} = \hat{a}_m^\dagger \sqrt{\frac{1}{2M\omega_m}} \sum_j b_j^m \hat{\sigma}_j^+ + \mathrm{h.c.}, \tag{5.27}$$

where M represents the mass of a single $^{171}\mathrm{Yb}^+$ ion, $\hat{a}_m^\dagger$, $\hat{a}m$, and ωm denote the creation, annihilation operator, and angular frequency of the m-th motional mode, respectively. Furthermore, b_j^m corresponds to the normal mode transformation matrix of the j-th ion with respect to the m-th mode. After the time evolution $\hat{U}_{\mathrm{r(b)},m}(t)$ of the Hamiltonian with an initial state $|{\downarrow\downarrow\downarrow} \cdots {\downarrow}\rangle\, |n\rangle_m$ (where $|n\rangle_m$ is a Fock state of the m-th mode), we obtain the time dependence of the normalized average population in the upstate as follows:

$$P_\uparrow^{\mathrm{r(b)},m}(t, n) = \mathrm{Tr}\left[\left(\sum_j \frac{\hat{\sigma}_j^z + \hat{I}_\mathrm{s}}{2} \otimes \hat{I}_m\right) \rho_{\mathrm{r(b)},m}(t, n)\right] \tag{5.28}$$

where $\hat{I}_\mathrm{s}$ and $\hat{I}_m$ are the identity operators of spins and the m-th mode and $\rho_{\mathrm{r(b)},m}(t, n) = \hat{U}(t)_{\mathrm{r(b)},m}\, |{\downarrow\downarrow\downarrow} \cdots {\downarrow}\rangle \langle {\downarrow\downarrow\downarrow} \cdots {\downarrow}| \otimes |n\rangle_m \langle n|_m\, \hat{U}(t)^\dagger_{\mathrm{r(b)},m}$ is the density matrix after the time evolution of duration t. If we start from a thermal state which is described by the density matrix

$$\rho_{\mathrm{th,m}}(\bar{n}) = \sum_i \frac{\bar{n}^i}{(\bar{n} + 1)^{i+1}}\, |i\rangle_m \langle i|_m\,. \tag{5.29}$$

Instead of simulating the master equation with this density matrix as the initial state, we numerically solve the time evolution starting from a Fock state with different phonon numbers. This allows us to obtain the probabilities of a set $P_{\uparrow}^{\mathrm{r(b)},m}(t,0), P_{\uparrow}^{\mathrm{r(b)},m}(t,1), \cdots P_{\uparrow}^{\mathrm{r(b)},m}(t,n)$. The average upper-state probability after the time evolution from a thermal state can then be calculated by a weighted superposition of each evolution of a Fock state, as shown below the equation.

$$P_{\uparrow}^{\mathrm{r(b)},m}(t) = \mathrm{Tr}\left[\left(\sum_j \frac{\hat{\sigma}_j^z + \hat{I}_\mathrm{s}}{2} \otimes \hat{I}_m\right)\rho_{\mathrm{r(b),th,m}}(t,\bar{n})\right] = \sum_i \frac{\bar{n}^i}{(\bar{n}+1)^{i+1}} P_{\uparrow}^{\mathrm{r(b)},m}(t,i) \tag{5.30}$$

At the π duration of COM mode, we compare the ratio between blue-sideband and red-sideband transition for the m-th mode, $P_{\uparrow}^{\mathrm{r},m}(t)/P_{\uparrow}^{\mathrm{b},m}(t)$ to the Eq. (5.30). Then we deduce the $\bar{n}$ for the m-th mode.

With this method we fit the peaks in Fig.4(b) and estimate the final temperature after the double-EIT cooling. The fitted results are {0.101 (zig-zag mode), 0.0460, 0.0283, 0.0817, 0.0996, 0.0181, 0.0759, 0.0337, 0.0388, 0.0495, 0.0274, 1.04 (COM mode)}.

It is interesting to discuss this method further. For a single ion, we can extract the phonon number by calculating $\frac{P^\mathrm{r}/P^\mathrm{b}}{1-P^\mathrm{r}/P^\mathrm{b}}$[37]. However, this method is not valid when we globally drive the COM mode of the crystal. For example, in a two-ion crystal in the Fock state $|n=2\rangle$, the global red-sideband transition can only pump 50% population of each ion to the up state. Since the Hamiltonian of the red-sideband transition is $\hat{H} = \eta\Omega_0\left[(\hat{\sigma}-^{(1)} + \hat{\sigma}-^{(2)})\hat{a}^\dagger + (\hat{\sigma}+^{(1)} + \hat{\sigma}+^{(2)})\hat{a}\right]$, we can consider the red-sideband transition as an exchange between phonon and spin. Therefore, we can only excite one of the spins by eliminating the phonon. The following figure, Fig. 5.9, provides an intuitive explanation.

Based on this understanding, we can also calculate the mean phonon number of the COM mode for 12 ions by introducing an additional parameter α into the formula $\bar{n} = \frac{\alpha P^\mathrm{r}/P^\mathrm{b}}{1-\alpha P^\mathrm{r}/P^\mathrm{b}}$. Fig. X illustrates the relationship between the ratio $P^\mathrm{r}/P^\mathrm{b}$ and $\bar{n}$, indicating that $\alpha \approx 2.7$ for $\bar{n} < 2$. In our simulation, we consider the sideband transitions of the COM mode with 12 ions, spanning from the initial phonon number up to $|n=10\rangle$ as discussed in Equation (5.30). The Rabi frequency on the carrier transition is $\Omega/(2\pi) = 12$ kHz, and the Lamb-Dicke parameter is $0.11/\sqrt{12}$. The transitions evolve for 206μs to obtain the spectrum. We truncate the Fock space by excluding phonon numbers larger than 22.

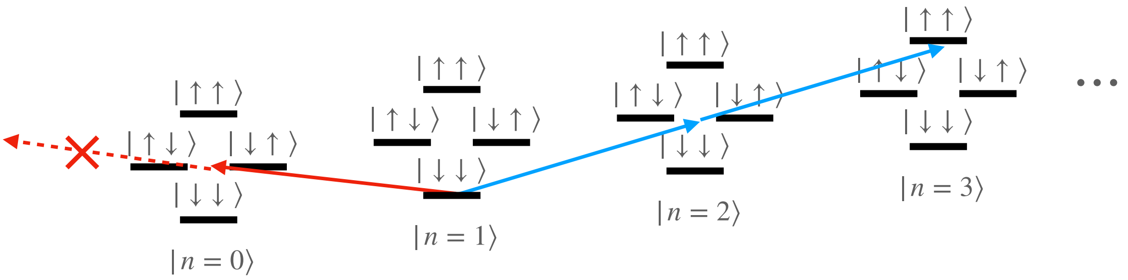

Figure 5.9 Sideband transition

Global red-sideband transition. Here, the red line represents the red-sideband transition, and the blue line represents the blue-sideband transition. Since the Fock state is bounded on $|n=0\rangle$, we can only reach $|\uparrow\downarrow\rangle$ or $|\downarrow\uparrow\rangle$ by globally driving the red-sideband transition of $|\downarrow\downarrow\rangle|n=1\rangle$. On the other hand, we can reach $|\uparrow\uparrow\rangle$ for the global blue-sideband transitions.

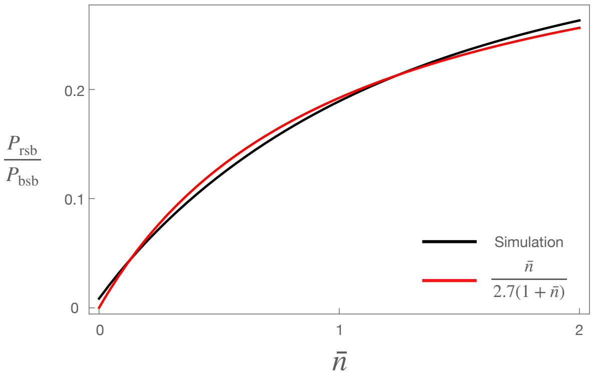

Figure 5.10 Peak fit

Comparison between numerical simulation result and the formula $\frac{P^{\mathrm{r}}}{P^{\mathrm{b}}} = \frac{\bar{n}}{\alpha(1+\bar{n})}$. Red curve represents the formula, and black curve represents the simulation result. Here α is 2.7, and determined by fitting the simulation result.

5.8 Thermometry based on the optical-dipole-force

Fig. 5.11 shows the laser setup for generating the optical-dipole-force(ODF).

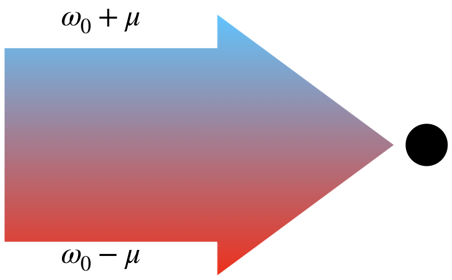

Figure 5.11 Laser setting for the ODF measurement.

For the pair of Raman beam, the effective Hamiltonian can be written as

$$H_I^{(\mathrm{eff})} = \sum_j \frac{\Omega_j}{2} e^{-i\left[\Delta k\cdot r_j(t)-\delta t-\Delta\varphi\right]}\hat{\sigma}_j^{+} + \mathrm{H.c.}, \tag{5.31}$$

where $\delta = \omega_{\mathrm{R}} - \omega_0$, Ω_j and Δk are the Rabi frequency and net wave-vector of Raman laser beams, respectively. If we use two pair of Raman beam to generate two effective coupling simultaneously with opposite detuning μ_{R} for the ODF, the whole Hamiltonian can be written as

$$H_{I,\mathrm{ODF}}^{(\mathrm{eff})} = \sum_j \frac{\Omega_j}{2} e^{-i\left[\Delta k_1\cdot r_j(t)-\mu_{\mathrm{R}}t-\varphi_1\right]}\hat{\sigma}_j^{+} + \frac{\Omega_j}{2} e^{-i\left[\Delta k_2\cdot r_j(t)+\mu_{\mathrm{R}}t-\varphi_2\right]}\hat{\sigma}_j^{+} + \mathrm{H.c.} \tag{5.32}$$

Although we have four transitions and two Raman transitions, we typically use only two laser beams. One laser beam has a single frequency component, while the other laser beam has two frequency components. In this situation, we have $\Delta k_1 = \Delta k_2$. We can rewrite the two phase terms as $\varphi_s = \frac{\varphi_1+\varphi_2}{2}$ and $\varphi_m = \frac{\varphi_1-\varphi_2}{2}$. Consequently, the Hamiltonian can be expressed as follows:

$$H_{I,\mathrm{ODF}}^{(\mathrm{eff})} = \frac{\Omega_j}{2}(\cos(\Delta k\cdot r_j)+i\sin(\Delta k\cdot r_j))\cos(\mu_{\mathrm{R}}t+\varphi_m)(\hat{\sigma}_x^{(j)}\cos\varphi_s-\hat{\sigma}_y^{(j)}\sin\varphi_s). \tag{5.33}$$

In experiment, we calibrate the phase of two different frequency components to be the same, $\varphi_s = \varphi_m = 0$, and the Δk along the y direction. Then we have

$$H_I^{(\mathrm{eff})} = \frac{\Omega_j}{2}\left[\cos(\Delta k\cdot y_j)\cos\mu_{\mathrm{R}}t + i\sin(\Delta k\cdot y_j)\cos\mu_{\mathrm{R}}t\right]\hat{\sigma}_x^{(j)}, \tag{5.34}$$

where the first term gives us the dephasing dependent on the motional state along the x-axis in the Bloch sphere[71]:

$$P_{\uparrow}^{j} = \frac{1}{2}\left[1 - e^{-2\Gamma_{\mathrm{D}}\tau}\exp\left(-2\sum_m \left|\alpha_{jm}\right|^2\left(2\bar{n}_m+1\right)\right)\right], \tag{5.35}$$

where Γ_{D} describes the decoherence in the experiment and

$$\begin{aligned}\alpha_{jm} =& \eta_m\Omega_j\frac{b_{jm}}{\left(\mu_{\mathrm{R}}^2-\omega_m^2\right)}\left(\omega_m(1-\cos\phi)+i\mu_{\mathrm{R}}\sin\phi - e^{i\omega_m\tau}\left\{\omega_m\left[\cos\left(\mu_{\mathrm{R}}\tau\right)-\cos\left(\mu_{\mathrm{R}}\tau+\phi\right)\right]\right.\right.\\ &\left.\left.-i\mu_{\mathrm{R}}\left[\sin\left(\mu_{\mathrm{R}}\tau\right)-\sin\left(\mu_{\mathrm{R}}\tau+\phi\right)\right]\right\}\right),\end{aligned} \tag{5.36}$$

where $\phi = \left(\tau+\tau_\pi\right)\left(\mu_{\mathrm{R}}-\omega_m\right)$, $\eta_m = \Delta k\sqrt{\frac{1}{2M\omega_m}}$ is the Lamb-Dicke parameter of m-th mode, and τ_π is the duration for the π-pulse during the ODF measurement. For the relative long duration of the ODF pulse we have $\phi \approx \tau\left(\mu_{\mathrm{R}} - \omega_m\right)$. When the detuning μ_{R} is near the COM mode, we can approximate the Eq. (5.38) by

$$P_{\uparrow}^{j} = \frac{1}{2}\left[1 - e^{-2\Gamma_{\mathrm{D}}\tau}\exp\left(-2\left|\alpha_j\right|^2(2\bar{n}+1)\right)\right], \tag{5.37}$$

where

$$\begin{aligned}\alpha_j =& \frac{\eta\Omega_j}{\sqrt{N}}\frac{1}{\left(\mu_{\mathrm{R}}^2 - \omega_{\mathrm{COM}}^2\right)}\left(\omega_{\mathrm{COM}}(1-\cos\phi) + i\mu_{\mathrm{R}}\sin\phi - e^{i\omega_{\mathrm{COM}}\tau}\left\{\omega_{\mathrm{COM}}\left[\cos\left(\mu_{\mathrm{R}}\tau\right) - \cos\left(\mu_{\mathrm{R}}\tau+\phi\right)\right]\right.\right.\\ &\left.\left.-i\mu_{\mathrm{R}}\left[\sin\left(\mu_{\mathrm{R}}\tau\right) - \sin\left(\mu_{\mathrm{R}}\tau+\phi\right)\right]\right\}\right),\end{aligned} \tag{5.38}$$

where $\eta = \Delta k\sqrt{\frac{1}{2M\omega_{\mathrm{COM}}}}$ represents the Lamb-Dicke parameter for the COM mode, and N denotes the number of ions. The spectrum resulting from Equation (5.38) with different phonon numbers is depicted in Fig. 5.12(a). The null point corresponds to $\tau\left(\mu_{\mathrm{R}} - \omega_m\right) = 2n\pi$. In the experiment, we individually detect the fluorescence of ions in the crystal to obtain the downstate population and measure the strength of the ODF using the Rabi oscillation of the carrier transition.

To study the cooling dynamics conveniently without acquiring the spectroscopy signal shown in Fig. 5.12(a) at each cooling step, we fix the detuning of the ODF beams at the highest peak of the spectrum indicated by the dashed line in Fig. 5.12(a). In our experiment, this detuning is $(\mu_{\mathrm{R}} - \omega_{\mathrm{COM}})\tau_{\mathrm{ODF}}/(2\pi) = 0.37$, and we record the up-state probability during the cooling process. As demonstrated in Fig. 5.12(a), for the same strength and duration of the ODF beams, a decrease in temperature leads to a reduction in the height of the spectrum.

The relationship between the up-state probability at the selected detuning and the temperature is illustrated in Fig. 5.12(b). By fitting the experimentally measured $P_{\uparrow}$ to the corresponding function, we can quickly determine the temperature of the mode using a method referred to as the ODF height method. To verify the reliability of this method, we compare its results with those obtained from the blue-sideband measurement for the heating of a single ion. Firstly, we measure the heating rate of a single ion using both the blue-sideband method and the ODF height method. The comparison of their results, 0.83 (±0.19) ms^{-1} for the blue-sideband method and 0.77 (±0.15) ms^{-1} for the ODF method, demonstrates consistency within the error bars, as shown in Fig. 5.12(c). Subsequently, we apply the ODF height method to measure the heating rate for the COM mode

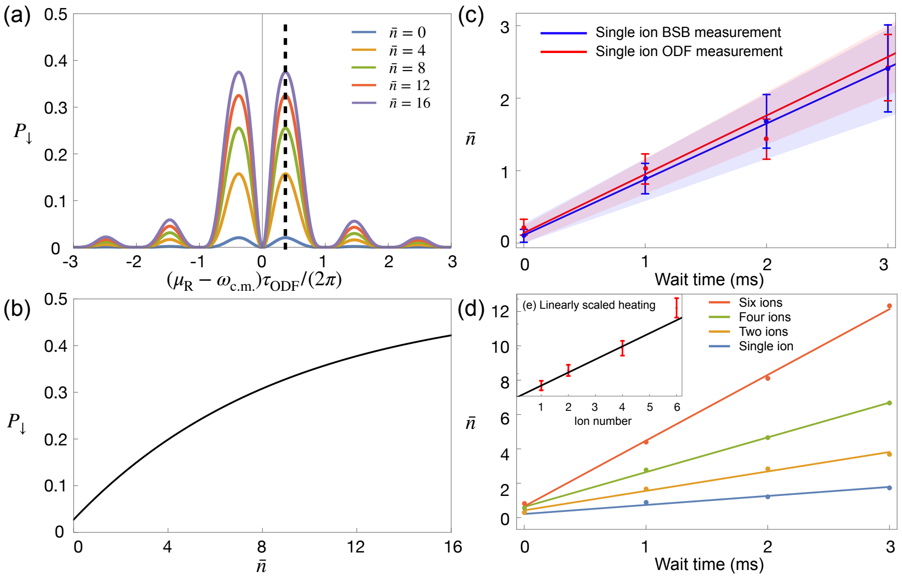

Figure 5.12 ODF spectrum

ODF spectrum and the heating measurement. (a) The ODF spectrum of average up-state population with different phonon number for the COM mode. The dashed black line indicates the chosen detuning to measure the average phonon number. (b) The relation between the average phonon number and the average downstate population at the detuning of ODF pulse indicated in (a). Here the blue (red) area represents error bars for the heating rate measured by sideband (ODF) method. (c) Comparison of the results of heating measurements between blue-sideband (blue line) and ODF height method (red line). (d) The heating measurement of multiple ions by the ODF height method. The measured heating rates are 0.77 ± 0.19 quanta/ms (sideband method) and 0.83 ± 0.15 quanta/ms (ODF method). (e) Linearly scaled heating rate. In this figure, the black line denotes $n \cdot \gamma_{\text{heating}}$, where n is the number of ions and γ_{heating} is the heating rate of a single ion.

of 2D crystals consisting of 1, 2, 4, and 6 ions. As depicted in Figures 5.12(d) and 5.12(e), the heating rate for the COM mode increases linearly with the number of ions as expected, amounting to 0.61 (±0.08) ms^{-1} per ion. For an ion trapped by electric fields, the heating rate can be calculated using the formula proposed by[76].

$$\dot{\bar{n}} = \frac{e^2}{4m\hbar\omega} S_E(\omega) \tag{5.39}$$

where, $\dot{\bar{n}}$ represents the heating rate, ω is the mode frequency, Ω_T is the frequency of the rf field, m denotes the mass of the ion, e is the elementary charge, and $S_E(\omega) \equiv 2\int_{-\infty}^{\infty} d\tau e^{i\omega\tau}\langle E(t)E(t+\tau)\rangle$ represents the spectral density of electric-field fluctuations. In the case of the COM mode of a large crystal with N ions, it can be approximated as a single ion with mass Nm and charge Ne. Consequently, the coefficient $e^2/(4m\hbar\omega)$ will increase by a factor of N, indicating a linear dependence on the number of ions.

However, for other modes of a large ion crystal, the above argument requires some modifications. The Hamiltonian in the presence of uniform electric noise is given by:

$$H(t) = \sum_i \hbar\omega_i a_i^\dagger a_i + eE(t)\sum_i x_i$$

The ion's position operator can be decomposed into the normal coordinates $x_i = b_{ij}u_j$ and the normal coordinates $u_i = \sqrt{\frac{\hbar}{2m\omega_i}}(a_i + a_i^\dagger)$. Then the Hamiltonian can be simplified to

$$H(t) = \sum_i \left[\hbar\omega_i a_i^\dagger a_i + u_i eE(t)\sum_j b_{ji}\right]$$

Based on the first-order perturbation theory[76], the heating rate on the i-th mode is

$$\dot{\bar{n}}_i = \frac{e^2}{4m\hbar\omega_i}2\left(\sum_j b_{ji}\right)^2 \int_{-\infty}^{\infty} d\tau e^{i\omega_i\tau}\langle E(t)E(t+\tau)\rangle = \left(\sum_j b_{ji}\right)^2 \dot{\bar{n}}_{\text{single}}$$

Once again, for the COM mode, the heating rate of a large ion crystal will increase by a factor of $(\sum_{i=1}^{N}\frac{1}{\sqrt{N}})^2 = N$. The linear relationship between the heating rate and the number of ions confirms the reliability of the ODF height measurement. We utilize this method to investigate the cooling dynamics in crystals with different numbers of ions. Fig. 5.13 illustrates the cooling dynamics for the 2D crystal with varying numbers of ions using the ODF height method. It should be noted that the trapping conditions remain the same as those for the 12-ion crystal. The transverse mode's trap frequency is nearly two times lower than that for cooling a single ion, resulting in a higher cooling limit of $\bar{n} = 0.34 \pm 0.25$. For the twelve ions, we average the experimental results over the time interval of 390μs to 500μs, obtaining a mean phonon number of 1.04 ± 0.61. The experimental data for the single-ion crystal, twelve-ion crystal, and two-, four-, six-ion crystals were obtained under different experimental conditions, mainly varying the overall laser power of the Doppler and EIT cooling beams. This discrepancy beyond statistical errors introduces inconsistency between the datasets. Nonetheless, we can confidently conclude that there is no significant speed-up observed in EIT cooling due to many-body interactions.

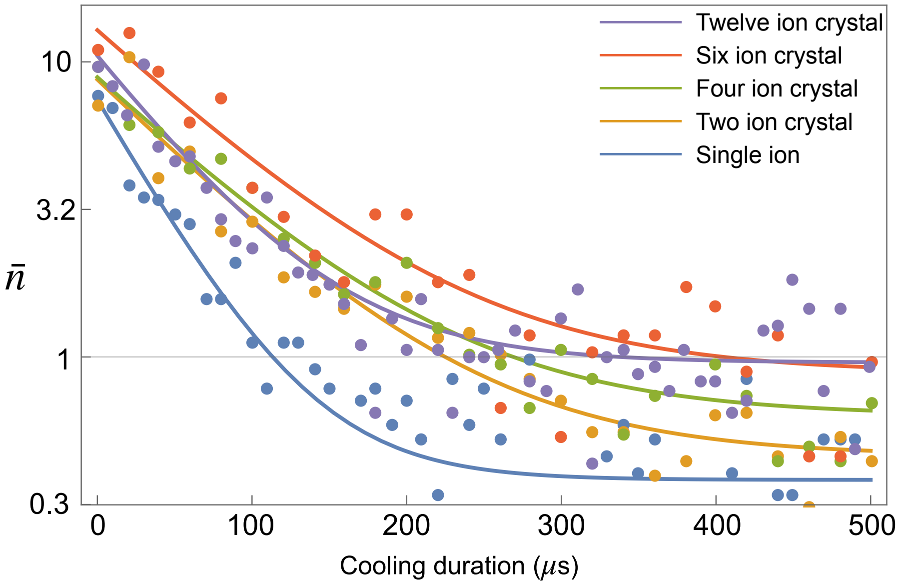

Figure 5.13 ODF cooling
Multi-ion crystal cooling measurement by the ODF height method for 2, 4, 6 and 12 ions.

CHAPTER 6 QUANTUM SIMULATION WITH 2D ION CRYSTALS

Realizing a controllable quantum system that can be described by a quantum spin model is central to the development of quantum simulation and quantum computation in various experimental platforms[77-82]. Quantum spin models provide simplified Hamiltonians to understand exotic phenomena in quantum magnetic materials, including geometric spin frustration[77-80], topological or spin-liquid phases[83-84], and topological phase transitions[85], primarily arising in two or higher dimensions. In general, solving two-dimensional (2D) Ising models with transverse fields is challenging[81]. Furthermore, if the model is frustrated by competing interactions, mean-field theory fails to explain the exotic features, and the quantum Monte Carlo method cannot be applied due to the sign problem. Interactions in the spin model are classified into ferromagnetic and anti-ferromagnetic types, which, together with the lattice geometry, determine the properties of magnetic materials. Such Ising models can also encode combinatorial optimization problems, such as maximum independent sets, which fall under NP-hard problems. To fully map such problems[82], it is necessary to arbitrarily adjust the type, strength, and connectivity of the interactions. Thus, an ideal quantum simulator for quantum spin models, surpassing classical computational capabilities, should enable control over the sign, strength, and connectivity of spin-spin interactions. Furthermore, the solution can be obtained through site-resolving detection after coherently preparing the ground state of the encoded Hamiltonian. Therefore, a desirable quantum simulator for quantum spin models, exceeding classical computational capabilities, should encompass the control of sign, strength, and connectivity of spin-spin interactions, as well as coherent manipulation and individual detection.

Recently, various physical platforms have been developed for quantum simulators with 2D geometries. Superconducting annealers[86] have demonstrated the realization of 2D spin ices; however, limited coherence prevents the probing of quantum properties. Neutral atoms in 2D optical tweezers have simulated large-scale quantum magnets[87-88]; however, generating ferromagnetic or arbitrary range interactions using Rydberg blockade interactions is challenging[89].

Trapped atomic ions, as a leading platform for quantum simulation, exhibit excep-

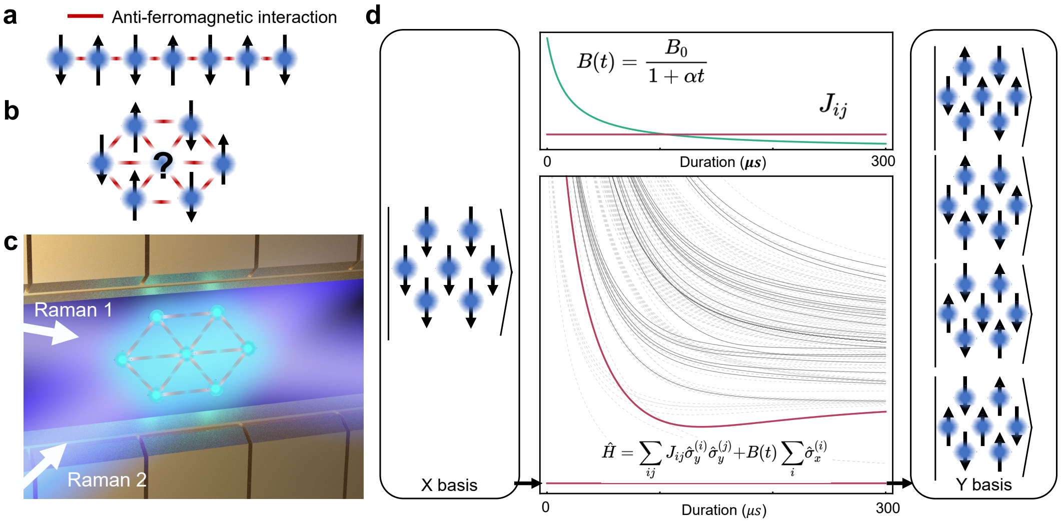

Figure 6.1 Quantum simulation of frustrated quantum magnets with a 2D ion crystal. **a** One-dimensional (1D) antiferromagnetic quantum magnets exhibit Néel-like ground states, illustrated here with an example of seven spins. **b** Two-dimensional (2D) antiferromagnetic quantum magnets display geometric frustration in the ground state. **c** Atomic ions are trapped using a monolithic trap and controlled by globally illustrated Raman lasers. **d** Systematic diagram of adiabatic quantum simulation for the case of geometrically frustrated 2D spins. The experiment starts from the ground state of the transverse magnetic field, $B\sum_i \sigma_x^{(i)}$, and adiabatically evolves into the ground state of the Ising Hamiltonian, $\sum_{i,j} J_{i,j}\sigma_y^{(i)}\sigma_y^{(j)}$, as depicted in Fig. **b**. In the energy-level diagram, the vertical axis represents the energy difference from the ground state. Solid lines represent excited states coupled to the ground state, while dashed lines represent other excited states. The red lines correspond to the ground state and the lowest excited energy level coupled to the ground state. The energy level is scaled with the spin-spin interaction, J_0. We ramp down the strength of the transverse magnetic field using a profile of $1/(1+\alpha t)$, where α is a tuning parameter, while the spin-spin interaction remains constant during the ramping process. Ultimately, the system reaches the ground state of the frustrated magnet, which is a superposition of four degenerate states due to competing interactions.

tional coherence times[38,90] and can realize both ferromagnetic and antiferromagnetic interactions[91-94]. However, previous studies on simulating quantum spin models were limited to 1D ion chains, making it difficult to directly simulate 2D spin models[95-96].

There have been decades of efforts to extend the dimension of trapped-ion simulators while retaining the advantages of 1D chains[50,97-101]. Controllable spin-spin interactions have been demonstrated using fast-rotating 2D ion crystals in a Penning trap[100,102]. However, the simulation of quantum spin models and site-resolved detection in the Penning trap have not yet been realized. Stationary 2D ion crystals can be achieved in Paul traps, but they are susceptible to micromotion synchronized with the RF field, which compromises the quality of quantum simulations. Traps without excess micromotion can be constructed in arrays of micro Paul traps[103-105]. Alternatively, it has been proposed that the detrimental effects of micromotion on quantum simulation can be mitigated by using an oblate Paul trap[50,101]. Similarly, we have developed a monolithic trap that suppresses the influence of micromotion by aligning the net propagation direction of the operating lasers perpendicular to the micromotion[106].

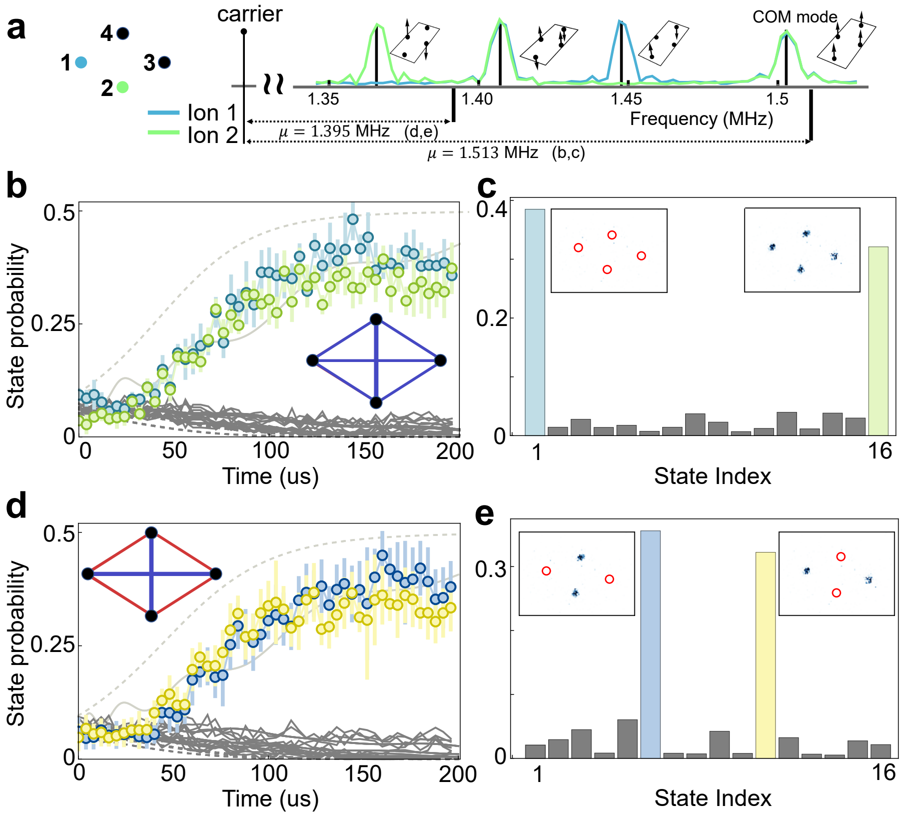

Figure 6.2 Verification of quantum simulation with 2D crystal with four ions. **a**, Vibrational spectrum of the four-ion 2D crystal. The blue and green curves come from fluorescence of blue and green ions, respectively, where the mode frequencies are indicated by the black lines. **b**,**d** depict the time evolution of different Ising models at the detunings of Raman laser beams shown in **a**. Insets present the interaction diagrams, where the red and blue lines represent the anti-ferromagnetic and ferromagnetic interactions, respectively. The filled circles, solid curves, and dashed curves represent the experimental data, theoretical evolution expected from the actual ramp, and populations in the exact ground state, respectively. **c**,**e**, depict the experimentally measured populations of the state in binary order at the end of the ramp, which indicates the ground states of the Hamiltonians with the corresponding interaction diagrams. Insets represent reconstructed images based on the binary detection of spin states. **b**,**c** are for the all-to-all ferromagnetic interaction. **d**,**e** are for the nearest anti-ferromagnetic interaction and next-nearest ferromagnetic interaction. The error bars represent standard deviation.

For the first time, we have successfully simulated quantum Ising models using 2D ion crystals confined in a monolithic Paul trap. Our quantum simulation involves generating various Ising interactions with different signs and strengths, and preparing and observing their ground states through adiabatic evolution and site-resolving detection, as summarized in Fig. 6.1. In our experiment, we utilize $^{171}\mathrm{Yb}^{+}$ ions in the monolithic Paul trap to realize the spin models. The states $|F=1,m=0\rangle$ and $|F=0,m=0\rangle$ in the $S_{1/2}$

manifold, with an energy splitting of $\omega_{\mathrm{HF}} = 12.642\,812\,\mathrm{GHz}$, represent the $|\uparrow\rangle$ and $|\downarrow\rangle$ states of a spin-1/2 system. As shown in Fig. 6.1(c), a 2D ion crystal is confined in the monolithic Paul trap[106], where spin-spin interactions are mediated by collective phonon modes through Raman excitations. The trap's electrodes are designed to rotate the crystal plane along the direction of micromotion, thereby mitigating the detrimental effect of micromotion on quantum simulation. This is achieved by ensuring that the net propagation vector of the Raman laser beams is perpendicular to the plane of the crystal.

By coupling ions to Raman laser beams, we realize the Hamiltonian of the transverse field Ising model,

$$\hat{H} = \sum_{i,j} J_{i,j}\hat{\sigma}_y^{(i)}\hat{\sigma}_y^{(j)} + B(t)\sum_i \hat{\sigma}_x^{(i)}, \tag{6.1}$$

where J_{ij} represents the interaction strength between the i-th and the j-th spins, and $B(t)$ represents the strength of the transverse B-field. We generate the transverse B-field using Raman laser beams with a frequency difference of ω_{HF}. To generate the spin-spin interactions, we use bichromatic Raman beams with frequency differences of $\omega_{\mathrm{HF}} \pm (\nu - \delta)$. The effective Ising interaction is expressed as[107-109]:

$$J_{ij} = \Omega_i\Omega_j \frac{\hbar(\delta k)^2}{2M}\sum_m \frac{b_{i,m}b_{j,m}}{\mu^2 - \omega_m^2} \tag{6.2}$$

where M is the mass of the $^{171}\mathrm{Yb}^+$ ion, Ω_i is the laser Rabi frequency on i-th ion, δk is the net-propagation vector of the Raman beams, $b_{i,m}$ is the normal mode vector, ω_m is the m-th mode frequency, and μ is the Raman detuning from the ω_{HF}. As shown in Eq. (6.2), the spin-spin couplings J_{ij} can be engineered by adjusting the Raman detuning μ. If the detuning μ is close to a certain vibrational mode, the characteristics of the spin-spin couplings reflect the vibrational mode vector[91]. We can further engineer J_{ij} to any types of spin models by applying multiple detunings together[110-111]. It has been shown that in the limit $\mu \gg \omega_{\mathrm{com}}$, the strength of J_{ij} decays with inter-ion distance r as r^{-3} and in the limit $\mu \approx \omega_{\mathrm{com}}$, it scales as r^0[100,112]. We note that as illustrated in Fig. 6.1a,b, the different dimension and geometry of spins results in fundamentally different spin models though the scale of the spin-spin coupling depending on the distance is similar.

Our protocol of adiabatic quantum simulation is shown in Fig. 6.1d[91,94]. In experiment, we perform ground state cooling of vibrational modes before starting the adiabatic quantum simulation, which consists of Doppler cooling, EIT cooling[113-114], and five cycles of sideband cooling. Then, we initialize all spins to the $|\downarrow\rangle$ state using the standard optical pumping technique[115]. The adiabatic quantum simulation begins with a global $\pi/2$ pulse, which simultaneously rotates the spins into the eigenstate of the transverse $\boldsymbol{B}$-field. The strength of the $\boldsymbol{B}$-field is chosen to be sufficiently strong to dominate over the Ising interactions. As shown in Fig. 6.1(d), we gradually decrease the strength of the $\boldsymbol{B}$-field while keeping the Ising interaction strength constant. To achieve this, we employ a ramping profile of $1/(1+\alpha t)$, inspired by local adiabatic evolution[116], where the speed of the ramping is proportional to the instantaneous energy gap. This specific ramping profile allows us to prepare the ground state with a much shorter duration compared to exponential ramping profiles[91,93]. Finally, we perform individual spin state measurements of the final spin configuration using standard site-resolved fluorescence detection[117] with an electron-multiplying charge coupled device (EMCCD) camera.

6.1 Engineering of interaction diagram

First, we verify the feasibility of quantum simulation in a 2D-ion crystal using a simple example of a four-ion crystal arranged in a rhombus geometry. In Fig. 6.2(a), we display the vibrational spectrum of the crystal and the Raman detunings used to generate different spin-spin interactions. Fig. 6.2(b) shows the time evolution of four spins with ferromagnetic interactions, while Fig. 6.2(c) presents the dominant populations in the expected ground states $|\uparrow\uparrow\uparrow\uparrow\rangle$ and $|\downarrow\downarrow\downarrow\downarrow\rangle$ with a probability of 73.34%. We effectively generate ferromagnetic interactions for each ion pair by setting the detuning $\mu = \omega_{\mathrm{com}} + (2\pi)10$ kHz, resulting in an average $J_{ij} = 2$ kHz. The $\boldsymbol{B}$-field is initially set at 29 kHz and ramped down to 2 kHz in 200 μs using a time constant $\alpha = 0.06$, which maximizes the probability of ground states and is consistent with other experiments in the paper (see Method). It is worth noting that we effectively reverse the sign of the Hamiltonian by preparing the highest excited states[91]. Fig. 6.2(d) and (e) illustrate the time evolution and ground states of the Ising model with nearest anti-ferromagnetic and next-nearest ferromagnetic interactions, respectively. We generate these interactions using the red side of the third mode shown in Fig. 6.2(a). The expected ground state, a superposition of alternating N'eel spin orders, is prepared with a probability of 64.97%. While the experimental data for time evolution shown in Fig. 6.2(b) and (d) deviate from the exact ground states, they are in agreement with the expected time evolution. This deviation is primarily caused by a faster ramping speed employed, which is larger than what a perfect adiabatic condition requires, mainly due to the large heating rates of the COM mode.

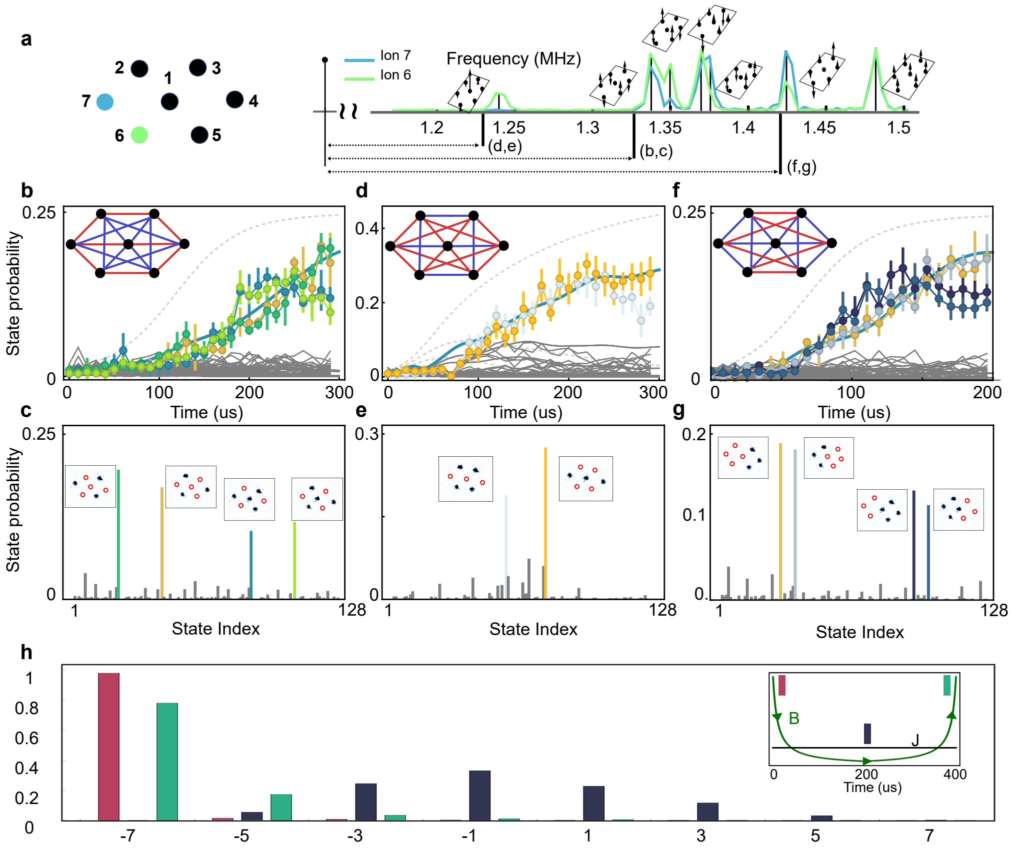

Figure 6.3 Quantum simulation and quantum coherence of various spin models with seven-ion 2D crystal.

a, Vibrational spectrum of the crystal. The red and green curves represent the fluorescence of red and green ions, respectively. The vertical red lines indicate the mode frequencies, while the solid line represents the detuning used in the experiment. **b**,**d**,**f** depict the time evolution of different Ising interactions, which are tuned by detunings of the Raman laser beams shown in **a**. The insets represent the interaction diagrams. The points, solid curves, and dashed curves represent the experimental data, theoretical evolution expected from the actual ramp, and the populations in the exact ground state, respectively. **c**,**e**,**g** depict the experimentally measured populations of all states in binary order at the end of the ramp, which presents the ground states of the Hamiltonians with the given interaction diagrams. Insets depict reconstructed images based on the binary detection of spin states. **b**,**c**, is performed with a detuning of 1.328 MHz; **d**,**e** is performed with a detuning of 1.231 MHz; **f**,**g** is performed with a detuning of 1.416 MHz to the left of the 7th vibrational mode from the COM mode. The error bars represent standard deviation. **h,** Quantum coherence probed by time reversal of adiabatic evolution. Population distributions of each spin-x component in the initial state (red), at the end of adiabatic evolution (black), and after the reversal of adiabatic evolution (green). The initial state is recovered after reversal with fidelity of 80% which strongly indicates the quantum coherence in the simulation. The inset presents the ramping trajectory corresponding to the transverse B field (green curve) and the averaged Ising couplings (black curve). The experimental conditions are the same as in **b**,**c**.

Next, we increase the number of ions to seven in a centered-hexagonal crystal, as shown in Fig. 6.3(a), which displays the geometrical configuration and vibrational mode spectrum. We benchmark the seven-ion 2D crystal with three different types of Ising models, where the strengths and signs of the spin-spin interactions are engineered by tuning the detuning of the bichromatic Raman laser beams, as illustrated in Fig. 6.3(a). In the first case, with a detuning of 1.328 MHz (red side of the 6th vibrational mode), the outer spins exhibit anti-ferromagnetic nearest-neighbor interaction and ferromagnetic next-nearest-neighbor interaction, while the center spin experiences four ferromagnetic interactions and two anti-ferromagnetic interactions, as depicted in Fig. 6.3(b). The average strength of J_{ij} is 566 Hz, and the B-field is changed from 29 kHz to 1.5 kHz in 300 μs. This interaction diagram exhibits a similar frustration as in Fig. 6.1(b), where the outer spins show an alternating order, and the center spin experiences competing interactions between the $|\uparrow\rangle$ and $|\downarrow\rangle$ spins. Thus, the ground state for this interaction diagram contains a superposition of $|\uparrow\rangle$ and $|\downarrow\rangle$ states for the center spin. Including the equal superpositions of different alternating orders of the outer ions, there are four different spin configurations in the ground state. We observe the ground state after the adiabatic evolution. Fig. 6.3(b) compares experimental and theoretical results during the adiabatic evolution. Consistent with theoretical expectations, the four spin configurations are dominantly populated with a probability of 58.5% at the end of the evolution, as shown in Fig. 6.3(c), clearly indicating the presence of frustrated spin states of the Hamiltonian.

In the second case, illustrated in Fig. 6.3(d) and (e), with a detuning of 1.231 MHz, the crystal splits into two sub-lattices: one consisting of spins 1-4-7 and the other consisting of spins 2-3-5-6. The average strength of J_{ij} is 849 Hz, and the B-field is changed from 29 kHz to 1.5 kHz in 300 μs. Within each sub-lattice, the interactions are ferromagnetic, while the interactions between different sub-lattices are anti-ferromagnetic. This interaction diagram does not exhibit frustration, and the resulting ground state consists of the same spins within each sub-lattice and opposite spins between the two sub-lattices. As shown in Fig. 6.3(d) and (e), the ground state comprises two configurations with a probability of 46.3%. In these ground states, one of the sub-lattices has all spins down, while the other has all spins up, which is in agreement with theoretical expectations.

In the third case, at the detuning of 1.416 MHz, the crystal experiences frustration from different types of interactions, as shown in Fig. 6.3(f) and (g). The crystal can be divided into three parts: a left sub-lattice with spins 2-6-7, a right sub-lattice with spins 3-4-5, and the center spin. The average strength of J_{ij} is 917 Hz, and the B-field is changed from 29 kHz to 1.5 kHz in 300 μs. Within each sub-lattice, the spins have ferromagnetic interactions, while spins between different sub-lattices interact antiferromagnetically. If

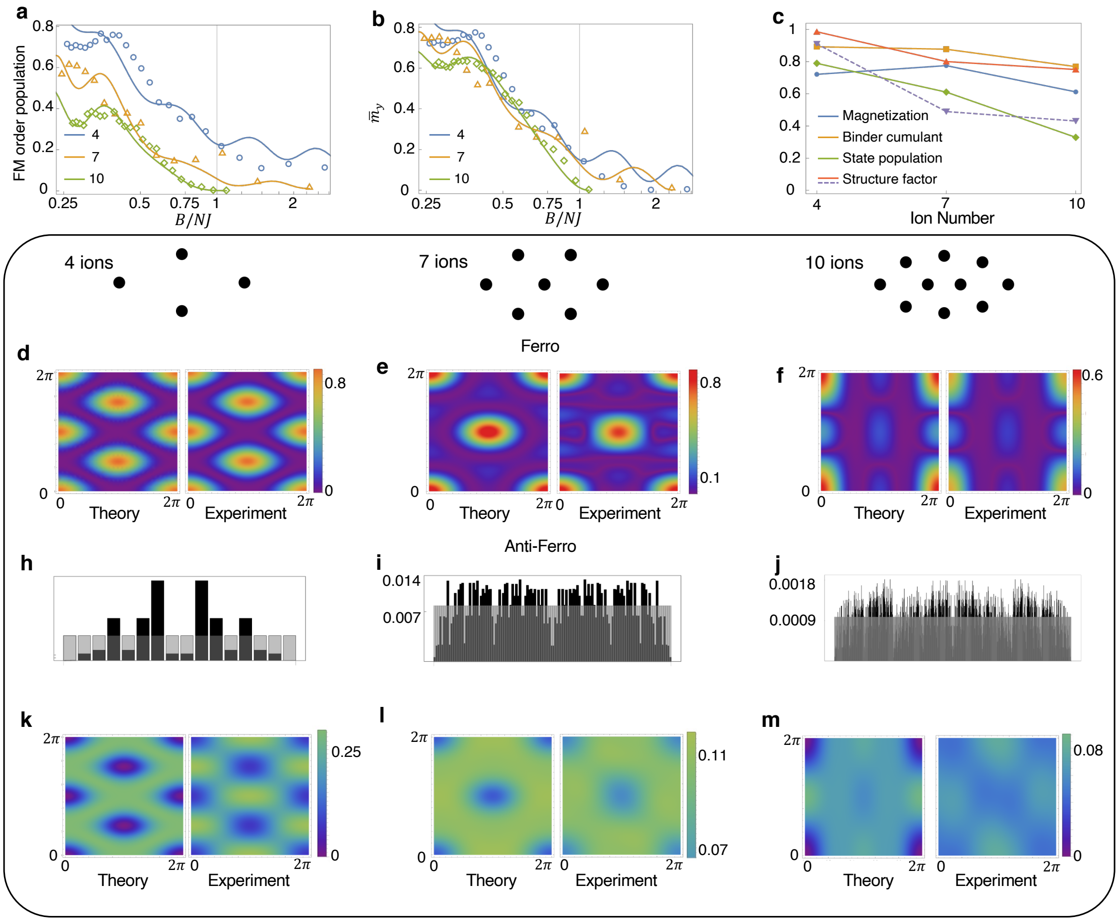

Figure 6.4 Benchmarking of quantum simulation with increasing number of spins in 2D ion crystal.

a, b show the population of ferromagnetic (FM) order and scaled magnetization $\bar{m}$ depending on B/NJ, respectively, for four, seven, and ten ions, which are obtained from the experimental ramping down of transverse field. As the strength of the magnetic field decreases, the spins experience a crossover from a paramagnetic phase to a ferromagnetic phase. The solid lines represent theoretical curves obtained by numerical simulation given ramping profiles, where scaling factors are used to capture the decay induced by decoherence. **c**, Population of FM order, scaled magnetization, scaled Binder cumulant and scaled structure factor at the end of the experimental ramping profiles on the number of spins. **d,h,k**, for four ions, **e,i,l**, for seven ions, **f,j,m**, for ten ions, with the corresponding geometries of crystals shown above **d,e,f**. **d,e,f**, show both theoretical and experimental structure factors at the end of the experimental ramping profiles for long-range ferromagnetic interactions. The experimental values at (0,0) are used for **c**, which are scaled with theoretical values. **h,i,j**, show the theoretical state population after adiabatic evolution for a long-range anti-ferromagnetic interaction. The black bars represent the final state population, and the gray bars represent the population of a paramagnetic state. **k,l,m**, show the structure factors after adiabatic evolution for a long-range anti-ferromagnetic (AFM) interaction. The experimental values at $(\pi, 0)$ are used for **c**, which are scaled with theoretical values.

there were no center spin, the spins in the left sub-lattice would have the same orientation, and the spins in the right sub-lattice would have the opposite orientation without frustration. However, frustration arises from the ferromagnetic interactions between the center spin and all the other spins. Due to the competing interactions on the center spin, the ground state becomes degenerate with four-spin configurations, as shown in Fig. 6.3(f) and (g). The adiabatic evolution prepares the ground state with a probability of 61.45%.

To probe the coherence of the adiabatic evolution, we apply a verification scheme using the time-reversed analog simulation, which can sensitively detect incoherent noise[93,118]. The basic experimental protocol involves performing adiabatic evolution by ramping down the $\boldsymbol{B}$-field and then reversing the adiabatic evolution by ramping it back up. Fig. 6.3(h) shows the measured distribution of the x-component of the total spin operator $\hat{S}_x = \sum_i \hat{\sigma} x^{(i)}$. Initially, 90% of the population is prepared in the state $|Sx = -7/2\rangle$. The total magnetization at the end of the adiabatic evolution is approximately zero since the spins are aligned along the y-direction, which is the direction of the spin-spin interaction. After the time-reversal ramping, 80% of the population returns to the initial state $|S_x = -7/2\rangle$, indicating the coherence of the process. Here, the experimental conditions are the same as those in Fig. 6.3(b) and (c), where the ground state is frustrated. We note that the time-reversal analog verification protocol is insensitive to shot-to-shot parameter fluctuations, parameter miscalibration, and crosstalk[118], which have insignificant effects on the adiabatic quantum simulation[118].

We evaluate the performance of quantum simulation with the 2D crystal using different numbers of ions. When the Raman detuning is close to the COM mode frequency, all spin-spin interactions can be either ferromagnetic or antiferromagnetic. For four, seven, and ten ions, we set the Raman detuning to be 10, 12, and 30 kHz larger than the COM mode frequency, respectively, and generate a long-range antiferromagnetic interaction $\boldsymbol{J}_{ij} \propto 1/r_{ij}^{\gamma}$[100], where $\gamma = 0.24, 0.27, 0.57$ correspondingly. Initially, we start from the highest excited state of the transverse $\boldsymbol{B}$-field, which generates effective ferromagnetic interactions, and use them to benchmark the performance of the 2D ion crystals. In Fig. 6.4(a), we use the population of the ferromagnetic order, and in Fig. 6.4(b), we use the scaled magnetization[92] as order parameters to investigate the crossover from the paramagnetic phase to the ferromagnetic phase as the number of spins increases for four, seven, and ten ions.

In Fig. 6.4(c), we introduce four different order parameters: the population of the ferromagnetic order, magnetization, Binder cumulant[92], and structure factor (see also Methods). The state populations of the ferromagnetic order at the end of the quantum simulation decay faster as the number of spins increases. This behavior may arise from the heating of the COM vibrational mode (see Methods). However, other order parameters such as scaled magnetization and Binder cumulant are not significantly affected by the number of spins. The structure factors shown in Figs.6.4(d), (e), and (f) confirm that the prepared states at the end of the simulation closely resemble the ideal ground states of the long-range ferromagnetic Ising models. The experimental values in Figs.6.4(d), (e), and (f), compared to the theoretical ones, are depicted in Fig. 6.4(c), revealing a similar dependence on the magnetization and Binder cumulant with respect to the number of spins.

By starting from the ground state of the transverse field, we perform quantum simulation with long-range AFM interaction. The ground state of a long-range AFM model in a triangular lattice is typically frustrated and exhibits a large degeneracy[77], as shown in Figs.6.4(h), (i), and (j). Due to the extensive degeneracy of the ground states, it becomes challenging to use magnetization and Binder cumulant as order parameters to assess the reliability of the experiments. Instead, we compare the measured state populations to those from time evolution simulations using the population distribution distance. In our quantum simulation, the Bhattacharyya distance of the final ground states is 89%, 92%, and 30% for four, seven, and ten ions, respectively. We note that distinguishing frustrated phases from paramagnetic phases is difficult. To probe the emergence of the frustrated phase, we utilize structure factors, which clearly distinguish the frustrated phase from the uniform structure factor of the paramagnetic phase. The ideal structure factors and the experimentally measured structure factors shown in Fig. 6.4(h), (i), and (j) are consistent with each other. In Fig. 6.4(c), the experimental values at $(\pi, 0)$ scaled with the theoretical ones do not exhibit significant degradation as the number of ions increases.

The frustrated ground states can be related to solutions of optimization problems with challenging instances. It has been extensively discussed that adiabatic quantum simulation may not find the exact solution to the optimization problem due to the exponentially closing minimum energy gap at the end of the evolution. However, adiabatic quantum simulation can provide approximate solutions that are significantly better than classical computation[119]. We consider states with an approximation ratio larger than 95%, which corresponds to 5% of the minimum energy level, as belonging to the optimization solutions. In the experiment, we find that 56%, 52%, and 16% of our measured states are approximate solutions for four, seven, and ten ions, respectively.

In our experiment, imperfections mainly arise from errors during the preparation of the initial states, heating of the vibrational modes, and non-adiabatic transitions (see Methods). The imperfections from initial state preparation are below 5% for the ten-ion crystal and can be further improved by using Raman laser beams with larger beam widths. The influence of heating may be limited in precisely preparing ground states as the number of ions increases, especially when the COM mode is involved in the quantum simulation. This limitation can be addressed by utilizing modes other than the COM mode or by enclosing the trap at cryogenic temperatures, which can significantly reduce heating rates[120]. With lower heating, adiabatic evolution can be performed for longer durations, thereby further suppressing non-adiabatic transitions.

This work presents an experimental demonstration of quantum simulation using 2D-ion crystals. The 2D-ion crystal showcases the ability to engineer the signs and strengths of spin-spin interactions and perform coherent quantum evolution with site-resolving detection, making it an ideal platform for simulating Ising models. The 2D-ion crystal is particularly well-suited for addressing classically intractable problems, such as combinatorial optimization problems. The general mapping of optimization problems to Ising models requires all-to-all connectivity, which naturally arises in the 2D-ion crystal[121]. Without such connectivity, the mapping would require an overhead of the order of N^2 spins[121-122]. In comparison to 1D-ion chains, the 2D-ion crystal offers improved connectivity. The spin-spin interactions typically decay as a power law $1/d^\gamma$ with the distance d between ions[100]. For an N-ion system, the largest distance between ions scales as $1/\sqrt{N}$ in 2D, whereas it scales as $1/N$ in 1D. It is worth noting that arbitrary programmable interactions can be realized through modulation of laser pulses[110,123-124].

Our experimental demonstration can also be extended to the study of 2D quantum spin systems with controllable polynomial-decaying interactions[125-129]. By scaling up the system, we can explore the properties of ground states in frustrated Hamiltonians with large degeneracy[77], utilizing appropriate order parameters like the structure factor that are insensitive to microscopic details of the states. This platform holds promise for investigating the dynamics of quantum materials, topological phase transitions[85], and thermalization of 2D systems[130]. We anticipate that the 2D-ion crystal will emerge as a powerful tool for solving classically intractable problems and as a fertile ground for exploring exotic phenomena in 2D quantum systems.

6.2 Trap conditions

To generate 2D ion crystal, we squeeze crystal along y-direction by setting the voltage of electrodes $V_0 = V_1$, $V_2 = V_3 = V_4 = V_5$, and with ratio of $V_0/V_2 = 1/5.41$. The ratio of voltages is calculated based on numerical simulation given the trap geometry[106].

For 4-ion and 10-ion experiment, the trap frequencies are $\{\omega_x, \omega_y, \omega_z\} = \{0.626, 0.404, 1.503\}$ MHz. For 7-ion experiment, the trap frequencies are $\{\omega_x, \omega_y, \omega_z\} = \{0.486, 0.407, 1.482\}$ MHz. The axes of the trap frequencies are shown in Fig. 1. The 2D crystal is in the xy plane, where the x-axis is confined by RF power and the y-axis is controlled by DC-voltage[106]. The trap frequencies are the same for 4-ion and 10-ion cases, but for 7-ion case the trap frequencies along the x- and y-direction are closer. With 7 ions, we release the confinement along x-direction to make a hexagonal geometry that 6 ions form a hexagon and 1 ion locates at the center of the hexagon. If we use the setting of the 4-ion case with 7 ions, ions will form a shape of a ladder as shown in Fig S1, which is different from the centered hexagonal geometry. For 4-ion and 10-ion cases, we increase the z-direction trap frequency as high as possible to reduce heating from environment noise meanwhile maintain crystal are 2D and inter-ion distance is around 5 μm.

Figure 6.5 Trap geometry.
Here black texts represent voltage labels on the front side of the trap, and white texts represent voltage labels on the back side electrodes. The GND electrodes are connected to the ground.

6.3 Compensation of micromotion

Different from the 1D ion chain, the excess micromotion[131] of the 2D ion crystal cannot be perfectly compensated. Micromotion refers to the synchronous motion of ions with the oscillating RF field, which degrades precise control over the ions. In a Paul trap, a line exists where the RF field is zero, allowing us to overlap the chain of ions and minimize the effects of micromotion. However, this is not possible for 2D ion crystals since there is no plane in which the RF electric field strength is zero.

Although perfect micromotion compensation is impossible, we can still eliminate the effects of micromotion on quantum operations. When the 2D ion crystal is formed in a plane with only an in-plane electric field, the micromotion exists only within the plane. Therefore, we minimize the effects of micromotion on the Raman laser beams by aligning the plane of the 2D ion crystal with the plane containing only the in-plane electric field and ensuring that the net propagation vector of the Raman beams is perpendicular to the plane. In our case, the trap electrode geometry includes three symmetric planes: the x-y plane, the y-z plane, and the z-x plane. The RF field also exhibits mirror symmetry in relation to these planes, guaranteeing that within each of the three planes, the electric field has only in-plane components. By rotating the principal axis of the electric field[106], we align the crystal with the x-y plane.

In the experiment, we align the plane of the 2D-ion crystal with that of an in-plane electric field through the following three steps: single ion positioning, linear chain formation, and 2D crystal recovery. Firstly, we bring a single ion to the RF null position using the traditional method[131]. Secondly, we determine the required electric voltages for the 2D ion crystal and then increase the RF power to transform the 2D crystal into a linear chain, ensuring its overlap with the RF null line. The mismatch between the ion chain and the null line of the RF field can be detected by observing the strengths of micromotion sideband transitions of individual ions. By simultaneously adjusting the voltages $\Delta V_2 = -\Delta V_3 = \Delta V_4 = -\Delta V_5$, as shown in Fig. 6.5, we minimize the mismatch. Finally, we reduce the power of the RF field to restore the 2D ion crystal. After completing the first two steps, we only need to rotate the plane of the 2D ion crystal around the null line. By simultaneously adjusting the voltages of electrodes $\Delta V_0 = \Delta V_1$, we minimize the micromotion sidebands of individual ions. Fig. 6.6 illustrates the strengths of micromotion sidebands for 16 individual ions in the 2D-ion crystal after minimizing their magnitudes. On average, the strengths of the micromotion sidebands are approximately 200 times smaller than those of the carrier transitions.

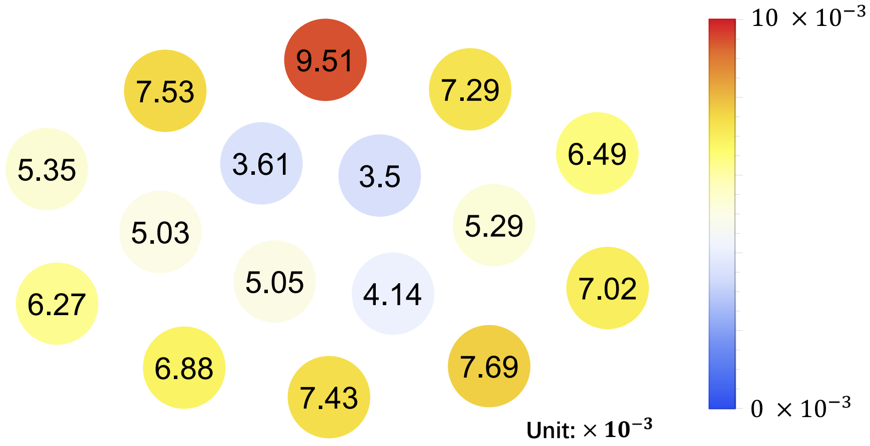

Figure 6.6 The relative strengths of micromotion sidebands with respect to those of carrier transitions for 16 ions.

6.4 Detection of multi-ion states

To detect the multi-ion states, we spatially resolve the photons emitted by ions during the application of a detection laser. The 2D crystals are imaged using an objective lens positioned perpendicular to the crystals, and we utilize an electron-multiplying charge-coupled device (EMCCD) camera (Andor iXon 897) for photon detection. To enhance the signal-to-noise ratio, we fit the distribution of photon counts across pixels using a Gaussian function and extract the fitted amplitude as the effective photon count for single-shot measurements.

In experiment, we use a 1.0 ms detection pulse, and we collect 34.7 photons on PMT with a 0.37 NA objective lens for the bright state of a single ion. In our case, the average detection fidelities for a 4-ion, 7-ion, and 10-ion 2D crystal are 98.2%, 97.8%, and 98.0%.

6.5 Generating transverse-field Ising interaction

We generate the Ising interaction by globally driving the ions with two pulsed laser beams at a wavelength of 355 nm. These beams have beatnote frequencies $\nu_{\text{Qubit}} \pm \mu$, which induce a spin-dependent dipole force (SDF). The wavevector difference $\Delta k = 2\pi\sqrt{2}/\lambda$ is aligned along the transverse direction of the 2D ion crystal. By varying the beatnote frequencies near different modes, similar to the linear chain[94,112], we can engineer the interaction diagram.

The transverse magnetic field (B field) is effectively generated by addressing Raman transitions that are resonant with the hyperfine splitting, which corresponds to the carrier transition. The phase of the Raman beams determines the direction of the B field on the Bloch sphere. Since the SDF has a phase difference of $\pi/2$ with respect to the laser field, we use the same laser phase for both the carrier transition and the SDF to ensure that the direction of the transverse B field is perpendicular to the direction of the SDF.

The Hamiltonian of a single ion interacting with the laser field can be expressed as follows:

$$\begin{aligned}\hat{H} = \sum_{i,j,k} \Omega_i \Big\{ \hat{\sigma}_+^{(j)} \left[\hat{I} - i\eta_k (\hat{a}_k e^{-i\nu_k t} + \hat{a}_k^\dagger e^{i\nu_k t}) \right] e^{-i\omega_i t + i\phi_i} \\ + \hat{\sigma}_-^{(j)} \left[\hat{I} + i\eta_k (\hat{a}_k e^{-i\nu_k t} + \hat{a}_k^\dagger e^{i\nu_k t}) \right] e^{i\omega_i t - i\phi_i} \Big\},\end{aligned}$$

, where only the first-order of Lamb-Dicke parameter are reserved. For carrier transition, we drive only one transition, and the Raman detuning matches the hyperfine splitting of qubit. the Hamiltonian reduce to

$$\hat{H} = \sum_j \Omega_0 \left(\hat{\sigma}_+^{(j)} e^{i\phi} + \hat{\sigma}_-^{(j)} e^{-i\phi} \right) = \sum_j \Omega_0 \hat{\sigma}_\phi^{(j)}, \tag{6.3}$$

which is a spin rotation along ϕ-axis. ϕ is the phase of laser field, and Ω_0 is the Rabi frequency which represents laser field strength.

For SDF, we use beatnote Raman beams, and the Hamiltonian becomes

$$\begin{aligned}\hat{H} &= \sum_{j,k} \Omega_0 \Big[-i\eta_k \hat{\sigma}_+^{(j)} e^{i\phi} (\hat{a}_k e^{-i(\nu_k-\omega)t} + \hat{a}_k^\dagger e^{i(\nu_k-\omega)t}) \\ &+ i\eta_k \hat{\sigma}_-^{(j)} e^{-i\phi} (\hat{a}_k e^{-i(\nu_k-\omega)t} + \hat{a}_k^\dagger e^{i(\nu_k-\omega)t}) \Big] \\ &= \sum_{j,k} \eta_k \Omega_0 (\hat{a}_k e^{-i(\nu_k-\omega)t} + \hat{a}_k^\dagger e^{i(\nu_k-\omega)t}) \\ &\times \left[\hat{\sigma}_+^{(j)} e^{i(\phi-\pi/2)} + \hat{\sigma}_-^{(j)} e^{-i(\phi-\pi/2)} \right],\end{aligned}$$

where the last term in the above equation is a spin operator along $\phi - \pi/2$ direction, and the Hamiltonian can be written as

$$\hat{H} = \sum_{j,k} \eta_k \Omega_0 (\hat{a}_k e^{-i(\nu_k-\omega)t} + \hat{a}_k^\dagger e^{i(\nu_k-\omega)t}) \hat{\sigma}_{\phi-\pi/2}^{(j)}. \tag{6.4}$$

By comparing Eq. (6.3) and Eq. (6.4), we can conclude that driving the SDF and the carrier transition naturally results in a phase difference of $-\pi/2$ when the laser fields have the same phase.

To investigate the ferromagnetic order and the antiferromagnetic order, we utilize different order parameters such as scaled magnetization, scaled Binder cumulant, and structure factor.

The scaled magnetization is defined as

$$\bar{m}_y = (m^0_{y,N} - m_y)/(m^0_{y,N} - 1)$$

, where $m_y = \sum_{n=0}^{N} C^n_N |N - 2n| P(n)$, and $m^9_{y,N} = \frac{1}{N2^N} \sum_{n=0}^{N} C^n_N |N - 2n|$.

The scaled Binder cumulant is defined as

$$\bar{g} = \frac{g^0_N - g}{g^0_N - 1}$$

, where $g^0_N = 3 - 2/N$, and $g = \frac{\sum_{n=0}^{N}(N-2n)^4 P(n)}{(\sum_{n=0}^{N}(N-2n)^2 P(n))^2}$

The structure factor is defined as

$$\mathcal{S}(\mathbf{q}) = \frac{1}{N} \sum_{i,j} e^{-i\mathbf{q}\cdot\mathbf{r}_{ij}} C^Z_{ij}$$

, where $C^Z_{ij} = \left\langle \hat{\sigma}^{(i)}_z \hat{\sigma}^{(j)}_z \right\rangle - \left\langle \hat{\sigma}^{(i)}_z \right\rangle \left\langle \hat{\sigma}^{(j)}_z \right\rangle$ is the spin correlator between i-th and j-th ions.

6.6 Experimental methods of finding optimal Ising interactions

Experimentally, we perform a scan of the detuning of the spin-dependent dipole force (SDF) while keeping the duration of the adiabatic evolution fixed. We identify the detuning value that yields the maximum ground population after the adiabatic evolution. Specifically, we choose a detuning of 10 kHz based on the mode that exhibits the highest population among all up and down states. Since the detuning of the SDF determines the strength of the Ising interactions, this detuning scan enables us to assess the performance of the adiabatic evolution by measuring the ground state population after the adiabatic evolution. The maximum ground-state population signifies an optimal Ising interaction achieved through adiabatic passage of the transverse field, with fixed initial and final strengths of the transverse field and a fixed duration.

6.7 Error Budget

6.7.1 Imperfection of initial state preparations

Due to the constrained ion-electrode distance, we employ Raman beams with a diameter of 25 µm. However, as we increased the power and beam size of the Raman beam, we encountered a significant charging effect. The relatively narrow width of the Raman beams introduces non-uniform Rabi frequencies across the ions, resulting in errors in the global $\pi/2$ rotation. The dependence of individual Rabi frequencies on the total number of ions is illustrated in Fig. 6.7.

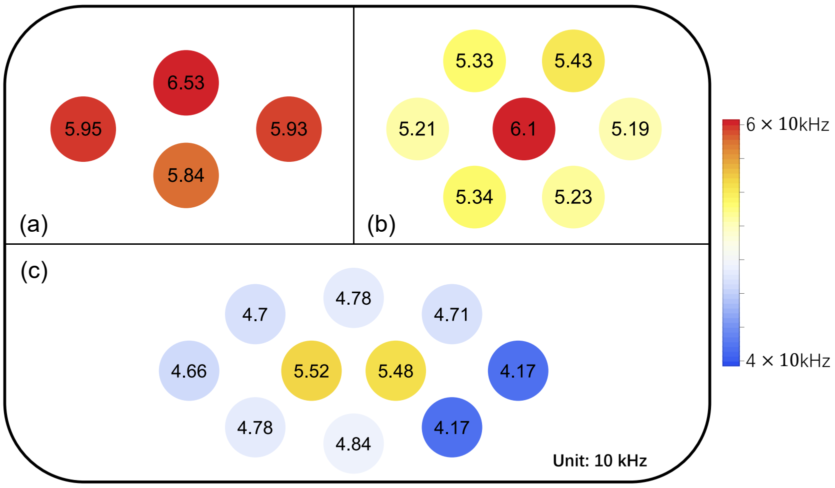

Figure 6.7 Rabi frequencies (in the unit of 10 kHz) of ions for the 2D crystal. (a) 4, (b) 7, and (c) 10 ions. The deeper color indicates higher Rabi frequency.

The non-uniform Rabi frequencies introduce imperfections in initial state preparation. Given experimentally measured Rabi frequencies, we theoretically estimate the fidelities of initial states for 4-ion, 7-ion, and 10-ion crystals as 99.5%, 98.7%, and 95.2%, respectively. In the experiment, we estimate the fidelities by using Bhattacharyya distances[132] between the measured and ideal populations of initial states, which is equal to state fidelity in our case. For 4, 7, and 10-ion crystals, Bhattacharyya distances are $99.2 \pm 0.7\%$, $96.3 \pm 0.6\%$, and $83\% \pm 2\%$ respectively, which are consistent to those of theoretical estimations except 10-ion case. The large deviation for 10-ion crystal mainly comes from the insufficient number of measurements for the multi-ion states. Therefore, we use the product of all Bhattacharyya distances of single-ion distribution, which should be also same to the state fidelities for our initial states. The formula is written as

$$\prod_{i=1}^{N}\left(\sqrt{\frac{1}{2}}\sqrt{p_{i,1}}+\sqrt{\frac{1}{2}}\sqrt{1-p_{i,1}}\right),$$

where $p_{i,1}$ is the upper state population of the i-th ion, and N is the number of ion. For 4, 7-ion, and 10-ion crystals, the experimentally measured Bhattacharyya distances of single-ion distribution are $99.7\% \pm 0.2\%$, and $99.6\% \pm 0.7\%$, and $95\% \pm 5\%$, respectively.

Errors from heating of the center of mass modes

We investigate the impact of center of mass modes heating through numerical simulations, specifically using four ions. We employ a detuning of Raman beams of 10 kHz, which induces all-to-all ferromagnetic interaction, as depicted in Fig. 2(b) of the main text.

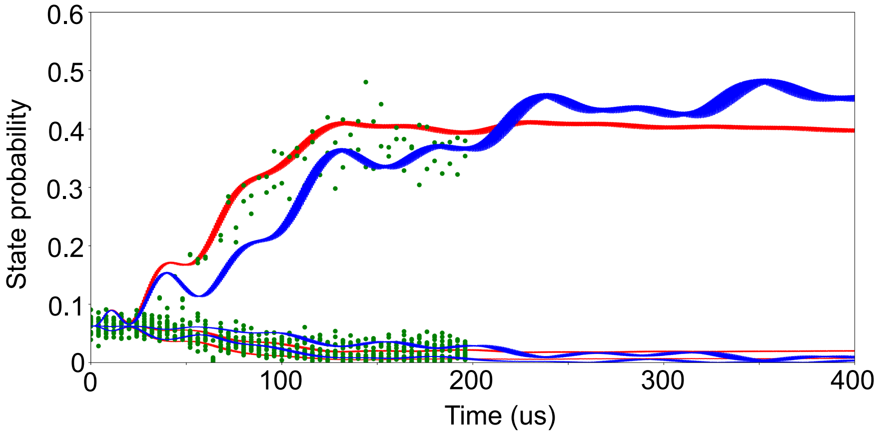

Figure 6.8 Effect of vibrational heating. The final ground states are the ferromagnetic states $|\uparrow\uparrow\uparrow\uparrow\rangle$ and $|\downarrow\downarrow\downarrow\downarrow\rangle$. The blue curves represent adiabatic evolution without heating, while the red curves represent adiabatic evolution with heating of 3200 quanta/s. The green dots represent the experimental results. When heating is applied, the adiabatic evolution leads to a lower population of the ground state compared to the adiabatic evolution without heating. We extend the simulation duration to 400 μs, which clearly reveals the limitations of heating.

n our experiment, the heating rate of a single ion in the center of mass mode is approximately 800 quanta/s[113-114], and this rate increases linearly with the number of ions. As for the other modes, it is well-known that their heating rates are significantly smaller compared to the center of mass mode[113-114]. To assess the imperfections in the final ground state resulting from heating in the center of mass mode, we employ numerical simulations.

To account for heating, we introduce two Lindblad operators, $\alpha\hat{a}^\dagger$ and $\alpha\hat{a}$, into the master equation.

$$\frac{d\hat{\rho}}{dt} = -\frac{i}{\hbar}[\hat{H}, \hat{\rho}] + \mathcal{L}(\alpha\hat{a}) + \mathcal{L}(\alpha\hat{a}^\dagger), \tag{6.5}$$

where $\mathcal{L}(A) = \hat{A}\hat{\rho}\hat{A}^\dagger - \frac{1}{2}\hat{A}^\dagger\hat{A}\hat{\rho} - \frac{1}{2}\hat{\rho}\hat{A}^\dagger\hat{A}$.

To get the value of α consistent with experiment, we can first let $\hat{H} = \hbar\hat{a}^\dagger\hat{a}$ and $\hat{\rho} = \sum_{n=0}^{\infty} c_n |n\rangle\langle n|$. We can get a system of differential equations

$$\begin{cases} \dot{c}_n = \alpha^2\left[(n+1)c_{n+1} - (2n+1)c_n + nc_{n-1}\right], & \text{for } n > 0 \\ \dot{c}_0 = \alpha^2(c_1 - c_0) \end{cases} \tag{6.6}$$

Substituting Eq.(4) into the time derivative of average phonon number $\dot{\bar{n}} = \sum_{n=0}^{\infty} n\dot{c}_n$, we can get

$$\dot{\bar{n}} = \alpha^2 \rightarrow \bar{n} = n_0 + \alpha^2 t, \tag{6.7}$$

which indicates a linearly increasing average phonon number. Eq.(6.7) shows that the value of α is related to the time unit used in simulation. In simulation, we use μs as time unit, and expect the average phonon number increase 0.8 quanta after 1000 μs evolution. Since $\Delta\bar{n} = \dot{\bar{n}}\Delta t$, we can calculate the value of α should be 0.028 for a heating rate of 8×10^{-4} quanta/μs.

In simulation of adiabatic evolution, we use a Hamiltonian with one mode and several spins.

$$\hat{H} = \sum_i \Omega_i \sigma_x^{(i)} (\hat{a} e^{-i\nu t} + \hat{a}^\dagger e^{i\nu t}) \tag{6.8}$$

Our numerical simulations demonstrate that heating has a detrimental effect on the population of the ground state during adiabatic evolution. In the absence of heating, at the optimized detuning, the adiabatic evolution is estimated to result in a population of 96% in the ferromagnetic states. However, when considering a heating rate of 3200 quanta/s on the center-of-mass mode (for four ions), the population of ferromagnetic states decreases to 80%. This reduction can account for the experimental result of 73% ± 5%, as illustrated in Fig. 6.8. Additional discrepancies may arise from other experimental imperfections, such as vibrational mode dephasing, laser intensity fluctuations, and so on.

To further investigate the impact of heating on the quality of adiabatic evolution, we conduct numerical simulations of a two-ion crystal under various heating rates.

6.8 Approximate solutions to optimization problems

The minimum energy state can be regarded as the solution to an optimization problem that can be mapped to a spin-model Hamiltonian. Instead of obtaining exact solutions to the optimization problem, we employ our quantum simulator to obtain approximate solutions. We specifically focus on solutions with an approximation ratio r greater than 95%. The approximation ratio $r(s)$ is defined as:

$r(s) = \frac{E_\mathrm{h} - E(s)}{E_\mathrm{h} - E_\mathrm{g}}$,

where $E(s)$ represents the energy of state s, E_h corresponds to the energy of the highest excited states, and E_g represents the energy of the ground states.

Fig. 6.9 depicts the energy level spectrum corresponding to different state configurations in the experiment. The solutions with an approximation ratio greater than 95% are indicated by red data points.

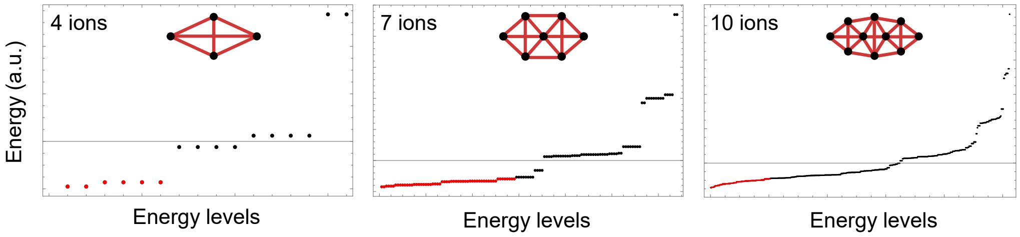

Figure 6.9 Energy level spectrum for 4, 7, and 10 ions crystal. The red points represent the solutions with an approximation ratio larger than 95%.

CHAPTER 7 CION: A PYTHON-BASED MIDDLEWARE

7.1 Current architecture

Cion is a Python-based middleware used for controlling trapped-ion systems. While there are already several controlling ecosystems available, such as ARTIQ, that provide both software and hardware for trapped-ion experiments, relying solely on the hardware components within these ecosystems is insufficient for conducting experiments in real-world scenarios. There may be a need to replace certain components, such as an arbitrary waveform generator, with a more cost-effective alternative. Similarly, individual direct digital synthesizers (DDS) might need to be replaced with integrated versions, and there may even be a requirement to update the field-programmable gate array (FPGA) to enable on-chip arithmetic operations or waveform generation. Additionally, in urgent experimental situations, there may be a need to procure products with short delivery times, which may not be readily available within the ecosystem.

As quantum hardware developers, it is necessary to continuously upgrade the classical hardware to meet the evolving demands of experiments. In contrast to the dynamic nature of classical hardware, the software component remains relatively fixed. Every experiment requires the definition of sequences for ion loading, SPAM (state preparation and measurement) error measurement, Raman operations, and high-level circuit execution. We believe that a middleware is essential to support these unified requirements across a variety of underlying classical hardware platforms.

The architecture of Cion comprises four layers. The first layer is the experiment layer, which contains all the necessary information for conducting experiments. It can be viewed as a central hub that organizes the flow of information. When initiating an experiment, the first step is to create an experiment layer, followed by activating the hardware components.

```
ion_number = 1
exp        = Experiment(ion_number=ion_number)
```

Listing 7.1 Define an experiment layer

The experiment layer has the capability to dynamically adjust its internal functions based on the desired number of ions to be used. Additionally, it automatically generates a folder to store all the data generated during subsequent experiments.

Building upon the experiment layer, we can create a sequence layer where a collec-

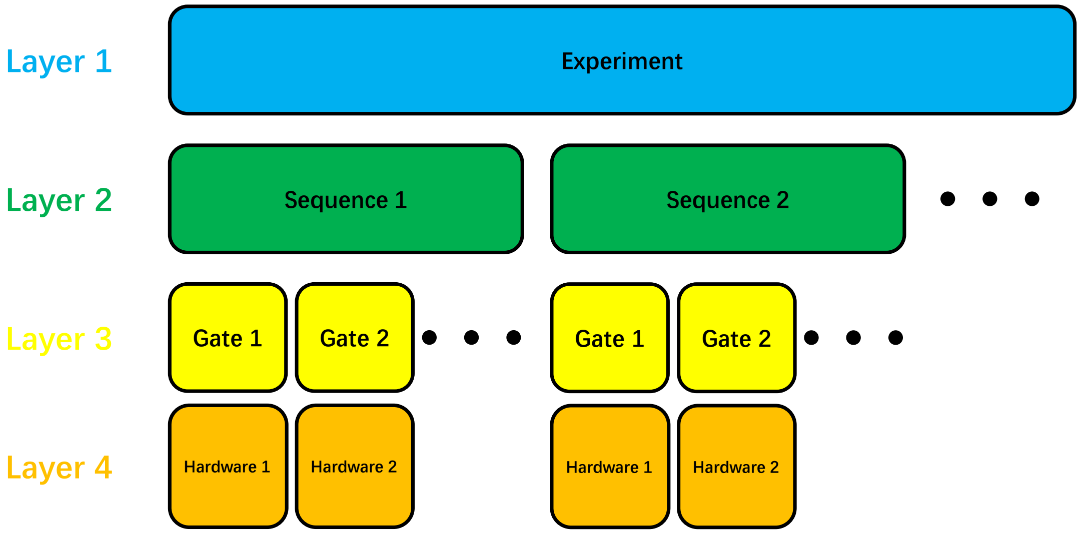

Figure 7.1 Architecture of cion
The four layers of cion. The first layer is experiment layer. The second layer is sequence layer. The third layer is gate layer. And the fourth layer is hardware layer.

tion of sequences can be defined. In atomic, molecular, and optical (AMO) experiments, sequences are established to perform specific operations. For instance, when loading ions, a common approach is to utilize a Doppler sequence, in which the Doppler cooling beam and ionization beam are continuously active.

```
1 doppler_cooling = exp.new_sequence()
2 doppler_cooling.set_sequence(
3     Zero(1).on(all),
4     Doppler_Only(1000, label='Doppler').on(all),
5     Zero(1).on(all))
```

Listing 7.2 Define a Doppler cooling sequence

Listing 7.2 demonstrates a method to define a Doppler cooling sequence. In Line 1, a new sequence is created from the experiment layer and named ”doppler_cooling”. The content of the sequence is defined in Lines 2 to 5, where a 1000 μs Doppler cooling beam is activated for all ions, with 1 μs waiting periods before and after the cooling. The gates ”Zero” and ”Doppler_Only” are further explained later, and the ”.on” method of gates determines the ions affected by the gate.

```
detection_time = 60
pumping_time   = 30
Micro_pitime   = 10
MRamsey        = exp.new_sequence()
MRamsey.set_sequence(
    Doppler(1000).on(all),
    Pumping(pumping_time).on(all),
    Microwave(Micro_pitime/2).on(all),
```

```
    Zero(1,label="Wait").on(all),
    Microwave(Micro_pitime/2).on(all),
    Detection(detection_time).on(all),
    Zero(1).on(all))
```

Listing 7.3 Define a Doppler cooling sequence

Listing 7.3 presents an example of a Ramsey measurement. In comparison to Listing 7.2, the Ramsey sequence employs the gate ”Doppler” instead of ”Doppler_Only” because in the ”Doppler” gate, photon collection is not necessary.

Within the sequence layer, we can define multiple sequences using a similar approach to accomplish our experimental objectives. This layer serves as the primary interface for user interactions and each sequence comprises fundamental elements from the gate layer. The gate layer encompasses three types of essential information.

- Bit string: used to define when the gate is running which signal should be turned on
- Waveform: the amplitude, frequency, phase or an arbitrary waveform of the pulse used inside a gate
- Hardware: used to specify if we want to update the waveform of a gate where we should send the data to.

The bit string is stored inside a variable called dictionary,

```
Exp_chapter_dict = {
    'Doppler':'00000000 00000000 00000000',
    'Doppler_Only':'00000000 00000000 00001111,[10000000 00000000 00000000, 1],[10000000 00000000 00010000,1]',
    'Pumping':  '01100000 11000000 00000000',
    'Detection':'01010000 10000000 00001111,[11000000 00000000 00000000, 1],[11000000 00000000 00010000,1]',
    'Microwave':  '11000000 10100000 00000000',
    'Raman':  '11000000 10010000 00000000',
    'Rx':  '11000000 10010000 00000000',
    'Zero': '11000000 10000000 00000000',
    'Strong': '11111111 11111111 11111111'
          }
```

Listing 7.4 Define a Doppler cooling sequence

Listing 7.4 provides an example of a dictionary used in experiments. In our current sequencer[133], to instruct the FPGA to start collecting photomultiplier tube (PMT) counts, the last four bits of the bit string are set to 1. Conversely, to stop collecting, the fifth-to-last bit is set to 1, as indicated by the bit strings ”Doppler_Only” and ”Detection”. These strings serve as labels to establish connections with the corresponding gates. Within the gate definition, the same label is used. When executing a user-defined sequence, Cion generates a list of bit strings with their respective durations.

The other fundamental information is waveform. In the current version of Cion, two types of pulses are utilized. The first type does not require phase coherence, such as Doppler cooling, pumping, and detection. The hardware and waveform for these pulses can be fully independent. The second type, on the other hand, necessitates phase coherence, such as single qubit rotations and entangling gates. For these pulses, the hardware must be synchronized. Looking at individual pulses, their waveforms can be defined independently of other pulses. These waveforms can take the form of simple sine functions or composite functions with multiple frequency components and time-varying amplitudes. We store these waveforms directly within the gates, but we store the formulas rather than the actual data. When running a specific sequence, Cion automatically combines these formulas with continuous durations, ensuring phase coherence of the pulses, and calculates the data points to be sent to the arbitrary waveform generator (AWG).

```
class Doppler(BaseGate):
    def __init__(self, duration, latency = 0, awg_flag = None, amp = None, freq = None, phase = None, label = "Doppler"):
        super().__init__(duration, latency, awg_flag, 'Doppler', amp, freq, phase, label)

    def update_hardware(self):
        #print("Update Doppler with ", "amp:", self.amp, "freq:", self.freq, "duration: ", self.duration,str(time()))
        labbrick_370_lock_EOM.freq_update(self.freq)

    def reset_hardware(self):
    labbrick_370_lock_EOM.freq_update(165)
```

Listing 7.5 Define a Doppler gate

Listing 7.5 provides an example of gate definition. The definition inherits from the BaseGate class, which is defined in the source code of Cion. Within the Doppler gate definition, there are certain parameters that are not crucial to define, such as the latency that specifies whether the beam needs to wait after it is called. However, it is essential to define the label used for connecting with the dictionary and the hardware responsible for updating the parameters of the Doppler beam. Two methods related to the hardware are present: one for parameter updates and the other for resetting the hardware parameters to their original values. This hardware component also falls under layer 4.

The hardware layer is not explicitly defined within Cion but rather exists in a separate code space that is invoked by Cion. For example, in Listing 7.5, ”labbrick_370_lock_EOM” represents a hardware component used for signal generation. Its definition is not included in the source code of Cion but resides in another Python file that is imported by the file where the Doppler gate is defined. If there is a desire to switch to a different type of hardware, it can be easily achieved by replacing ”lab-brick_370_lock_EOM” with a function compatible with the new hardware.

For gates involving amplitude modulation, frequency modulation, and phase modulation, it is necessary to define piecewise waveforms. In Cion, piecewise waveforms are facilitated through the AdvancedGate class. Listing 7.6 illustrates how to define a piecewise waveform for an AdvancedGate. As creating a piecewise waveform for multiple ions can be complex, we utilize a parameter table to define it and subsequently transfer it to the gate using the ”set_parameter_table()” method.

```
dict0 = {
  'ion_number' : 3,
  'segment_number' : 3,
  'time_intervals' : [(0,17.33),(17.33, 45.66),(45.66, 87.99)],
  'data_per_ion' : {
    #first ion's parameter
    0 : {
      'amp': [(0.45,0.45), (0.42,0.42),(0.23,0.23)],
      'freq': [(4+2.03,4-2.03),(4+2.03,4-2.03),(4+2.03,4-2.03)],
      'phase': [(0.48,-0.48),(0.308,-0.308),(0.086,-0.086)]
    },
    #second ion's parameter
    1 : {
      'amp': [(0.42,0.42),(0.23,0.23),(0.45,0.45,0.10)],
      'freq': [(4+2.03,4-2.03),(4+2.03,4-2.03),(4+2.03,4-2.03,2.03)],
      'phase': [(0.308,-0.308),(0.086,-0.086),(-0.086,0.086,0.086)]
    },
    #third ion's parameter
    2 : {
      'amp': [(0.45,0.45), (0.42,0.42),(0.23,0.23)],
      'freq': [(4+2.03,4-2.03),(4+2.03,4-2.03),(4+2.03,4-2.03)],
      'phase': [(0.308,-0.308),(0.086,-0.086),(-0.086,0.086)]
    }
  }

}

MSGate().set_parameter_table(dict0)
two_qubit_gate = exp.new_sequence()
two_qubit_gate.set_seuqnce(
  Doppler(1000).on(all),
  Pumping(10).on(all),
  MSGate(87.99).on([0,2]),
  Raman(5/2, amp=0.4, freq=car, phase=phi).on([0,2]),
  Detection(60).on(all)
)
```

Listing 7.6 Define a piecewise waveform

7.2 Future update

While our goal is for Cion to be a middleware that users can deploy on their own systems as easily as Kubernetes, currently, if one intends to deploy Cion on hardware with vastly different FPGA communication protocols and arbitrary waveform generators, a bridge must be established between the output of Cion and the input of the hardware. Certain sequencers support our current format of placing bit strings into a list, but there are also more advanced sequencers with high-level programming features that the current version of Cion cannot fully leverage. On-chip arithmetic operations typically serve real-time feedback purposes, which the current version of Cion does not support. Additionally, Cion is primarily designed for trapped ion systems that employ individual addressing, where tightly focused beams can be selectively turned on and off. This individual addressing technology is Markovian, meaning the waveform for entangling a particular pair of ions remains the same. However, there are non-Markovian addressing technologies, such as QCCD[134], where the waveform for entangling a specific pair of ions depends on previous operations. QCCD achieves qubit addressing by moving ions together, and the ions' positions are dependent on previous movements, resulting in non-Markovian operations. The current version of Cion has not yet accounted for these non-Markovian operations. Presently, when executing a sequence, Cion directly generates the data points. However, there are several technologies, such as RFSoC or real-time controlled DDS, that only require receiving formulas to generate arbitrary waveforms.

CHAPTER 8 CONCLUSION AND OUTLOOK

8.1 Conclusion

In my whole Ph.D career, we focused on how to make two-dimensional ion crystal being useful for quantum information processing. We started from negotiating with the company about how to fabricate the trap, how to make laser cutting precise, and how to isolate electrodes without desctroy the coating on the side wall of the trap. Then we build a useful vacuum system to hold the trap. We developed a systematic method to compensate the micromotion of 2D ion crystals, and used Raman beam to measure the residual micromotion strength. We also developed a double-EIT cooling method for $^{171}\mathrm{Yb}^{+}$, and used this method to prepare the motional ground states of 2D ion crystals. Finally, we performed a quantum simulation experiment with 2D ion crystals that prepare ground states of different Ising model.

8.2 Outlook: the future of trapped ion quantum information processor

Quantum information processing with trapped ions has been pursued for almost three decades. As the earliest system proposed for quantum computation, trapped ions show extremely high gate fidelities, long coherence time, and full connectivity. However, the charge of the ion makes it hard to scale up the size of the trapped ion quantum processor. Thirty years ago, the interaction between charged ions was considered a bus for transferring information stored in ions' internal state. However, nowadays, people found that it very challenging to perform high-fidelity entangling gates under complex motional modes as the number of ions increases. Several ideas were proposed to solve these problems, like using modulated pulse and QCCD. Modulated pulses use modulation to simultaneously close all the phonon trajectories at the end of the entangling gate. At the same time, QCCD makes only two ions entangled during the gate by moving the ions' position. The charge of ions also makes a single crystal fragile to background collisions. When a background particle collides with a single ion, the collision energy could transfer to collective motional modes formed by strong Column interaction between charged ions and make the whole crystal melt. As a comparison, if a collision happens for natural atoms, only the atom being collided would be ejected from the optical trap, and the other atoms would remain at their original positions. The problem of background collision could be solved by putting it trapped into a cryogenic system, and people already show hundreds of ions stably confined in it. Another limitation on the scalability of ion crystals is the weak axial confinement. As the number of ions increases, the axial trap frequency must be continuously reduced. However, a too-small axial trap frequency would make the axial modes hard to be cooled down to near ground state, and hot axial modes could induce amplitude noise into quantum operations. Can we increase the number meanwhile have a high axial trap frequency? A two-dimensional ion crystal is one of the possible solutions. If we keep the axial trap frequency, the number of ions could increase from N to N^2. Nowadays, the largest trapped ion system has around 60 ions. If we change it to a 2D crystal, the number of ions could increase to 3600, which is an unbelievable number for the current trapped ion community. However, we admit that 2D ion crystal is not the final solution for a fault-tolerant quantum computer with millions, even trillions of ions. Assuming an ion-ion distance of 5 μm, a trapped ion system with millions of qubit could have a size of 5 m for a 1D chain or size of 5 mm for a 2D crystal. The size of the 2D ion crystal looks acceptable. However, it is still unknown whether the axial micromotion would introduce a fatal influence on the quality of quantum operations on 2D ion crystals with such a size, which could be a future research direction. If there is an upper bound N_u on the number of ions inside a single crystal, how can we pursue Moore's law for quantum computers? Ion-photon interface could be a solution. A single ion could emit tens of millions of photons in one second, corresponding to a single photon emission time of tens of nanoseconds. Suppose we scale up trapped ion quantum processors by adding more modules with N_u ions and connecting them by an ion-photon interface. In that case, the maximal number of a trapped ion quantum processor is N_u^2 for the ion-photon interface between any pair of modules since the maximal number of modules can be connected to a single module is the number of ions inside that module. Even with 2D ion crystal, we can only increase this limitation to N_u^2, which cannot guarantee exponential scalability. One possible solution is using a switchable ion-photon interface, and we can only connect modules when information exchange is required, sacrificing the ion-photon connection's speed.

BIBLIOGRAPHY

[1] Bromley A G. Charles babbage's analytical engine, 1838[J]. Annals of the History of Computing, 1982, 4(3): 196-217.

[2] Hollerith H. An electric tabulating system[M]//The Origins of Digital Computers. Springer, 1982: 133-143.

[3] Herman hollerith[EB/OL]. http://www.columbia.edu/cu/computinghistory/hollerith.html.

[4] Turing A M, et al. On computable numbers, with an application to the entscheidungsproblem [J]. J. of Math, 1936, 58(345-363): 5.

[5] John mauchly[EB/OL]. https://findingaids.library.upenn.edu/records/UPENN_RBML_PUSP.MS.COLL.925.

[6] Knuth D E. Selected papers on computer science[M]. Cambridge University Press, 1996.

[7] Von Neumann J. First draft of a report on the edvac[J]. IEEE Annals of the History of Computing, 1993, 15(4): 27-75.

[8] Bardeen J, Brattain W H. The transistor, a semi-conductor triode[J]. Physical Review, 1948, 74(2): 230.

[9] Shurkin J N. Broken genius: The rise and fall of william shockley, creator of the electronic age [M]. Palgrave Macmillan, 2006.

[10] Brassard G. Brief history of quantum cryptography: A personal perspective[C]//IEEE Information Theory Workshop on Theory and Practice in Information-Theoretic Security, 2005. IEEE, 2005: 19-23.

[11] 40 years of quantum computing[J/OL]. Nature Reviews Physics, 2022, 4(1): 1-1. https://doi.org/10.1038/s42254-021-00410-6.

[12] Benioff P. The computer as a physical system: A microscopic quantum mechanical hamiltonian model of computers as represented by turing machines[J]. Journal of statistical physics, 1980, 22(5): 563-591.

[13] Toffoli T. Physics and computation[J]. International Journal of Theoretical Physics, 1982, 21 (3): 165-175.

[14] Fredkin E, Toffoli T. Conservative logic[J]. International Journal of theoretical physics, 1982, 21(3): 219-253.

[15] Deutsch D. Quantum theory, the church–turing principle and the universal quantum computer [J]. Proceedings of the Royal Society of London. A. Mathematical and Physical Sciences, 1985, 400(1818): 97-117.

[16] Deutsch D E. Quantum computational networks[J]. Proceedings of the Royal Society of London. A. Mathematical and Physical Sciences, 1989, 425(1868): 73-90.

[17] Deutsch D, Jozsa R. Rapid solution of problems by quantum computation[J]. Proceedings of the Royal Society of London. Series A: Mathematical and Physical Sciences, 1992, 439(1907): 553-558.

[18] Lloyd S. A potentially realizable quantum computer[J]. Science, 1993, 261(5128): 1569-1571.

[19] Bernstein E, Vazirani U. Quantum complexity theory[C]//Proceedings of the twenty-fifth annual ACM symposium on Theory of computing. 1993: 11-20.

[20] Yao A C C. Quantum circuit complexity[C]//Proceedings of 1993 IEEE 34th Annual Foundations of Computer Science. IEEE, 1993: 352-361.

[21] Obermayer K, Teich W G, Mahler G. Structural basis of multistationary quantum systems. i. effective single-particle dynamics[J/OL]. Phys. Rev. B, 1988, 37: 8096-8110. https://link.aps.org/doi/10.1103/PhysRevB.37.8096.

[22] Davidovich L, Zagury N, Brune M, et al. Teleportation of an atomic state between two cavities using nonlocal microwave fields[J]. Physical Review A, 1994, 50(2): R895.

[23] Turchette Q A, Hood C J, Lange W, et al. Measurement of conditional phase shifts for quantum logic[J]. Physical Review Letters, 1995, 75(25): 4710.

[24] Monroe C, Meekhof D M, King B E, et al. Demonstration of a fundamental quantum logic gate [J]. Physical review letters, 1995, 75(25): 4714.

[25] Cirac J I, Zoller P. Quantum computations with cold trapped ions[J]. Physical review letters, 1995, 74(20): 4091.

[26] Gershenfeld N A, Chuang I L. Bulk spin-resonance quantum computation[J]. science, 1997, 275(5298): 350-356.

[27] Shnirman A, Schön G, Hermon Z. Quantum manipulations of small josephson junctions[J]. Physical Review Letters, 1997, 79(12): 2371.

[28] Loss D, DiVincenzo D P. Quantum computation with quantum dots[J]. Physical Review A, 1998, 57(1): 120.

[29] Kane B E. A silicon-based nuclear spin quantum computer[J]. nature, 1998, 393(6681): 133-137.

[30] Imamog A, Awschalom D D, Burkard G, et al. Quantum information processing using quantum dot spins and cavity qed[J]. Physical review letters, 1999, 83(20): 4204.

[31] Mooij J, Orlando T, Levitov L, et al. Josephson persistent-current qubit[J]. Science, 1999, 285 (5430): 1036-1039.

[32] Platzman P, Dykman M. Quantum computing with electrons floating on liquid helium[J]. Science, 1999, 284(5422): 1967-1969.

[33] Lukin M D, Fleischhauer M, Cote R, et al. Dipole blockade and quantum information processing in mesoscopic atomic ensembles[J]. Physical review letters, 2001, 87(3): 037901.

[34] DiVincenzo D P. The physical implementation of quantum computation[J]. Fortschritte der Physik: Progress of Physics, 2000, 48(9-11): 771-783.

[35] Paul W. Electromagnetic traps for charged and neutral particles[J]. Reviews of modern physics, 1990, 62(3): 531.

[36] Duhem P. èmile mathieu, his life and works[J]. Bulletin of the American Mathematical Society, 1892, 1(7): 156-168.

[37] Leibfried D, Blatt R, Monroe C, et al. Quantum dynamics of single trapped ions[J/OL]. Reviews of Modern Physics, 2003, 75(1): 281. https://journals.aps.org/rmp/abstract/10.1103/RevModPhys.75.281.

[38] Wang P, Luan C Y, Qiao M, et al. Single ion qubit with estimated coherence time exceeding one hour[J/OL]. Nature Communications, 2021, 12(1): 233. https://doi.org/10.1038/s41467-020-20330-w.

[39] Yang H X, Ma J Y, Wu Y K, et al. Realizing coherently convertible dual-type qubits with the same ion species[J/OL]. Nature Physics, 2022, 18(9): 1058-1061. https://doi.org/10.1038/s41567-022-01661-5.

[40] Srinivas R, Burd S C, Knaack H M, et al. High-fidelity laser-free universal control of trapped ion qubits[J/OL]. Nature, 2021, 597(7875): 209-213. https://doi.org/10.1038/s41586-021-03809-4.

[41] Sutherland R, Srinivas R, Burd S C, et al. Versatile laser-free trapped-ion entangling gates[J]. New journal of physics, 2019, 21(3): 033033.

[42] Brownnutt M, Wilpers G, Gill P, et al. Monolithic microfabricated ion trap chip design for scaleable quantum processors[J]. New J. Phys., 2006, 8(10): 232.

[43] Shaikh F, Ozakin A, Amini J M, et al. Monolithic microfabricated symmetric ion trap for quantum information processing[A]. 2011.

[44] Wilpers G, See P, Gill P, et al. A monolithic array of three-dimensional ion traps fabricated with conventional semiconductor technology[J]. Nature Nanotech., 2012, 7(9): 572.

[45] Hensinger W, Olmschenk S, Stick D, et al. T-junction ion trap array for two-dimensional ion shuttling, storage, and manipulation[J]. Appl. Phys. Lett., 2006, 88(3): 034101.

[46] Madsen M J. Advanced ion trap development and ultrafast laser-ion interactions[D]. University of Michigan, 2006.

[47] Olmschenk S, Younge K C, Moehring D L, et al. Manipulation and detection of a trapped Yb^+ hyperfine qubit[J]. Phys. Rev. A, 2007, 76(5): 052314.

[48] Debnath S. A programmable five qubit quantum computer using trapped atomic ions[D]. University of Maryland, College Park, 2016.

[49] Lee M W, Jarratt M C, Marciniak C, et al. Frequency stabilization of a 369 nm diode laser by nonlinear spectroscopy of ytterbium ions in a discharge[J/OL]. Opt. Express, 2014, 22(6): 7210-7221. https://opg.optica.org/oe/abstract.cfm?URI=oe-22-6-7210. DOI: 10.1364/OE.22.007210.

[50] Richerme P. Two-dimensional ion crystals in radio-frequency traps for quantum simulation[J]. Phys. Rev. A, 2016, 94(3): 032320.

[51] Dubin D H. Theory of structural phase transitions in a trapped coulomb crystal[J]. Phys. Rev. Lett., 1993, 71(17): 2753.

[52] Podolsky D, Shimshoni E, Morigi G, et al. Buckling transitions and clock order of two-dimensional coulomb crystals[J]. Phys. Rev. X, 2016, 6(3): 031025.

[53] Yan L, Wan W, Chen L, et al. Exploring structural phase transitions of ion crystals[J]. Sci. Rep., 2016, 6: 21547.

[54] Wang S T, Shen C, Duan L M. Quantum computation under micromotion in a planar ion crystal [J]. Sci. Rep., 2015, 5: 8555.

[55] Schiffer J P. Phase transitions in anisotropically confined ionic crystals[J/OL]. Phys. Rev. Lett., 1993, 70: 818-821. https://link.aps.org/doi/10.1103/PhysRevLett.70.818.

[56] Fishman S, De Chiara G, Calarco T, et al. Structural phase transitions in low-dimensional ion crystals[J]. Phys. Rev. B, 2008, 77(6): 064111.

[57] Mielenz M, Brox J, Kahra S, et al. Trapping of topological-structural defects in coulomb crystals [J/OL]. Phys. Rev. Lett., 2013, 110: 133004. https://link.aps.org/doi/10.1103/PhysRevLett.110.133004.

[58] Partner H L, Nigmatullin R, Burgermeister T, et al. Dynamics of topological defects in ion coulomb crystals[J]. New J. Phys., 2013, 15(10): 103013.

[59] Ulm S, Roßnagel J, Jacob G, et al. Observation of the kibble–zurek scaling law for defect formation in ion crystals[J]. Nature Commun., 2013, 4(1): 1-7.

[60] Berkeland D, Miller J, Bergquist J C, et al. Minimization of ion micromotion in a paul trap[J]. J. Appl. Phys., 1998, 83(10): 5025-5033.

[61] Leibfried D. Individual addressing and state readout of trapped ions utilizing rf micromotion [J]. Physical Review A, 1999, 60(5): R3335.

[62] Qiao M, Wang Y, Cai Z, et al. Double-eit ground-state cooling of stationary two-dimensional ion lattices[A]. 2020.

[63] Zhu S L, Monroe C, Duan L M. Trapped ion quantum computation with transverse phonon modes[J]. Phys. Rev. Lett., 2006, 97(5): 050505.

[64] Landa H, Drewsen M, Reznik B, et al. Classical and quantum modes of coupled mathieu equations[J]. J. Phys. A: Math.Theor., 2012, 45(45): 455305.

[65] Landa H, Drewsen M, Reznik B, et al. Modes of oscillation in radiofrequency paul traps[J]. New J. Phys., 2012, 14(9): 093023.

[66] Wang Y, Um M, Zhang J, et al. Single-qubit quantum memory exceeding ten-minute coherence time[J/OL]. Nature Photonics, 2017, 11(10): 646. https://www.nature.com/articles/s41566-017-0007-1.

[67] Wang Y, Qiao M, Cai Z, et al. Realization of two-dimensional crystal of ions in a monolithic paul trap[A/OL]. 2019. https://arxiv.org/abs/1912.04262.

[68] Häffner H, Gulde S, Riebe M, et al. Precision measurement and compensation of optical stark shifts for an ion-trap quantum processor[J/OL]. Phys. Rev. Lett., 2003, 90(14): 143602. https://journals.aps.org/prl/abstract/10.1103/PhysRevLett.90.143602.

[69] Ejtemaee S, Haljan P C. 3d sisyphus cooling of trapped ions[J/OL]. Phys. Rev. Lett., 2017, 119 (4): 043001. https://journals.aps.org/prl/abstract/10.1103/PhysRevLett.119.043001.

[70] Lechner R, Maier C, Hempel C, et al. Electromagnetically-induced-transparency ground-state cooling of long ion strings[J/OL]. Physical Review A, 2016, 93(5): 053401. https://link.aps.org/pdf/10.1103/PhysRevA.93.053401.

[71] Sawyer B C, Britton J W, Keith A C, et al. Spectroscopy and thermometry of drumhead modes in a mesoscopic trapped-ion crystal using entanglement[J/OL]. Phys. Rev. Lett., 2012, 108(21): 213003. https://journals.aps.org/prl/abstract/10.1103/PhysRevLett.108.213003.

[72] Jordan E, Gilmore K A, Shankar A, et al. Near ground-state cooling of two-dimensional trapped-ion crystals with more than 100 ions[J/OL]. Phys. Rev. Lett., 2019, 122(5): 053603. https://journals.aps.org/prl/abstract/10.1103/PhysRevLett.122.053603.

[73] Shankar A, Jordan E, Gilmore K A, et al. Modeling near ground-state cooling of two-dimensional ion crystals in a penning trap using electromagnetically induced transparency [J/OL]. Physical Review A, 2019, 99(2): 023409. https://journals.aps.org/pra/abstract/10.1103/PhysRevA.99.023409.

[74] Lounis B, Cohen-Tannoudji C. Coherent population trapping and fano profiles[J/OL]. Journal de Physique II, 1992, 2(4): 579-592. https://jp2.journaldephysique.org/articles/jp2/abs/1992/04/jp2v2p579/jp2v2p579.html.

[75] Hayes D, Matsukevich D N, Maunz P, et al. Entanglement of atomic qubits using an optical frequency comb[J/OL]. Phys. Rev. Lett., 2010, 104(14): 140501. https://journals.aps.org/prl/abstract/10.1103/PhysRevLett.104.140501.

[76] Turchette Q A, King B E, Leibfried D, et al. Heating of trapped ions from the quantum ground state[J]. Physical Review A, 2000, 61(6): 063418.

[77] Wannier G H. Antiferromagnetism. the triangular ising net[J/OL]. Phys. Rev., 1950, 79: 357-364. https://link.aps.org/doi/10.1103/PhysRev.79.357.

[78] Moessner R, Ramirez A P. Geometrical frustration[J]. Phys. Today, 2006, 59(2): 24.

[79] Balents L. Spin liquids in frustrated magnets[J/OL]. Nature, 2010, 464(7286): 199-208. https://doi.org/10.1038/nature08917.

[80] Schmidt B, Thalmeier P. Frustrated two dimensional quantum magnets[J]. Phys. Rep., 2017, 703: 1-59.

[81] Barahona F. On the computational complexity of ising spin glass models[J/OL]. Journal of Physics A: Mathematical and General, 1982, 15(10): 3241-3253. https://doi.org/10.1088/0305-4470/15/10/028.

[82] Lucas A. Ising formulations of many np problems[J/OL]. Frontiers in Physics, 2014, 2: 5. https://www.frontiersin.org/article/10.3389/fphy.2014.00005.

[83] Wen X G. Colloquium: Zoo of quantum-topological phases of matter[J/OL]. Rev. Mod. Phys., 2017, 89: 041004. https://link.aps.org/doi/10.1103/RevModPhys.89.041004.

[84] Zhou Y, Kanoda K, Ng T K. Quantum spin liquid states[J/OL]. Rev. Mod. Phys., 2017, 89: 025003. https://link.aps.org/doi/10.1103/RevModPhys.89.025003.

[85] Kosterlitz J M, Thouless D J. Ordering, metastability and phase transitions in two-dimensional systems[J]. Journal of Physics C: Solid State Physics, 1973, 6(7): 1181.

[86] King A D, Nisoli C, Dahl E D, et al. Qubit spin ice[J/OL]. Science, 2021, 373(6554): 576-580. https://www.science.org/doi/abs/10.1126/science.abe2824.

[87] Ebadi S, Wang T T, Levine H, et al. Quantum phases of matter on a 256-atom programmable quantum simulator[J/OL]. Nature, 2021, 595(7866): 227-232. https://doi.org/10.1038/s41586-021-03582-4.

[88] Scholl P, Schuler M, Williams H J, et al. Quantum simulation of 2d antiferromagnets with hundreds of rydberg atoms[J/OL]. Nature, 2021, 595(7866): 233-238. https://doi.org/10.1038/s41586-021-03585-1.

[89] Qiu X, Zoller P, Li X. Programmable quantum annealing architectures with ising quantum wires [J/OL]. PRX Quantum, 2020, 1: 020311. https://link.aps.org/doi/10.1103/PRXQuantum.1.020311.

[90] Wang Y, Um M, Zhang J, et al. Single-qubit quantum memory exceeding ten-minute coherence time[J/OL]. Nature Photonics, 2017, 11(10): 646-650. https://doi.org/10.1038/s41566-017-0007-1.

[91] Kim K, Chang M S, Korenblit S, et al. Quantum simulation of frustrated ising spins with trapped ions[J/OL]. Nature, 2010, 465(7298): 590-593. https://doi.org/10.1038/nature09071.

[92] Islam R, Edwards E E, Kim K, et al. Onset of a quantum phase transition with a trapped ion quantum simulator[J/OL]. Nature Communications, 2011, 2(1): 377. https://doi.org/10.1038/ncomms1374.

[93] Islam R, Senko C, Campbell W C, et al. Emergence and frustration of magnetism with variable-range interactions in a quantum simulator[J/OL]. Science, 2013, 340(6132): 583-587. https://www.science.org/doi/abs/10.1126/science.1232296.

[94] Monroe C, Campbell W C, Duan L M, et al. Programmable quantum simulations of spin systems with trapped ions[J/OL]. Rev. Mod. Phys., 2021, 93: 025001. https://link.aps.org/doi/10.1103/RevModPhys.93.025001.

[95] Bermudez A, Almeida J, Schmidt-Kaler F, et al. Frustrated quantum spin models with cold coulomb crystals[J]. Phys. Rev. Lett., 2011, 107(20): 207209.

[96] Nath R, Dalmonte M, Glaetzle A W, et al. Hexagonal plaquette spin–spin interactions and quantum magnetism in a two-dimensional ion crystal[J]. New J. Phys., 2015, 17(6): 065018.

[97] Cirac J I, Zoller P. A scalable quantum computer with ions in an array of microtraps[J/OL]. Nature, 2000, 404(6778): 579-581. https://doi.org/10.1038/35007021.

[98] Chiaverini J, Lybarger W E. Laserless trapped-ion quantum simulations without spontaneous scattering using microtrap arrays[J/OL]. Phys. Rev. A, 2008, 77: 022324. https://link.aps.org/doi/10.1103/PhysRevA.77.022324.

[99] Clark R J, Lin T, Brown K R, et al. A two-dimensional lattice ion trap for quantum simulation [J/OL]. Journal of Applied Physics, 2009, 105(1): 013114. https://doi.org/10.1063/1.3056227.

[100] Britton J W, Sawyer B C, Keith A C, et al. Engineered two-dimensional ising interactions in a trapped-ion quantum simulator with hundreds of spins[J/OL]. Nature, 2012, 484(7395): 489-492. https://doi.org/10.1038/nature10981.

[101] Yoshimura B, Stork M, Dadic D, et al. Creation of two-dimensional coulomb crystals of ions in oblate paul traps for quantum simulations[J/OL]. EPJ Quant. Techn., 2015, 2(1): 2. https://doi.org/10.1140/epjqt14.

[102] Bohnet J G, Sawyer B C, Britton J W, et al. Quantum spin dynamics and entanglement generation with hundreds of trapped ions[J/OL]. Science, 2016, 352(6291): 1297-1301. https://www.science.org/doi/abs/10.1126/science.aad9958.

[103] Sterling R C, Rattanasonti H, Weidt S, et al. Fabrication and operation of a two-dimensional ion-trap lattice on a high-voltage microchip[J/OL]. Nat. Commun., 2014, 5(1): 3637. https://doi.org/10.1038/ncomms4637.

[104] Mielenz M, Kalis H, Wittemer M, et al. Arrays of individually controlled ions suitable for two-dimensional quantum simulations[J/OL]. Nat. Commun., 2016, 7(1): ncomms11839. https://doi.org/10.1038/ncomms11839.

[105] Hakelberg F, Kiefer P, Wittemer M, et al. Interference in a prototype of a two-dimensional ion trap array quantum simulator[J]. Phys. Rev. Lett., 2019, 123(10): 100504.

[106] Wang Y, Qiao M, Cai Z, et al. Coherently manipulated 2d ion crystal in a monolithic paul trap [J/OL]. Advanced Quantum Technologies, 2020, 3(11): 2000068. https://onlinelibrary.wiley.com/doi/abs/10.1002/qute.202000068. DOI: https://doi.org/10.1002/qute.202000068.

[107] Porras D, Cirac J I. Effective quantum spin systems with trapped ions[J/OL]. Phys. Rev. Lett., 2004, 92: 207901. https://link.aps.org/doi/10.1103/PhysRevLett.92.207901.

[108] Deng X L, Porras D, Cirac J I. Effective spin quantum phases in systems of trapped ions[J/OL]. Phys. Rev. A, 2005, 72: 063407. https://link.aps.org/doi/10.1103/PhysRevA.72.063407.

[109] Kim K, Chang M S, Islam R, et al. Entanglement and tunable spin-spin couplings between trapped ions using multiple transverse modes[J/OL]. Phys. Rev. Lett., 2009, 103: 120502. https://link.aps.org/doi/10.1103/PhysRevLett.103.120502.

[110] Korenblit S, Kafri D, Campbell W C, et al. Quantum simulation of spin models on an arbitrary lattice with trapped ions[J]. New Journal of Physics, 2012, 14(9): 095024.

[111] Shapira Y, Shaniv R, Manovitz T, et al. Theory of robust multiqubit nonadiabatic gates for trapped ions[J]. Phys. Rev. A, 2020, 101(3): 032330.

[112] Kim K, Chang M S, Islam R, et al. Entanglement and tunable spin-spin couplings between trapped ions using multiple transverse modes[J/OL]. Phys. Rev. Lett., 2009, 103: 120502. https://link.aps.org/doi/10.1103/PhysRevLett.103.120502.

[113] Qiao M, Wang Y, Cai Z, et al. Double-electromagnetically-induced-transparency ground-state cooling of stationary two-dimensional ion crystals[J/OL]. Phys. Rev. Lett., 2021, 126: 023604. https://link.aps.org/doi/10.1103/PhysRevLett.126.023604.

[114] Feng L, Tan W L, De A, et al. Efficient ground-state cooling of large trapped-ion chains with an electromagnetically-induced-transparency tripod scheme[J/OL]. Phys. Rev. Lett., 2020, 125: 053001. https://link.aps.org/doi/10.1103/PhysRevLett.125.053001.

[115] Olmschenk S, Younge K C, Moehring D L, et al. Manipulation and detection of a trapped yb$^+$ hyperfine qubit[J/OL]. Phys. Rev. A, 2007, 76: 052314. https://link.aps.org/doi/10.1103/PhysRevA.76.052314.

[116] Roland J, Cerf N J. Quantum search by local adiabatic evolution[J/OL]. Phys. Rev. A, 2002, 65: 042308. https://link.aps.org/doi/10.1103/PhysRevA.65.042308.

[117] Zhang J, Pagano G, Hess P W, et al. Observation of a many-body dynamical phase transition with a 53-qubit quantum simulator[J/OL]. Nature, 2017, 551(7682): 601-604. https://doi.org/10.1038/nature24654.

[118] Shaffer R, Megidish E, Broz J, et al. Practical verification protocols for analog quantum simulators[J/OL]. npj Quantum Information, 2021, 7(1): 46. https://doi.org/10.1038/s41534-021-00380-8.

[119] Zhou L, Wang S T, Choi S, et al. Quantum approximate optimization algorithm: Performance, mechanism, and implementation on near-term devices[J/OL]. Phys. Rev. X, 2020, 10: 021067. https://link.aps.org/doi/10.1103/PhysRevX.10.021067.

[120] Bruzewicz C D, Sage J M, Chiaverini J. Measurement of ion motional heating rates over a range of trap frequencies and temperatures[J/OL]. Phys. Rev. A, 2015, 91: 041402. https://link.aps.org/doi/10.1103/PhysRevA.91.041402.

[121] Lechner W, Hauke P, Zoller P. A quantum annealing architecture with all-to-all connectivity from local interactions[J]. Sci. Adv., 2015, 1(9): e1500838.

[122] Qiu X, Zoller P, Li X. Programmable quantum annealing architectures with ising quantum wires [J/OL]. PRX Quantum, 2020, 1: 020311. https://link.aps.org/doi/10.1103/PRXQuantum.1.020311.

[123] Lu Y, Zhang S, Zhang K, et al. Global entangling gates on arbitrary ion qubits[J/OL]. Nature, 2019, 572(7769): 363-367. https://doi.org/10.1038/s41586-019-1428-4.

[124] Shapira Y, Shaniv R, Manovitz T, et al. Theory of robust multiqubit nonadiabatic gates for trapped ions[J/OL]. Phys. Rev. A, 2020, 101: 032330. https://link.aps.org/doi/10.1103/PhysRevA.101.032330.

[125] Kuramoto Y, Yokoyama H. Exactly soluble supersymmetric t-j-type model with long-range exchange and transfer[J/OL]. Phys. Rev. Lett., 1991, 67: 1338-1341. https://link.aps.org/doi/10.1103/PhysRevLett.67.1338.

[126] Kuramoto Y, Kato Y. Dynamics of one-dimensional quantum systems: inverse-square interaction models[M]. Cambridge University Press, 2009.

[127] Haldane F D M. Exact jastrow-gutzwiller resonating-valence-bond ground state of the spin-$\frac{1}{2}$ antiferromagnetic heisenberg chain with $1/r^2$ exchange[J/OL]. Phys. Rev. Lett., 1988, 60: 635-638. https://link.aps.org/doi/10.1103/PhysRevLett.60.635.

[128] Shastry B S. Exact solution of an s=1/2 heisenberg antiferromagnetic chain with long-ranged interactions[J/OL]. Phys. Rev. Lett., 1988, 60: 639-642. https://link.aps.org/doi/10.1103/PhysRevLett.60.639.

[129] Graß T, Lewenstein M. Trapped-ion quantum simulation of tunable-range heisenberg chains [J/OL]. EPJ Quantum Technology, 2014, 1(1): 8. https://doi.org/10.1140/epjqt8.

[130] Chertkov E, Villalonga B, Clark B K. Numerical evidence for many-body localization in two and three dimensions[J/OL]. Phys. Rev. Lett., 2021, 126: 180602. https://link.aps.org/doi/10.1103/PhysRevLett.126.180602.

[131] Berkeland D J, Miller J D, Bergquist J C, et al. Minimization of ion micromotion in a paul trap [J/OL]. Journal of Applied Physics, 1998, 83(10): 5025-5033. https://doi.org/10.1063/1.367318.

[132] Bhattacharyya A. On a measure of divergence between two multinomial populations[J/OL]. Sankhyā: The Indian Journal of Statistics (1933-1960), 1946, 7(4): 401-406. http://www.jstor.org/stable/25047882.

[133] Zhang J. Quantum operation of phonons and entanglement of multi-species ions[D]. Tsinghua University, 2017.

[134] Pino J M, Dreiling J M, Figgatt C, et al. Demonstration of the trapped-ion quantum ccd computer architecture[J/OL]. Nature, 2021, 592(7853): 209-213. https://doi.org/10.1038/s41586-021-03318-4.

ACKNOWLEDGEMENTS

I am deeply grateful for the invaluable support and guidance I received throughout my time in the lab. Since joining in 2017, Professor Kihwan Kim has been instrumental in my journey, providing me with immense help in acclimating to the lab environment and the intricacies of our experiments. Prof. Kim's unwavering dedication is evident every time I step into the lab; he is readily available in his office, always willing to engage in discussions and address any queries I may have. His patience and insightful suggestions have played a crucial role in shaping my understanding and passion for the experiments we conduct. Prof. Kim's enthusiasm is truly inspiring, motivating me to push my boundaries.

I would also like to extend my heartfelt gratitude to Prof. Ye Wang, who was a recent graduate of the lab when I joined and has since become a professor at USTC. Prof. Wang's remarkable creation of the monolithic trap has allowed me to build upon the groundbreaking work of those who came before me, and for that, I am truly thankful.

Additionally, I would like to express my appreciation to all my dedicated colleagues who have worked alongside me during these past few years: Junhua Zhang, Yao Lu, Shuaining Zhang, Yangchao Shen, Dingshun Lv, Shuoming An, Pengfei Wang, Wentao Chen, Chunyang Luan, Zhengyang Cai, Jialiang Zhang, Naijun Jin, Tian Xie, Erfu Gao, Haonan Tian, Lingfeng Ou, and Hengchao Tu. Their unwavering support and camaraderie have made this challenging Ph.D. journey more enjoyable, particularly Zhengyang Cai, whose presence has brought so much happiness to our shared struggles.

I would also like to extend my sincere gratitude to our collaborators from Arc Quantum Software Inc., particularly Riling Li and Keli Zheng. Their invaluable assistance in the development of the quantum control software Cion has been instrumental to the success of our research. Their expertise and support have greatly enhanced our capabilities in the lab, and I am truly thankful for their contributions.

Finally, I would like to express my deepest gratitude to my parents and girlfriend, who have been unwavering pillars of support throughout my journey. Their constant presence, love, and encouragement have been a source of strength and motivation for me. I am truly blessed to have such a loving family, and I am forever grateful for their unconditional love and support.

声　明

本人郑重声明：所呈交的学位论文，是本人在导师指导下，独立进行研究工作所取得的成果。尽我所知，除文中已经注明引用的内容外，本学位论文的研究成果不包含任何他人享有著作权的内容。对本论文所涉及的研究工作做出贡献的其他个人和集体，均已在文中以明确方式标明。

签　名：＿＿＿＿＿＿ 日　期：＿＿＿＿＿＿